

RICE UNIVERSITY

**Studies of one- and two-photon photoassociative
spectroscopy using ultracold strontium**

by

James Allen Aman

A THESIS SUBMITTED
IN PARTIAL FULFILLMENT OF THE
REQUIREMENTS FOR THE DEGREE

Doctor of Philosophy

APPROVED, THESIS COMMITTEE:

Thomas C. Killian, Chair
Professor of Physics and Astronomy

Randall G. Hulet
Fayez Sarofim Professor of Physics and
Astronomy

Kevin F. Kelly
Associate Professor of Electrical and
Computer Engineering

Houston, Texas

April, 2019

ABSTRACT

Studies of one- and two-photon photoassociative spectroscopy using ultracold strontium

by

James Allen Aman

”Lorem ipsum dolor sit amet, consectetur adipiscing elit, sed do eiusmod tempor incididunt ut labore et dolore magna aliqua. Ut enim ad minim veniam, quis nostrud exercitation ullamco laboris nisi ut aliquip ex ea commodo consequat. Duis aute irure dolor in reprehenderit in voluptate velit esse cillum dolore eu fugiat nulla pariatur. Excepteur sint occaecat cupidatat non proident, sunt in culpa qui officia deserunt mollit anim id est laborum.”

Acknowledgments

”Lorem ipsum dolor sit amet, consectetur adipiscing elit, sed do eiusmod tempor incididunt ut labore et dolore magna aliqua. Ut enim ad minim veniam, quis nostrud exercitation ullamco laboris nisi ut aliquip ex ea commodo consequat. Duis aute irure dolor in reprehenderit in voluptate velit esse cillum dolore eu fugiat nulla pariatur. Excepteur sint occaecat cupidatat non proident, sunt in culpa qui officia deserunt mollit anim id est laborum.”

Contents

Abstract	ii
Acknowledgments	iii
List of Illustrations	ix
List of Tables	xi
1 Introduction	1
1.1 Few-body physics	1
1.2 Halo molecules	2
1.3 Properties of strontium	2
1.4 Overview	2
1.5 Thesis Outline	3
2 The Neutral apparatus	5
2.1 Vacuum system	5
2.2 Laser systems	6
2.2.1 Wideband cooling stage: 461 nm	6
2.2.2 Narrowband cooling stage: 689 nm	6
2.2.3 Repumping: 481 nm	6
2.2.4 Optical dipole trap: 1064 nm	7
2.2.5 Optical toolbox	7
2.3 Experimental control and electronics	11
2.3.1 Computer control system	11
2.3.2 Ancillary laboratory systems	11
2.4 Apparatus benchmarks	12

3	Photoassociation in ultracold gases	13
3.1	Introduction	13
3.2	Theoretical description of trapped bosonic gases	15
3.2.1	Extracting data from column densities	18
3.3	Characterizing cold collisions	24
3.3.1	Low energy scattering	24
3.3.2	Modifying interactions with external fields	26
3.4	Modeling of photoassociation lineshapes	31
3.4.1	One-photon excitation of free to bound transitions	32
3.4.2	Extension to two-color spectra	32
4	Binding energy of the $^{86}\text{Sr}_2$ halo molecule	35
4.1	Probing the ground state potential	35
4.2	Experimental setup	39
4.2.1	Photoassociation	45
4.2.2	Consideration of the trap depth	48
4.3	Theoretical description	49
4.4	Spectral fitting and determination of energy shifts	56
4.4.1	AC Stark shift due to excitation lasers	56
4.4.2	Density-dependent frequency shift	59
4.4.3	AC Stark Shift due to Trapping Lasers	61
4.5	Unperturbed halo binding energy	63
4.6	Calculating the bound-bound Frank-Condon factor	67
5	Strongly coupled PAS of a weakly bound molecule	76
5.1	Introduction	76
5.2	Experimental methods	76
5.3	Three level model	77
5.4	Resonance positions	77

5.5	Lineshape	77
5.6	Emergence of multi-photon Raman coupling	78
6	Progress towards studies of quantum magnetism	79
6.1	532 nm optical lattice: installation and characterization	80
6.1.1	Background	80
6.1.2	Setup	87
6.1.3	Measurement and results	87
6.2	Spin manipulation of ^{87}Sr	92
6.3	Search for narrowline PA molecules using various spin mixtures . . .	92
7	Conclusion	93
	Bibliography	95
	Appendices	105
A	Two-particle momentum probability distribution	106
A.1	Standard form	106
A.2	Truncated form	107
B	Imagefit analysis routine	113
B.1	Background removal	113
B.1.1	Principal component analysis	113
B.1.2	Comparison of PCA implementations	115
B.2	Fitting the spatial distribution	115
B.3	Evaluating fit parameters	115
B.3.1	Writing new plug-ins	116
B.3.2	Suggested improvement	116

C neuKLEIN - Killian lab experimental interface	117
C.1 Labview code	117
C.2 FPGA code	118
C.3 Possible future improvements	118
D Experimental control computer hardware	119
D.1 Overview of status	119
D.2 Migration to a new machine	119
D.3 PixelFly camera system	119
E Concise derivation of effective volumes	120
F Repair of 922 Lynx master	121
G Custom circuitry	122
G.1 AC line zero crossing trigger	122
G.2 Hard drive shutters	122
G.3 Power locks	122
G.4 Photodiodes	122
G.5 Infinite sample and hold	122
G.5.1 Reduced intensity fluctuations for sub-hertz exposures	122
H Miscellaneous tips and tricks	123
H.1 Alignment of GHz AOM	123
H.2 Using the Picoscope in Labview(TM)	123
H.3 Liquid crystal retarder	123
H.4 Newport(TM) optomotion control	123
H.5 Fast analog lock for 689 nm	123
H.6 Porta CoM technique	123

H.7 Measuring Rabi frequencies	123
--	-----

Illustrations

1.1	Properties of strontium. Left: Natural abundances and s-wave scattering lengths for all mixtures of Sr. Right: Simplified energy level diagram of Sr showing the relevant states used for trapping and cooling of the atomic gas	2
1.2	Properties of strontium	3
3.1	Ballistic expansion of particles	19
3.2	Strontium interatomic wavefunctions	26
3.3	Schematic representation of a Feshbach resonance	27
4.1	Strontium PAS potential	38
4.2	Strontium two-photon photoassociation	39
4.3	Schematic of PAS light generation	41
4.4	Histogram of PAS beam intensity variation	44
4.5	Characteristic view of the PA beatnote	44
4.6	PAS laser setup	46
4.7	Variation of 1064 nm trap depth	55
4.8	Variation of 689 nm excitation	57
4.9	Fit of 689 nm AC Stark shift	58
4.10	Measurement of halo state susceptibility, χ_{1064}	62
4.11	Determination of 86 scattering length	65
4.12	Variation of halo susceptibility as a function of Δ_1	66

4.13	Estimate of bound-bound coupling via isolated resonance model . . .	69
6.1	1D band structure as a function of lattice depth	82
6.2	Calculated interaction energies and tunneling rates for each isotope of strontium	85
6.3	Evolution of plane wave population using Kapitza-Dirac	88
6.4	Evolution of condensate fraction over time after adiabatically ramping on the lattice to $9E_r$. a,b) Comparison of total number and condensate fraction for a sample held in the optical dipole trap (red squares) or in a deep lattice (blue circles). c) Time of flight images after ramping on the lattice and diabatically projecting back to plane wave states.	89
6.5	Observation of driven sideband transitions	91

Tables

Chapter 1

Introduction

The ability to engineer and manipulate quantum states lies at the heart of modern atomic physics experiments using ultracold gases [1, 2, 3]. Two important tools for this pursuit are Feshbach resonances [4, 5] and optical lattices [6]. This proposal will detail our recent work building and characterizing a three-dimension optical lattice for use with ultracold and quantum degenerate gases of neutral strontium. Furthermore, we will present the first experiment we hope to pursue with the optical lattice; the creation of Feshbach molecules using an optical Feshbach resonance. We will also briefly discuss other future plans such as the production of highly excited ground state Sr_2 dimers through adiabatic internal state transfer.

Should probably mention somewhere that this is long-range PA, in contrast to short-range stuff being explored now.

[6]

1.1 Few-body physics

field of photoassociation in ultracold gases, wherein studies of molecular structure have revealed the most accurate descriptions of atomic interactions and have become a fundamental probe of the ultracold toolbox [7].

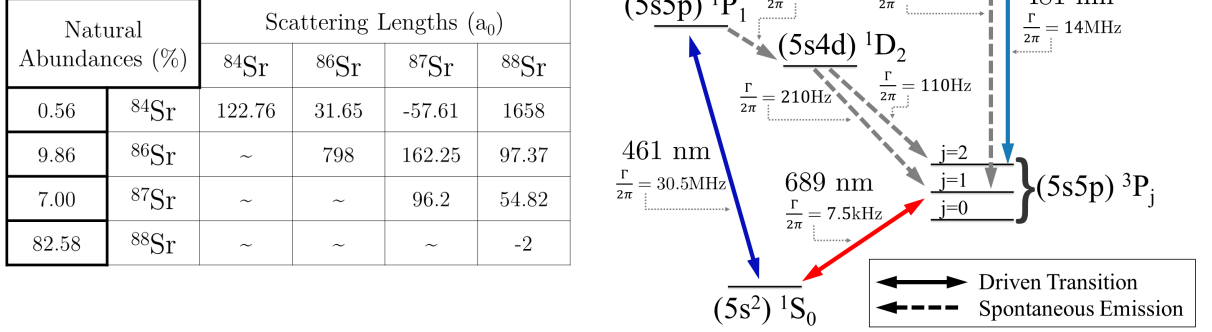


Figure 1.1 : Properties of strontium. Left: Natural abundances and s-wave scattering lengths for all mixtures of Sr. Right: Simplified energy level diagram of Sr showing the relevant states used for trapping and cooling of the atomic gas

1.2 Halo molecules

”Lorem ipsum dolor sit amet, consectetur adipiscing elit, sed do eiusmod tempor incididunt ut labore et dolore magna aliqua. Ut enim ad minim veniam, quis nostrud exercitation ullamco laboris nisi ut aliquip ex ea commodo consequat. Duis aute irure dolor in reprehenderit in voluptate velit esse cillum dolore eu fugiat nulla pariatur. Excepteur sint occaecat cupidatat non proident, sunt in culpa qui officia deserunt mollit anim id est laborum.”

1.3 Properties of strontium

1.4 Overview

The experiments in this proposal will be realized using an ultracold gas of atomic strontium. Fig. 1.4 shows all of the stable isotopes of strontium, their natural abundance, as well as their inter-particle scattering lengths. The isotopic differences in

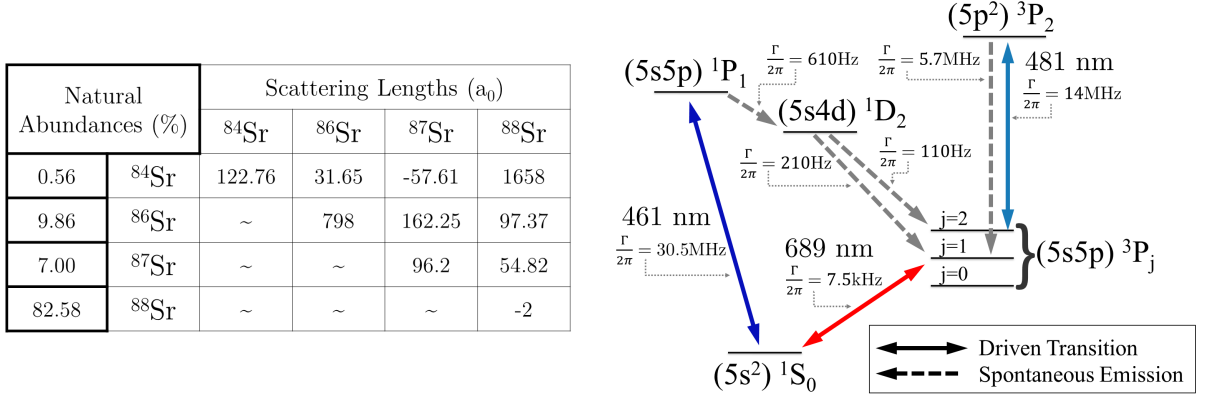


Figure 1.2 : Properties of strontium

Properties of strontium. Left: Natural abundances and s-wave scattering lengths for all mixtures of Sr. Right: Simplified energy level diagram of Sr showing the relevant states used for trapping and cooling of the atomic gas

strontium have important implications for their use in certain experiments. For example, none of the bosonic isotopes of strontium (^{88}Sr , ^{86}Sr , or ^{84}Sr) display hyperfine structure since they have no nuclear spin, $\mathbf{I} = 0$. However, the fermionic isotope ^{87}Sr has a large nuclear spin, $\mathbf{I} = 9/2$, which makes it an ideal candidate for exploring exotic phases of quantum magnetism [8? , 9]. In the studies presented in this proposal, we are sensitive to the isotopic shifts of the bosonic photoassociation lines along the $^1S_0 \rightarrow ^3P_1$ transition as well as the various interspecies scattering lengths.

1.5 Thesis Outline

”Lorem ipsum dolor sit amet, consectetur adipiscing elit, sed do eiusmod tempor incididunt ut labore et dolore magna aliqua. Ut enim ad minim veniam, quis nostrud exercitation ullamco laboris nisi ut aliquip ex ea commodo consequat. Duis aute irure

dolor in reprehenderit in voluptate velit esse cillum dolore eu fugiat nulla pariatur. Excepteur sint occaecat cupidatat non proident, sunt in culpa qui officia deserunt mollit anim id est laborum.”

$$V(x) = V_{lat} \sin^2(k_L x) \tag{1.1}$$

Chapter 2

The Neutral apparatus

Our experiments begin by cooling and trapping atomic strontium utilizing well-established atomic physics techniques [10, 11, 12, 13, 14, 15, 16, 17]. Fig. 1.4 shows the simplified energy level diagram employed in our cooling process. Once cooled, we typically obtain bulk samples in an optical dipole trap containing on the order of 10^6 atoms at temperatures $< 1\mu\text{K}$ and densities between $10^{12} - 10^{15} \text{ cm}^{-3}$ depending upon the isotope. Samples of ultracold atoms can then be directly loaded into an optical lattice potential by ramping up the intensity of the laser beams forming the optical lattice.

2.1 Vacuum system

”Lorem ipsum dolor sit amet, consectetur adipiscing elit, sed do eiusmod tempor incididunt ut labore et dolore magna aliqua. Ut enim ad minim veniam, quis nostrud exercitation ullamco laboris nisi ut aliquip ex ea commodo consequat. Duis aute irure dolor in reprehenderit in voluptate velit esse cillum dolore eu fugiat nulla pariatur. Excepteur sint occaecat cupidatat non proident, sunt in culpa qui officia deserunt mollit anim id est laborum.”

2.2 Laser systems

The heart of any atomic physics experiment is the laser systems which can be utilized for various studies.

2.2.1 Wideband cooling stage: 461 nm

”Lorem ipsum dolor sit amet, consectetur adipiscing elit, sed do eiusmod tempor incididunt ut labore et dolore magna aliqua. Ut enim ad minim veniam, quis nostrud exercitation ullamco laboris nisi ut aliquip ex ea commodo consequat. Duis aute irure dolor in reprehenderit in voluptate velit esse cillum dolore eu fugiat nulla pariatur. Excepteur sint occaecat cupidatat non proident, sunt in culpa qui officia deserunt mollit anim id est laborum.”

2.2.2 Narrowband cooling stage: 689 nm

”Lorem ipsum dolor sit amet, consectetur adipiscing elit, sed do eiusmod tempor incididunt ut labore et dolore magna aliqua. Ut enim ad minim veniam, quis nostrud exercitation ullamco laboris nisi ut aliquip ex ea commodo consequat. Duis aute irure dolor in reprehenderit in voluptate velit esse cillum dolore eu fugiat nulla pariatur. Excepteur sint occaecat cupidatat non proident, sunt in culpa qui officia deserunt mollit anim id est laborum.”

2.2.3 Repumping: 481 nm

”Lorem ipsum dolor sit amet, consectetur adipiscing elit, sed do eiusmod tempor incididunt ut labore et dolore magna aliqua. Ut enim ad minim veniam, quis nostrud exercitation ullamco laboris nisi ut aliquip ex ea commodo consequat. Duis aute irure

dolor in reprehenderit in voluptate velit esse cillum dolore eu fugiat nulla pariatur. Excepteur sint occaecat cupidatat non proident, sunt in culpa qui officia deserunt mollit anim id est laborum.”

2.2.4 Optical dipole trap: 1064 nm

Discuss how our only method for evaporative cooling is through light traps since we do not have a magnetically sensitive ground state.

2.2.5 Optical toolbox

Absorption imaging system

Discuss time of flight pixel calibration as well as the optical magnification system put in place by Mi

Give timing diagram, name the first pulse the atom pulse and the second the background pulse.

Actualy diagram of the imaging system, the light path and the relation of the beam to the chamber

Give reference to section with theory but discuss the technical limitations

Absorption imaging is a destructive measurement process which is predicated on measuring the spatially distributed attenuation of laser light after passing through an atomic cloud. In this section we will discuss the technical details of the Neutral absorption system and reserve the theoretical description of the process to Sec.3.2.1.

We must consider the bit depth of the camera’s pixels, which in turn influences

the number of photons (the intensity) we can illuminate the cloud with over a certain time. this must be related to the thinness of the sample right? Thick clouds also mean multiple scatters? Find someone that discusses this idea.

The number of photons needs to be in a certain range, not too little but not too much. perhaps discuss the real world implication of counting photons (changing the exposure time)

This consideration means we generally aim for an optical depth around unity which is an order of magnitude difference the atom and background pulse.

We use such and such camera include datasheet in appendix since it is hard to find which has a double shutter function. More details can be found in the appendix some sec. We care about the timing since the laser intensity and frequency might drift between the atom and background images. Variations in intensity have straightforward implications for errors since the measurement of the atomic number density assumes the only difference between the images is due to the presence of scatters, Sec. some sec, and does not account for fluctuating photon number. Very occasionally, the Neutral apparatus will experience an underexposed shot (of either the atom or background image) that must be discarded due to large, noticeable, fluctuations. We hypothesize that these occurrences are the result of environmental perturbations (acoustic noise, vibrations through the table, spurious ground or electrical noise). However, the precise cause is unknown as the absorption imaging happens very quickly at the end of the experimental cycle when multiple systems begin to reset for the next sequence and in practice, these fluctuations do not occur often enough to be a major cause for concern.

The more insidious source of error in absorption imaging is variation of the optical frequency. Coherent, frequency stabilized radiation is used to illuminate the atom cloud so that we may control the optical absorption cross section and accurately measure the atomic number density. However, this laser light is passed through many optical components on its path to the atoms and ultimately the imaging camera. Small reflections along this path result in a multitude of interferometers which causes small scale spatial intensity variation across the beam. Exacerbating this problem are short time frequency drifts that may occur between the atom and background images which result in slightly different fringe patterns in the atom and background images. Fringes patterns are a well known nuisance in experimental AMO images and it has become routine to use linear algebra techniques to create a composite background image for each atom image during analysis [?]. A brief discussion of the principal component analysis (PCA) algorithm employed by the Neutral analysis routine is outlined below, while a more can be found in Sec. [some sec](#). Briefly, this approach is as follows:

1. Find a basis set of background images from a large set of raw background images.
2. For a single atom image, construct an initial guess at a composite background image using coefficients to weight each basis image resulting in a superposition of the basis images.
3. Segment the atom image into multiple regions by separating out the region of interest around the atom cloud.

4. Comparing similar regions between the composite background and the atom background region, perform a least-squares minimization by tweaking the weighting coefficients of the composite background.
5. Once a suitable composite background has been found, calculate the optical depth using the atomic region of interest and the corresponding region of the minimized composite background image.

This procedure is repeated for each atom image using a static background basis set that is periodically recalculated using recent background images to account for long term drifts of the apparatus. may be numerically intensive as it is done for each atom image but the results have proven remarkable for even modest computational resources.

add picture showing the fringe removal

Chirped blow away pulser

Reference Josh's master for construction

Reference Natali's(?) thesis for shelving

Discuss usage in measuring Rabi frequencies (add appendix discussing the fitting of the optical bloch equations?)

Highly tunable 689 nm spectroscopy system

Spin-manipulation laser with dynamic polarization control

2.3 Experimental control and electronics

”Lorem ipsum dolor sit amet, consectetur adipiscing elit, sed do eiusmod tempor incididunt ut labore et dolore magna aliqua. Ut enim ad minim veniam, quis nostrud exercitation ullamco laboris nisi ut aliquip ex ea commodo consequat. Duis aute irure dolor in reprehenderit in voluptate velit esse cillum dolore eu fugiat nulla pariatur. Excepteur sint occaecat cupidatat non proident, sunt in culpa qui officia deserunt mollit anim id est laborum.”

2.3.1 Computer control system

”Lorem ipsum dolor sit amet, consectetur adipiscing elit, sed do eiusmod tempor incididunt ut labore et dolore magna aliqua. Ut enim ad minim veniam, quis nostrud exercitation ullamco laboris nisi ut aliquip ex ea commodo consequat. Duis aute irure dolor in reprehenderit in voluptate velit esse cillum dolore eu fugiat nulla pariatur. Excepteur sint occaecat cupidatat non proident, sunt in culpa qui officia deserunt mollit anim id est laborum.”

2.3.2 Ancillary laboratory systems

Trim coils

Standard trim coil apparatus with the coils in a helmholtz configuration.

Used to trim out static residual B-fields and to apply dynamic and well con-

trolled external magnetic fields.

Should include the trim coils in here somewhere and discuss how to zero the B field as well as provide what the calibration factor is for the coils

Zero crossing AC line trigger

Pneumatic actuated mirror mounts

2.4 Apparatus benchmarks

”Lorem ipsum dolor sit amet, consectetur adipiscing elit, sed do eiusmod tempor incididunt ut labore et dolore magna aliqua. Ut enim ad minim veniam, quis nostrud exercitation ullamco laboris nisi ut aliquip ex ea commodo consequat. Duis aute irure dolor in reprehenderit in voluptate velit esse cillum dolore eu fugiat nulla pariatur. Excepteur sint occaecat cupidatat non proident, sunt in culpa qui officia deserunt mollit anim id est laborum.”

Chapter 3

Photoassociation in ultracold gases

3.1 Introduction

This part needs to be brief and really should motivate the idea of PAS.

PA is not unique to atomic physics, chemists have been using light to interrogate molecular structure for a long time

physicists molecule

PA can come in many forms (in a lattice, in a bulk gas, via dissociating molecules) Experimentally we observe PA by looking for trap loss [doublon paper](#).

There are multiple flavors of PAS. Can do one-photon or two-photon.

Can even be used to modify the scattering length of atoms through mixing of atomic eigenstates.

Pioneering work done in the early 90's used PA to interrogate the structure of interatomic potentials to deduce the scattering lengths between atoms.

a photoassociation experiment can be used to map the square of the scattering wave function in the ground electronic state at the Condon points corresponding to the different excited bound levels. [18] What about the history of scattering? Most of what we know about quantum mechanics comes from either scattering experiments of

spectroscopy. Definitely need some BS about how simple scattering theory has been a hallmark of atomic physics and Photoassociation spectroscopy is an important field which relies on both of these properties.

rabi oscillations between atomic and molecular condensates (cite ours and the lattice experiment that followed)

short-range PA This work is focused on long-range PA but in recent years groups have also developed short-range PA techniques for the creation of rovibrational ground state molecules. These techniques rely heavily on favorable overlap integrals between molecular wavefunctions and typically searching for favorable intermediate states is a pain (that is why our large FCF might be useful)

While the general idea of photoassociation is incredibly straightforward, a rigorous theoretical understanding of the process requires discussion of several key topics related to the behavior of ultracold gases. **fix this segue** The photoassociation process is effected by the residual kinetic energy of the atoms, external potential energy from trapping potentials, and the internal potential energy due to inter-particle scattering between atoms. In the following sections we will cover the statistical mechanics linking the atom temperature and distribution in parabolic potentials. Next we'll move to cold collisions and see the importance of the scattering wavefunction and how external fields can lead to tunable properties. Finally, we'll pull it all together and develop analytic expressions which can be used to fit spectral lineshapes and extract meaningful information from these experiments.

3.2 Theoretical description of trapped bosonic gases

Additional

This section will briefly discuss the

Need to know the spatial and momentum distribution of atoms in the trap. Concerned with space as the likelihood of PA is dependent on the interatomic separation and the overlap integral between wavefunctions plays a big role. Highest probability of excitation is near the Condon point [citations?](#)

Momentum distribution needs to be known as this affects how the wavefunction looks as well as the distribution of energies within the cloud which can lead to line-broadening and asymmetric lineshapes

Essentially first part of chapter 2 from Res

We need

Since photoassociation is a two-body process, an accurate description of the spatial

Ben This chapter will briefly cover the statistical mechanics of trapped atomic gases, both at thermal temperatures and at near-zero temperatures for bosons and fermions. In our experiment, we typically acquire data by imaging the atomic density profile either in-situ or after releasing the atoms and allowing them to freely expand for a variable time-of-flight (TOF). I will discuss the expected density profiles for these various regimes and the related fit functions that we use to extract physical information from our samples. To illustrate the properties of trapped atomic gases,

let us first consider a system in the grand canonical ensemble. For non-interacting particles at a temperature T , the average occupation of the state i with energy E_i is

Typically our samples have a fixed number of particles, N , so the chemical potential, μ , is constrained such that

In the limit of large particle number we can describe the gas semi-classically assuming that the occupation of the ground state is negligible.

The semi-classical distribution is defined such that the average number of particles in the phase-space volume $d\mathbf{p}d\mathbf{r}$ is given by $f(\mathbf{r}, \mathbf{p})d\mathbf{p}d\mathbf{r}/(2\pi)^3$ and

check the equation numbers in pethick and smith Consider the number density of atoms per phase space volume $(2\pi\hbar)^3$ integrated from $\epsilon > 0$

$$n(\mathbf{r}) = \int \frac{d\mathbf{p}}{2\pi\hbar^3} \frac{1}{\exp((E_r(\mathbf{r}) - \mu/k_B T) - 1)} \quad (3.1)$$

where we are neglecting the full quantum nature of the atoms and considering them as point masses with free particle energy $E_r(\mathbf{r}) = \frac{p^2}{2m} + V(\mathbf{r})$

next we define the quantities

$$x = \frac{p^2}{2mk_B T} z(\mathbf{r}) = e^{\mu - V(\mathbf{r})/k_B T} \quad (3.2)$$

define ξ

then performing a change of variables and plugging into above eq we find

$$n(\mathbf{r}) = \frac{2}{\sqrt{\pi}\lambda_T^3} \int dx \frac{\sqrt{x}}{z^{-1}e^x - 1} \quad (3.3)$$

where $\lambda_T = \sqrt{\frac{2\pi\hbar^2}{mk_B T}}$ is the de Broglie wavelength cite?. This integral is of a certain form and can be rewritten using cite Demarco pg 237 footnote

need to put bound on these integrals from 0 to inf where does the 3/2 come from?

$$\begin{aligned} \int_0^\infty dx \frac{x^{\gamma-1}}{z^{-1}e^x - 1} &= \sum_{n=1}^\infty \int_0^\infty dx x^{\gamma-1} e^{-nx} z^n \\ &= \Gamma(\gamma) \text{Li}_\gamma[z] \end{aligned} \quad (3.4)$$

where $\text{Li}_\gamma[z]$ is the polylogarithm function defined by cite something

$$\text{Li}_\gamma[z] = \sum_{n=1}^\infty \frac{z^n}{n^\gamma} \quad (3.5)$$

This function is also known as the bose enhancement function cite ketterle and describes the bunching of bosonic particles near degeneracy

Using this identity we can write the thermal distribution as

$$\begin{aligned} n(\mathbf{r}) &= \frac{\text{Li}_{\frac{3}{2}}[z(\mathbf{r})]}{\lambda_T^3} \\ &= \frac{1}{\lambda_T^3} \text{Li}_{\frac{3}{2}}[\exp(\mu - V(\mathbf{r})/k_B T)] \end{aligned} \quad (3.6)$$

For harmonic traps $V(\mathbf{r}) = \frac{m}{2} \sum_i \omega_i^2 r_i^2$ where r_i represents the cartesian coordinates. Plugging this into previous eq then the *in-situ* density profile is given by

$$n(\mathbf{r}) = \frac{1}{\lambda_T^3} \text{Li}_{\frac{3}{2}} \left[\xi \exp \left(\sum_i \frac{-m\omega_i^2 r_i^2}{2k_B T} \right) \right] \quad (3.7)$$

Argue what z is what is it's range?, then say that it is small when T is large.

Therefore, writing the first few terms of the series expansion of Eq.3.5

$$\text{Li}_\gamma[z] = z + \frac{z^2}{2^\gamma} + \frac{z^3}{3^\gamma} + \dots \quad (3.8)$$

we see that $\text{Li}_\gamma[z] \approx z$ for $z \ll 1$. This corresponds to the high temperature limit which should result in recovery of the MB solution and indeed it does. In the classical, or high-temperature, limit $\text{Li}_{\frac{3}{2}}[z(\mathbf{r})] \approx z(\mathbf{r})$. From Eq. we see that this that in the limiting case we get the expected Maxwell-Boltzmann density profile **what happens with ξ** . In the following we will continue to use the full expressions with an explicit dependence on the polylogarithm as it is the most general form, however, we will use this approximation to ensure our expressions match those expected from a classical Maxwell-Boltzmann description of the gas.

this can be simplified

$$n(\mathbf{r}) = \frac{\xi}{\lambda_T^3} \exp \left(\sum_i \frac{-m\omega_i^2 r_i^2}{2k_B T} \right) \quad (3.9)$$

I'd like to put in something about the momentum distribution

3.2.1 Extracting data from column densities

This description of the atoms in the trapping potential is useful but we need to go a step further because we use absorption imaging to determine properties of the atom after a time of flight.

Maybe put in something about different measurement techniques and reference the ketterle and pethick and smith again.

Removeing the trap results in ballistic expansion with the above spatial density profile as the initial conditions. To derive how we find the properties of the atoms, consider the above spatial density profile as the initial conditions.

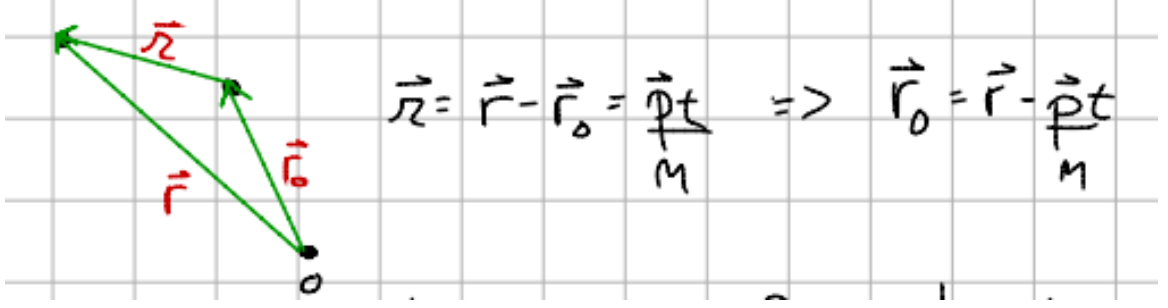


Figure 3.1 : Ballistic expansion of particles

Schematic representation particle displacement vectors used to determine how time-of-flight expansion transforms the initial density distribution

Atoms expand ballistically according to

$$\frac{d\mathbf{r}}{dt} = \frac{\mathbf{p}}{m} \text{ and } \frac{d\mathbf{p}}{dt} = 0 \quad (3.10)$$

Thus, an atom measured at position \mathbf{r} after the time-of-flight, t , will have moved a distance $\mathbf{r} = \frac{\mathbf{p}t}{m} = \mathbf{r} - \mathbf{r}_0$ from its initial position \mathbf{r}_0

make the tof density n' the spatial density evolves then double check $2\pi\hbar$ denom

$$\begin{aligned} n(\mathbf{r}, t) &= \int \frac{d^3\mathbf{r} d^3\mathbf{p}}{(2\pi\hbar)^3} \frac{1}{\exp\left(\left[\frac{p^2}{2m} + V(\mathbf{r}') - \mu\right] \frac{1}{k_B T}\right) - 1} \delta^3\left(\mathbf{r} - \frac{\mathbf{p}t}{m} - \mathbf{r}'\right) \\ &= \int \frac{d^3\mathbf{p}}{(2\pi\hbar)^3} \frac{1}{\exp\left(\left[\frac{p^2}{2m} + V\left(\mathbf{r} - \frac{\mathbf{p}t}{m}\right) - \mu\right] \frac{1}{k_B T}\right) - 1} \end{aligned} \quad (3.11)$$

Plugging in the harmonic potential we find that free expansion after release from a harmonic trap is self-similar and amounts to rescaling the the spatial coordinates by check Demarco's thesis. Thus the scaled spatial profile is given by

$$n'_{th}(\mathbf{r}, t) = \frac{1}{\lambda_T^3} \left(\prod_{j=1}^3 \frac{1}{1 + \omega_j^2 t^2} \right) \text{Li}_{\frac{3}{2}} \left[\xi \exp \left(\sum_{i=1}^3 \frac{-m\omega_i^2 r_i^2}{2k_B T} \frac{1}{1 + \omega_i^2 t^2} \right) \right] \quad (3.12)$$

Using this description of the spatial distribution after time-of-flight expansion, we must now consider how to relate our absorption measurement to the physically relevant variables of the gas.

Finally we must consider the column density along one direction since we are taking absorption images of the atoms. A brief description of absorption imaging and system used for this process is given in [some sec](#).

Simply stated, absorption imaging is the process of illuminating a gas of atoms with resonant (or near resonant) laser light and taking a spatially resolved image of the laser beam. As the light is tuned near a resonant transition, the atoms will absorb and scatter photons out of the original laser beam resulting in a "shadow" which is proportional to the number of scatters within a certain spatial region. This shadow image is then normalized by taking another picture of the laser after the atoms have fallen out of the imaging region. This relation of the light attenuation to the number density of scattering particles is known as Beer's law and results

Using Beer's law [cite](#), we can relate the total absorption of photons to the number density of scattering particles along the optical path multiplied by the absorption cross section. This results in a measurement of the "optical depth" of the gas along a column density. Measurement along a particular direction limits our description of the gas to the two-dimensional plane orthogonal to the laser beam as shown in [some fig from ch 2](#).

Experimentally, the optical depth is trivially computed by taking the natural logarithm of the ratio of the images obtained from the camera. We then equate this

OD image to be proportional to the spatial density profile after the time-of-flight expansion integrated along the optical path through the atoms.

$$\begin{aligned} \text{OD} &= \ln \left(\frac{\text{Atom Image}}{\text{Background Image}} \right) = \sigma_{abs} \int_{-\infty}^{\infty} dz n'_{th}(\mathbf{r}, t) \\ &= \frac{\sigma_{abs}}{\lambda_T^3} \left(\prod_{j=1}^3 \frac{1}{1 + \omega_j^2 t^2} \right) \int_{-\infty}^{\infty} dz \text{Li}_{\frac{3}{2}} \left[\xi \exp \left(\sum_{i=1}^3 \frac{-r_i^2}{2\sigma_i^2} \right) \right] \end{aligned} \quad (3.13)$$

where $\sigma_i^2 = \frac{k_B T}{m\omega_i^2} (1 + \omega_i^2 t^2)$. Need to say something about the integral in Eq. [prev](#) and evaluating the integral along z so going to write out the explicit spatial dependence in cartesian coordinates. Additionally, we'll rewrite the polylogarithm in terms of it's series representation in order to see an identity

$$\int_{-\infty}^{\infty} dz \text{Li}_{\frac{3}{2}} \left[\xi \exp \left(\sum_{i=1}^3 \frac{-r_i^2}{2\sigma_i^2} \right) \right] = \int_{-\infty}^{\infty} dz \sum_{n=1}^{\infty} \frac{\xi^n}{n^{3/2}} \exp \left(\frac{-x^2}{2\sigma_x^2} - \frac{y^2}{2\sigma_y^2} - \frac{z^2}{2\sigma_z^2} \right)^n \quad (3.14)$$

Defining $\rho = \exp \left(\frac{-x^2}{2\sigma_x^2} - \frac{y^2}{2\sigma_y^2} \right)$ and expanding the series out, Eq. [above](#) becomes

$$= \int_{-\infty}^{\infty} dz \xi \rho \exp \left(\frac{-z^2}{2\sigma_z^2} \right) + \frac{\xi^2}{2^{3/2}} \rho^2 \exp \left(\frac{-z^2}{2\sigma_z^2} \right)^2 + \frac{\xi^3}{3^{3/2}} \rho^3 \exp \left(\frac{-z^2}{2\sigma_z^2} \right)^3 + \dots \quad (3.15)$$

In this form we can readily separate out the dependence on z and perform the integral making use of the following identity [check identity](#) $\int_{-\infty}^{\infty} dz \sum_{n=1}^{\infty} \exp \left(\frac{-z^2}{2\sigma_z^2} \right) = \frac{\sqrt{2\pi}}{n^{1/2}} \sigma_z$.

Eq. [above](#) then reduces to

$$\begin{aligned} &= \int_{-\infty}^{\infty} dz \sum_{n=1}^{\infty} \frac{\xi^n \rho^n}{n^{3/2}} \exp \left(\frac{-z^2}{2\sigma_z^2} \right) \\ &= \sqrt{2\pi} \sigma_z \underbrace{\sum_{n=1}^{\infty} \frac{\xi^n \rho^n}{n^2}}_{\text{Li}_2[\xi \rho]} \end{aligned} \quad (3.16)$$

We are now ready to plug this result for the integral back into the full expression for the optical depth. Retaining the explicit expression in cartesian coordinates,

Eq. [above](#) becomes

$$OD(x, y) = \frac{\sqrt{2\pi}}{\lambda_T^3} \frac{\sigma_{abs}\sigma_z}{(1 + \omega_x^2 t^2)(1 + \omega_y^2 t^2)(1 + \omega_z^2 t^2)} \text{Li}_2 \left[\xi \exp \left(\frac{-x^2}{2\sigma_x^2} - \frac{y^2}{2\sigma_y^2} \right) \right] \quad (3.17)$$

This equation still has one unknown, σ_z , that we cannot readily measure. This problem is solved by recognizing that we can readily calculate and measure a specific value of Eq. [something](#), namely the peak optical depth (OD_{peak}) located at $x = 0, y = 0$.

$$OD_{\text{peak}} = \frac{\sqrt{2\pi}}{\lambda_T^3} \frac{\sigma_{abs}\sigma_z}{(1 + \omega_x^2 t^2)(1 + \omega_y^2 t^2)(1 + \omega_z^2 t^2)} \text{Li}_2[\xi] \quad (3.18)$$

thus the relation between the measured optical depth and the spatial density distribution is given by

$$OD(x, y) = \frac{OD_{\text{peak}}}{\text{Li}_2[\xi]} \text{Li}_2 \left[\xi \exp \left(\frac{-x^2}{2\sigma_x^2} - \frac{y^2}{2\sigma_y^2} \right) \right] \quad (3.19)$$

and in the limit of long expansion time during time-of-flight, namely $t \gg \omega_x^{-1}, \omega_y^{-1}, \omega_z^{-1}$ then the measured widths reduce to $\sigma_i^2 = \frac{k_B T}{m} t^2$ and the atom temperature is given along each axis by

$$T_i = \frac{m\sigma_i^2}{k_B t^2} \quad (3.20)$$

Regarding the assumption that the expansion time is much greater than the trap frequencies, we should note that limiting factors in the expansion time are due to center of mass motion of the cloud under the influence of gravity. In the Neutral apparatus we typically utilize drop times are ≈ 30 ms. For shallow traps, where ω_i is be small, then the atoms may not have enough time during expansion to achieve fully ballistic expansion. In these cases it is typical to quote temperatures of the sample as measured along the tightest axis of confinement.

Last thing to do is to relate our expression for optical depth and number density to the total number of atoms in the trap. This task is straightforward by recalling the boson normalization requiriement

$$\begin{aligned}
 N &= \int_{-\infty}^{\infty} d^3\mathbf{r} n_t h(\mathbf{r}) = \int_{-\infty}^{\infty} d^3\mathbf{r} n_t h'(\mathbf{r}, t) \\
 &= \int_{-\infty}^{\infty} d^3\mathbf{r} \frac{\sigma_{abs}}{\lambda_T^3} \frac{1}{(1 + \omega_x^2 t^2)(1 + \omega_y^2 t^2)(1 + \omega_z^2 t^2)} \sum_{n=1}^{\infty} \frac{\xi^n}{n^{3/2}} \exp\left(\frac{-x^2}{2\sigma_x^2} - \frac{y^2}{2\sigma_y^2} - \frac{z^2}{2\sigma_z^2}\right)^n
 \end{aligned} \tag{3.21}$$

This equation is the same problem we saw above but integrated over all axes instead of just one. Therefore we can apply the same expansion and identity we employed to solve for the optical depth to find

$$N = \frac{(2\pi)^{3/2}}{\lambda_T^3} \frac{\sigma_x \sigma_y \sigma_z}{(1 + \omega_x^2 t^2)(1 + \omega_y^2 t^2)(1 + \omega_z^2 t^2)} \text{Li}_3[\xi] \tag{3.22}$$

From our expression for the optical depth, Eq. [some](#), we can simply this to

$$N = \frac{2\pi\sigma_x\sigma_y}{\sigma_{abs}} \text{OD}_{\text{peak}} \frac{\text{Li}_3[\xi]}{\text{Li}_2[\xi]} \tag{3.23}$$

Eq. [above](#)

All of our information comes from taking pictures of our atomic clouds and inferring the physical properties of the gas before the time-of-flight expansion. This is possible since we know the density profile of the gas in-situ. In the absence of external fields, other than gravity, turning off the trapping potential results in ballistic expansion described by $\mathbf{r} = \mathbf{r}_0 + \frac{\mathbf{p}^2}{2m}t$, where \mathbf{r}_0 and \mathbf{p} are the position and momentum at the moment of release from the trap and t is the expansion time. Neglecting the center-of-mass motion due to gravity and assuming long expansion times, then we

can easily find a regime where $\frac{p^2}{2m}t \gg r_0$ and therefore

$$\mathbf{r} \approx \frac{p^2}{2m}t \quad (3.24)$$

This

[?] [get demarco thesis?](#). Thus, for atoms

Thus, for atoms starting at a position \mathbf{r}_0

Density profile expands self-similarly

Time of flight is essentially a Fourier transform which turns the initial momentum information into spatial information.

3.3 Characterizing cold collisions

3.3.1 Low energy scattering

this results in a potential that supports bound states. In atomic physics, our low density gases are mainly within the regime of small interactions. This spatial dependence is mapped onto the internal energy levels of each atom. I want to say dressed state model here (review atom-photon coupling, atomic physics book).

consider the two particle system as a single entangled particle long range part of this quasi-particle is just the eigenstates of the separate particles themselves (only composed of two parts) but the short range part is going to be determined by some complex physics (new eigenstates, what is the coupling mechanism?) the vdW point is the boundary distance? coupling is due to the interatomic potential, there is at least the long-range part falling off as R^{-6} , what are the types of interactions which

make up the internal wall?

Think I want to introduce the photoassociation by talking about the collisional wavefunction

what will that do?

I want to build up ideas about the FCF and need the wf for that to get qf I have to go back to scattering theory

ideas of the wavefunction become that basis for how you want to talk about interacting potentials

free atoms scattering as single particle state (different eigenstate) interaction determined by some gnarly stuff From scattering theory we know that the long range behavior is determined by short range physics how do we know this? (the dalibard intro) Can we come up with good enough pseudo potentials to describe the short range physics and then solve the schrodinger equation to extract wavefunctions? we want wavefunctions because that is the full characterization we don't know the right eigenbasis for the short range part but we can make some guesses (in particular Hund cases setup eigen states for various possible internal states) Bohn and Julienne theory guessed based on using quantum defect theory this pre-supposes that the bound and free wavefunctions are similar (I forget in what respect) but that the bound ones must go to zero as $R \rightarrow \infty$ If we have some notion of the wf then we can construct matrices which define interactions once we add additional coupling to the scattering problem

now in a position where I need to connect scattering theory and the PAS

Once we have the ground state wavefunction of our new particle we can con-

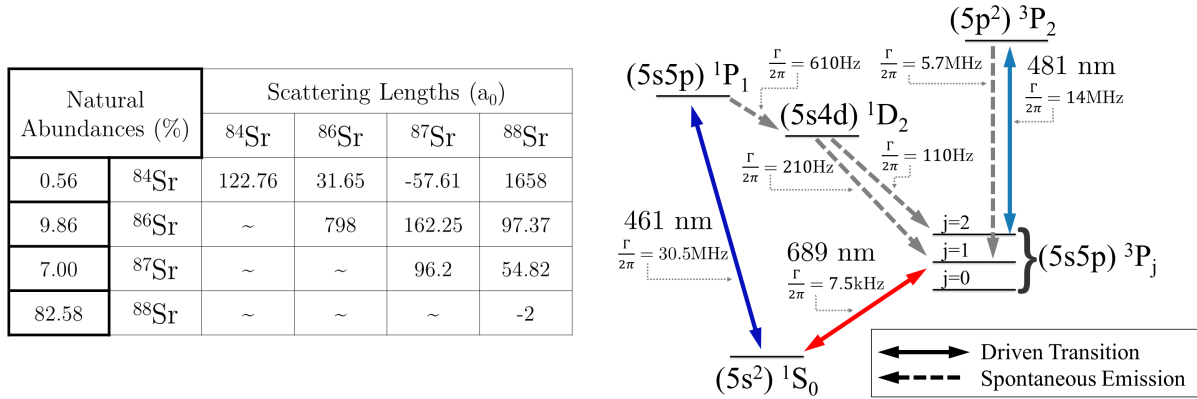


Figure 3.2 : Strontium interatomic wavefunctions

Res 6.3

struct the internal structure by considering the internal energy structure of the constituent atoms Can I make a connection that since it is a composite particle we must consider all the various configurations available?

3.3.2 Modifying interactions with external fields

Also the Chin '10 review on feshbach resonances

Follow the Nicholson 15 paper method of introing the elastic and inelastic cross sections

The use of a laser field as the coupling scheme in a Feshbach resonance introduces several advantages and complexities that must be considered when determining the expected properties of optical Feshbach molecules. In order to understand these differences, we will briefly outline the key concepts behind Feshbach resonances and the distinctions between optical and magnetic Feshbach resonances.

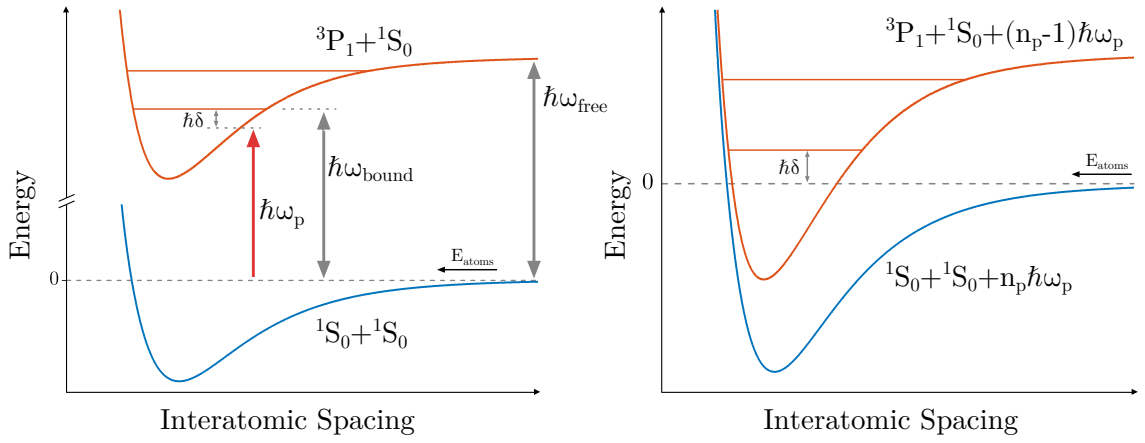


Figure 3.3 : Schematic representation of a Feshbach resonance

(a) Potentials for the open ($^1S_0 + ^1S_0$) and closed ($^3P_1 + ^1S_0$) channel of an optically coupled Feshbach resonance in strontium. (b) The same coupling shown in (a) in the dressed state model. Tuning of the excited potential is achieved by varying the laser frequency detuning, $\delta = \omega_p - \omega_{\text{bound}}$, and ω_{free} is the $^1S_0 \rightarrow ^3P_1$ atomic transition frequency.

The basic idea of a Feshbach resonance is outlined in Fig. ?? . Consider a simple two channel system, denoted by the open channel and the closed channel. The open channel is generally a ground state potential for two free atoms near threshold. Atoms occupying this state can undergo elastic collisions and, in the absence of any external perturbation, will remain in the open channel. Conversely, the closed channel is a bound state of a higher lying potential whose energy can be tuned relative to the open channel. In the absence of coupling between the states, the open and closed channel remain eigenstates of the system as the tuning parameter, and therefore the energy of the closed channel, is changed. However, in the presence of coupling between the channels, the original eigenstates are mixed and develop an avoided crossing between the bare open and closed channels, when tuned across the resonance. The power of Feshbach resonances comes from the ability to externally manipulate the degree of state mixing, which results in control of the s-wave scattering length and the creation of low energy Feshbach molecules.

Magnetic Feshbach resonances (MFR) are used extensively in alkali metal systems to tune the scattering properties of ultracold gases since the ground states of these systems feature a magnetic moment due to an unpaired electron in the valence shell. Thus, MFRs utilize interactions between low lying ground state molecular potentials via spin-dependent couplings. Since both the open and closed channel are ground state potentials, MFRs often exhibit extraordinarily long lifetimes [4, 5]. Conversely, in strontium the ground state is a 1S_0 state, as shown in Fig. 1.4. This state is not magnetically sensitive, so no MFRs exist near the $^1S_0+^1S_0$ interatomic potential. Fortunately, optical Feshbach resonances (OFR) serve as another method to introduce

coupling between the ground state potential (open channel) and a molecular state of an electronically excited potential (closed channel). Our work has utilized coupling between the $^1S_0 + ^1S_0$ and $^3P_1 + ^1S_0$ two-body potentials via the narrow $^1S_0 \rightarrow ^3P_1$ atomic transition at 689nm. Fig. ?? shows a schematic of the potentials involved in the OFR of strontium in both the bare atomic and dressed state pictures. In the dressed basis we consider the combined atom + photon field system such that the channels become $|^1S_0 + ^1S_0 + n_p \hbar \omega_p\rangle$ as the open channel and $|^3P_1 + ^1S_0 + (n_p - 1) \hbar \omega_p\rangle$ for the closed channel. As the light field frequency, ω_p , is varied the excited closed channel potential will experience an energy shift relative to the open channel, resulting in resonant coupling between the open and closed channels. [19, 20?]

Both MFRs and OFRs can be treated by the same theoretical formalism, as a modification of the collisional properties between two particles [21, 4]. One of the hallmarks of ultracold physics is the simplicity of atomic collisions. As bosonic atoms get colder they can only collide via $\ell = 0$ partial waves and thus the elastic collision rate between two atoms becomes energy independent and can be parameterized by a single fixed quantity, a_s . This parameter is known as the s-wave scattering length and is determined by the short range molecular potential between two colliding atoms. Through a similar approach, collisions near Feshbach resonances can be modeled by introducing a complex s-wave scattering length, $\tilde{\alpha}$. In this model, the magnitude of $\tilde{\alpha}$ influences the elastic scattering rate between particles while the imaginary part describes losses through inelastic scattering. Under an isolated Feshbach resonance model at low energies, this complex scattering length is given by [4]

$$\tilde{\alpha} = a - ib = \frac{a_s \Gamma_0}{-E_0 + i(\gamma/2)} \quad (3.25)$$

where E_0 and Γ_0 are the energy independent parameters for, respectively, the resonance position and coupling strength between channels, and γ is a general decay term associated with loss from the closed channel. Using Eq. 3.25, we can note the two main differences between MFRs and OFRs. Most experimentally useful MFRs, such as in Li and K, have negligible closed channel decay, $\gamma = 0$, and a fixed coupling strength between the open and closed channels. Thus, the change in the s-wave scattering length takes on a particularly simple form,

$$\tilde{\alpha} = a_s \left(1 - \frac{\Delta}{B - B_0} \right) \quad (3.26)$$

where B_0 is the resonance position and the coupling strength is parameterized by a magnetic width Δ , such that $\Gamma_0 = \delta\mu\Delta$ with $\delta\mu$ the difference in magnetic moments between the open and closed channel.

Conversely, OFRs offer the possibility to tune the coupling strength between the open and closed channel, since the coupling depends on the transition matrix element which varies with the square root of laser intensity. Furthermore, since OFRs utilize electronically excited states which have a natural lifetime, γ is nonzero. This results in inelastic loss processes for OFRs. Similar to MFRs, we can define the change in scattering length as [21, 22, 23]

$$\tilde{\alpha} = a_s \left(1 - \frac{w\delta}{\delta^2 + \gamma^2/4} + \frac{i}{2} \frac{w\gamma}{\delta^2 + \gamma^2/4} \right) \quad (3.27)$$

where $\delta = \omega - \omega_0$ is the detuning from the chosen photoassociation resonance at ω_0 as shown in Fig. ??, and the width of the resonance is defined by $w = -\ell_{opt} \gamma / a_s$.

Typically, the strength of OFRs are characterized by their optical length [21, 4] given by $\ell_{opt} = a_s \Gamma_0 / \gamma = \frac{\lambda_{OFR}^3}{16\pi c} \frac{|\langle n|E \rangle|^2}{k} I$. Here c is the speed of light, λ_{OFR} is the wavelength

of the coupling laser, and $|\langle n|E\rangle|^2$ is the free-bound Frank-Condon factor between the bound state $\langle n|$ and scattering state $|E\rangle$. Additionally, it is useful to identify the real and imaginary parts of Eq. 3.27 as defined in Eq. 3.25.

$$a_{OFR} = a_s + \ell_{opt}\gamma \frac{\delta}{\delta^2 + \gamma^2/4} \quad b_{OFR} = \frac{\ell_{opt}}{2} \frac{\gamma^2}{\delta^2 + \gamma^2/4} \quad (3.28)$$

Our previous work exploring the use of an optical Feshbach resonance took advantage of photoassociation transitions with large optical lengths to control the scattering length of an ^{88}Sr BEC as described by Eq. 3.27. However, all studies of OFR to date have been limited by large atom loss rates [24, 25, 26, 23, 22] which can be modeled as a density evolution, $\dot{n} = -K_{in}n^2$, where K_{in} is the two-body inelastic loss rate constant. In the low energy limit, $k \rightarrow 0$, the inelastic loss rate is given by

$$K_{in} = \frac{8\pi\hbar}{\mu_r} b_{OFR} = \frac{4\pi\hbar}{\mu_r} \frac{\ell_{opt}\gamma^2}{\delta^2 + \gamma^2/4} \quad (3.29)$$

where μ_r is the reduced mass, δ is the laser detuning as shown in Fig. ??.

3.4 Modeling of photoassociation lineshapes

This section will concern the general theory used to describe photoassociative spectra. While a full quantum close-coupling calculation is the most complete and rigorous method for analyzing cold quantum scattering problems, useful approximations can be applied to realize relatively more "simple" closed analytic formulas describing photoassociation spectra.

ideas of limiting cases that can be explored with PAS [27]

3.4.1 One-photon excitation of free to bound transitions

PAS near narrow intercombination transitions

3.4.2 Extension to two-color spectra

Now that we have the theory of PAS covered.

This section will cover the theory of lineshapes in PAS.

Somewhere I read about three regimes of PAS as a comparison of relevant energy scales. Should explore that here

$$N(t) = \frac{N_0 e^{-\Gamma t}}{1 + \frac{2N_0 \langle K \rangle V_2}{\Gamma V_1^2} (1 - e^{-\Gamma t})} \quad (3.30)$$

where N_0 is the number at the beginning of the PAS interaction time, and $\langle K \rangle$ indicates a spatial average of collision event rate constant K (Eq. 4.4). The one-body loss rate, Γ , is due to background collisions and off-resonant scattering from the PA lasers.

PA loss is described with a local equation for the evolution of the atomic density [Eq. (4.1)]. Integrating Eq. (4.1) over the trap volume yields the time evolution of the number of trapped atoms [Eq. (4.2)]. The effective volumes used throughout this analysis are defined by

$$V_q = \int_V d^3r e^{-\frac{qU(\mathbf{r})}{k_B T}}, \quad (3.31)$$

for trapping potential $U(\mathbf{r})$. The collision event rate constant can be expressed as a thermal average of the scattering probability for loss, $|S(\epsilon, \omega_1, \omega_2, \dots, \mathbf{r})|^2$, over the collision energy ϵ . We also average over the trap volume to allow for the possibility

that the scattering probability can vary with position in the trap due to inhomogeneity of laser intensity profiles and the density distribution [Eq. (4.4)].

$$\begin{aligned} \langle K \rangle &= \frac{1}{V_2} \int_V d^3r e^{-\frac{2U(\mathbf{r})}{k_B T}} \\ &\times \frac{1}{h Q_T} \int_0^{U_{max}-U(r)} d\epsilon |S|^2 e^{-\epsilon/k_B T}. \end{aligned} \quad (3.32)$$

where the partition function is $Q_T = \left(\frac{2\pi k_B T \mu}{h^2}\right)^{3/2}$ for reduced mass μ .

Bohn and Julienne [?] provide an expression for $|S(\epsilon, \omega_1, \omega_2, \dots)|^2$ for a collision on the open channel of two ground state atoms (g) with total energy ϵ leading to loss-producing decay from the excited state b_1 with rate γ_1 . (See Fig. 4.1.) It yields

$$\begin{aligned} |S|^2 &= \\ &\frac{(\Delta_2 + \epsilon/\hbar)^2 \gamma_1 \gamma_s}{\left[(\Delta_1 + \epsilon/\hbar)(\Delta_2 + \epsilon/\hbar) - \frac{\Omega_{12}^2}{4}\right]^2 + \left[\frac{\gamma_1 + \gamma_s}{2}\right]^2 (\Delta_2 + \epsilon/\hbar)^2}, \end{aligned} \quad (3.33)$$

where all quantities are defined in the main text. For simplicity, we have omitted the light shift of b_1 due to coupling to the scattering continuum [?]. Equation (4.5) neglects all light shifts due to the trapping laser. Light shifts due to the photoassociation lasers coupling to states outside our model (Fig. 4.1) are also neglected. The thermal energy is much greater than the zero-point energy for trap motion, $T \gg \hbar \nu_{\text{trap}}/k_B$, so confinement effects are negligible [?].

and lights shifts of states 0 and 2 are approximately equal and will cancel in the determination of the binding energy of the halo state, E_2 [? 28]. Neglecting

For the experiments reported here, we maintain significant intermediate-state detuning, $|\Delta_1| \gg |\Omega_{12}|$. Thus we are in a Raman configuration, and near two-photon

resonance the expression for the scattering probability for a given initial scattering energy Eq. (4.5) can be approximated as a Lorentzian

$$|S|^2 \approx \frac{A(\epsilon)}{\left(\Delta_2 + \epsilon/\hbar - \frac{\Omega_{12}^2}{4(\Delta_1 + \epsilon/\hbar)}\right)^2 + [\Gamma_L(\epsilon)/2]^2}, \quad (3.34)$$

where A and Γ_L are defined in Eqs. (4.8) and (4.9).

As discussed in the text, we analyze loss spectra using the effective expression, Eq. (4.10) to account for possible deviations from the single-channel theory [?].

The total 689-nm intensity oscillates with 100% contrast according to $I_{total} = I_1 + I_2 + 2\sqrt{I_1 I_2} \cos[(\omega_1 - \omega_2)t] = 2I \{1 + \cos[(\omega_1 - \omega_2)t]\}$. Equation 4.16 The form of the AC Stark shift due to excitation lasers in Eq. 4.11 reflects the time average of the intensity and neglects the interference term. To confirm that this is the correct description, we numerically solved the time-evolution for a three-level system with similar optical couplings and oscillating optical intensity as present during halo photoassociation. The Hamiltonian is

$$H = \quad (3.35)$$

$$\begin{pmatrix} 0 & \Omega_{01} [\cos(\omega_1 t) + \cos(\omega_2 t)] & 0 \\ \cdot & E_{b1} & \Omega_{12} [\cos(\omega_1 t) + \cos(\omega_2 t)] \\ \cdot & \cdot & E_{b2} \end{pmatrix}$$

For $\Omega_{01} \ll \Omega_{12} \ll \Delta_1 \equiv E_{b1}/\hbar - \omega_1$, which is analogous to the experimental conditions used here

, the shift of the two-photon resonance condition follows $\delta = \Omega_{12}^2/2\Delta_1$ in agreement with Eq. 4.16.

Chapter 4

Binding energy of the $^{86}\text{Sr}_2$ halo molecule

4.1 Probing the ground state potential

Strontium is a nice atom to work with because of the various properties of all of its isotopes but access to such a variety of properties also comes with its share of complications. The most abundant isotope, 88, has a nearly vanishing scattering length but served as the workhorse for many of our previous studies and those of other labs. The known scattering properties of strontium are mass scaled from 88 **is this somehow not as good for 86? Also, where are the most up to date scattering lengths for Sr from? - The '10 Fourier paper** but by probing the 86 ground state potential directly we can obtain a more accurate measurement of the 86-86 scattering length.

Additionally, by utilizing the narrow intercombination potential we are able to detune many linewidths from the intermediate state, thereby

Two-photon photoassociation

umm, I want to write something about the narrow line letting us probe this but

As described in previous chapters, two-photon PAS can be used to directly populate low-lying molecular levels. Applying this technique to strontium 86 we can

explore a similar regime

conclusion of chapter 4 is that we measured the binding energy more accurately which can be directly related to a more precious value of the scattering length for ^{86}Sr . Also there is a straightforward experiment available to use to attempt to measure the efimov paramter for strontium.

how did we determine the binding energy? how did we measure spectra?

Weakly bound ground-state dimers are of great interest in ultracold atomic and molecular physics. In the extreme case of a scattering resonance, the least-bound state represents an example of a quantum halo system [29] with spatial extent well into the classically forbidden region. Halo molecules show universality, meaning that molecular properties such as size and binding energy can be parameterized by a single quantity, the s -wave scattering length a , independent of other details of the atom-pair interaction [30, 31]. For potentials that asymptote to a van-der-Waals form, an additional parameter, the van der Waals length l_{vdW} , can be introduced for a more accurate description. Efimov trimers also exist in systems near a scattering resonance, influencing dimer and atomic scattering properties and introducing additional universal phenomena [32, 33]. Ultracold halo molecules are often associated with magnetic Feshbach resonances [?], for which the scattering state and a bound molecular state can be brought near resonance by tuning a magnetic field.

Here we study the least-bound vibrational level of the $X^1\Sigma_g^+$ electronic ground state of the $^{86}\text{Sr}_2$ dimer (Fig. 4.1), which is a naturally occurring halo molecule, meaning it exists in the absence of tuning with a magnetic Feshbach resonance. A well-

known example of a naturally occurring halo molecule is the $^4\text{He}_2$ dimer [34, 35, 30]. The least-bound vibrational level of the ground state of $^{40}\text{Ca}_2$, which was recently studied using similar methods [36], is also very close to this regime.

There are important differences between halo molecules associated with magnetic Feshbach resonances and the naturally occurring halo molecule in ^{86}Sr . With magnetic Feshbach resonances, the relevant scattering and bound molecular states lie on different molecular potentials, and single-photon magnetic-dipole transitions can be used to measure molecular binding energies with RF or microwave spectroscopy [? 37?]. Typically, this is done by first forming molecules through magneto-association and then driving bound-free or bound-bound transitions converting the halo molecule into a different state. Other methods include spectroscopy with an oscillating magnetic field [?], a modulated optically controlled Feshbach resonance [38], and Ramsey-type measurements of atom-molecule oscillation frequencies [39]. It is also possible to efficiently populate halo states with a magnetic-field sweep [40] or evaporative cooling [41] near a magnetic Feshbach resonance [?]. These are powerful techniques for manipulating quantum gases of alkali metals and other open-shell atoms, for which there are many magnetic Feshbach resonances. Strontium, however, due to its closed-shell electronic structure, lacks magnetic Feshbach resonances in the electronic ground state.

In this work, we probe the halo state in ^{86}Sr using two-photon Raman photoassociation (PA) [?], in which two laser fields couple colliding atoms to the least-bound state of the ground molecular potential. We tune near resonance with an intermediate state that is bound in the 0_u potential corresponding to the $^1S_0 + ^3P_1$ asymptote

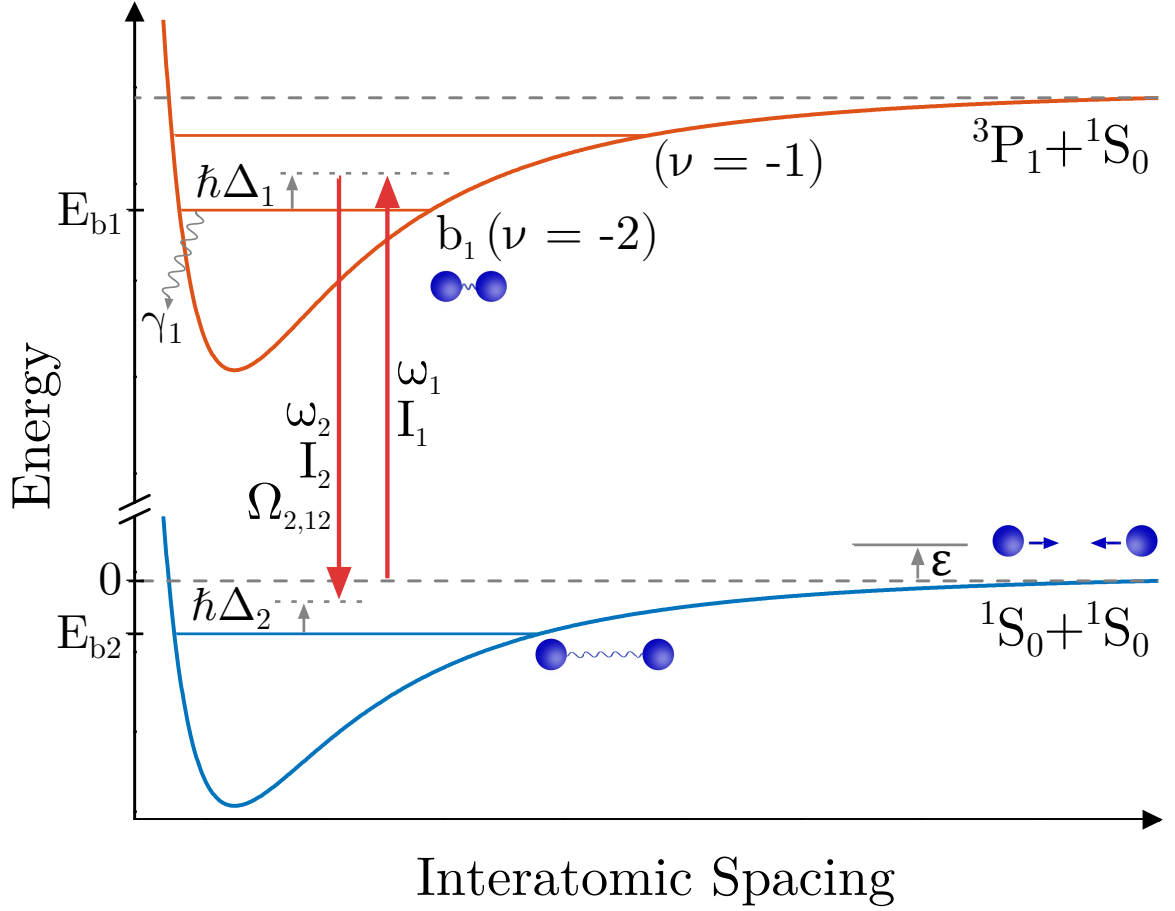


Figure 4.1 : Strontium PAS potential

Two-photon photoassociation diagram . The energy of two well-separated 1S_0 atoms at rest is taken as zero. ϵ is the kinetic energy of the colliding atom pair. E_{b1} is the unperturbed energy of the bound state of the excited molecular potential that is near resonance with the free-bound laser, which in these experiments is the second-least bound level of the excited molecular potential ($\nu = -2$). E_{b2} (< 0) is the unperturbed energy of the least bound state of the ground molecular potential. The photon of energy $\hbar\omega_1$ is detuned from E_{b1} by $\hbar\Delta_1$ for $\epsilon = 0$, while the two-photon detuning from E_{b2} is $\hbar\Delta_2$. The decay rate of b_1 is γ_1 . Stark and collisional frequency shifts are neglected in this schematic.

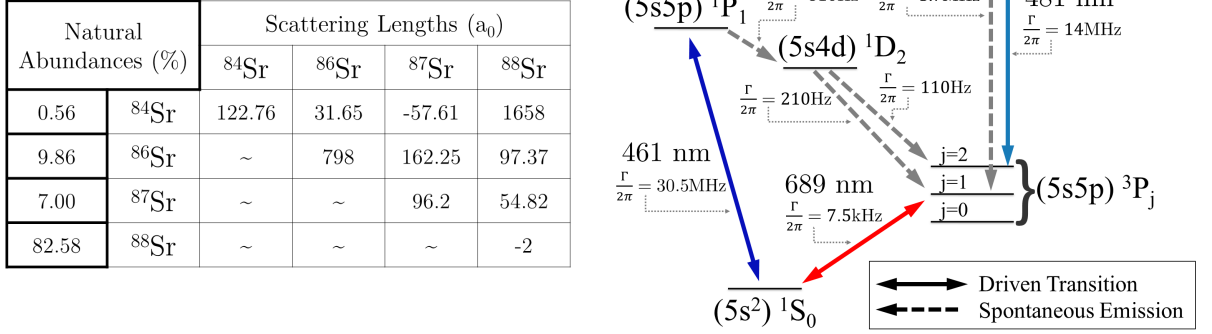


Figure 4.2 : Strontium two-photon photoassociation

fig 1 from the halo paper

at long range [?] (Fig. 4.1). We accurately determine the $^{86}\text{Sr}_2$ binding energy, considering possible collisional frequency shifts and AC Stark shifts due to trapping and excitation lasers. Using the universal prediction for the binding energy, including corrections derived for a van der Waals potential [42, 43, 44], we derive a more accurate value of the s -wave scattering length for ^{86}Sr atomic collisions [45?].

4.2 Experimental setup

In this work, we probe the halo state in ^{86}Sr using two-photon Raman photoassociation (PA) [cite 16 from halo paper](#), in which two laser fields couple colliding atoms to the least-bound state of the ground molecular potential. We tune near resonance with an intermediate state that is bound in the $0u$ potential corresponding to the $^1S_0 + ^3P_1$ asymptote at long range as shown in Fig.4.2.

Photoassociation experiments follow the same general prescription. We start

by trapping through the normal sequence as outlined in [some section](#). Then we evaporate down to the final trap depth. After evaporation

The two-photon PAS experiments described in the following chapters are performed under similar conditions but due to complications with the neutral vacuum system we performed the binding energy experiments using the Rydberg apparatus. While non-ideal from a consistency point of view, this did allow us to replicate and validate our previous findings which gives us great confidence in the robustness of this experimental approach.

The most significant difference between the two apparatus' is the trapping characteristics of the optical dipole traps and the beam parameters of the photoassociation beam. These differences are noted in the corresponding chapters but here we will outline the timing and generic characteristics that are shared between the two experiments.

Table [something](#) shows the relevant experimental parameters and typical values for our photoassociation experiments.

Specific details of the optical dipole traps, PA beam parameters, and using a completely different a

performed on ultracold Sr atoms in a single-beam optical dipole trap (ODT) generated from a 1064-nm laser propagating perpendicular to gravity. Typical atom numbers are several hundred thousand and peak densities are $\approx n_0 = 1 \times 10^{12} \text{ cm}^{-3}$. The number of atoms and sample temperature are measured using time-of-flight absorption imaging described in [some section](#). Trap oscillation frequencies are deter-

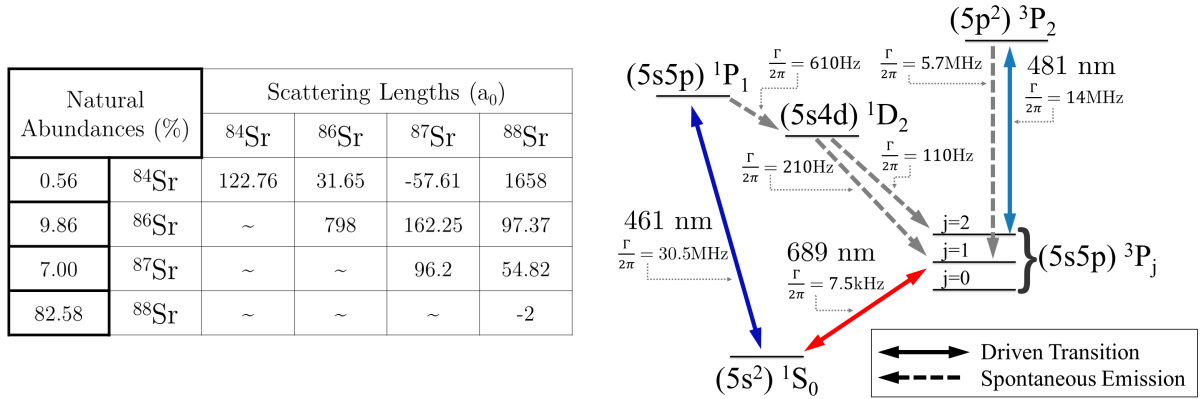


Figure 4.3 : Schematic of PAS light generation

Properties of strontium. Left: Natural abundances and s-wave scattering lengths for all mixtures of Sr. Right: Simplified energy level diagram of Sr showing the relevant states used for trapping and cooling of the atomic gas

mined by measuring dipole and breathing collective mode frequencies, which allow determination of trap volume and sample density

For experiments done on our apparatus we generate the two photon source as shown in Fig???. Light comes from an injection locked slave diode which follows the frequency stablized 689 master laser described in [some section](#). THis light is modulated via a single acousto-optic modulator (AOM) driven with two frequencies and coupled into a single-mode polarization maintaining optical fiber. THis fiber output is luanched near the science chamber and the light output level is continuously monitored via a beam sampler and photodiode placed between the fiber output and the chamber.

Primary reasons why we can't scan large distances. There will be a slight

misalignment of the beams into the fiber and the RF may start to fall off. For these experiments an AOM with a center frequency of 90 MHz was used.

This simple system has many advantages and a couple of drawbacks. Since both photons are aligned into the same fiber then they are guaranteed to have the same output wavevector and therefore the two photon process will be doppler free (since the absorption and emission processes will exactly cancel each other out).

This is a simple system for generating multiple frequencies which are guaranteed to share the same wavevector, phase coherence, and gross frequency stability. Use of the AOM provides highly accurate control of the difference frequency with RF precision.

While versatile and simple, we are worried about the balance of the RF power onto the AOM. These devices are narrowband modulators (simple ones)

We see a reduction in contrast when the two drive frequencies differ by more than ≈ 250 kHz.

Since the modulator is a narrowband device, scanning

great care is taken to ensure the maximum amount of contrast is visible on the photodiode. This

As described in [some section](#) the slave laser is frequency stabilized at +42 MHz of the $^{86}\text{Sr } ^1S_0 \rightarrow ^3P_1$ atomic transition. The AOM then shifts the light the remaining ≈ 86 MHz to set the detuning around the $\nu = -2$ bound state of the $^1S_0 + ^3P_1$ potential. Setting of Δ_1 is done by removing one of the frequencies, peaking up the diffraction angle and alignment into the fiber.

During the course of our experiments we found that mild environmental perturbations (loud noises, air currents due to fans, etc.) to the fiber resulted in slow variation of the light coupling through the fiber. Such amplitude modulations are not uncommon in laser systems and can typically be compensated for by using a closed loop locking mechanism. However, after construction of such a power lock the components did not react quickly enough and there was a significant overshoot which resulted in an uncontrolled amount of light illuminating the atoms during short exposures. This led us to implement a digital based sample and hold mechanism for reduced intensity variability. This system is described in detail in [some section](#). The sample and hold system in combination with the power lock provided intensity stability with a standard 5% standard deviation during a typical experiment. Fig shows a typical histogram of the recorded intensities.

Make sure to discuss how I scanned the rf frequencies since there is a difference to increasing the freq difference. Since we used the -1 order of the AOM, increasing the frequency of the drive relative to the gross actually lowered the amount of energy in the system, resulting in effectively scanning Δ_1 instead of keeping it fixed. This resulted in a slight variation of the AC stark shift from the intermediate state that can be seen in the strong coupling experiments that are discussed in [some section](#).

The beat signal of the two light fields after the fiber is monitored on a photodiode and the rf powers are adjusted to ensure matched intensities for the two frequency components ($I_1 = I_2 \equiv I$).

Regarding the general process

Natural Abundances (%)		Scattering Lengths (a_0)			
		^{84}Sr	^{86}Sr	^{87}Sr	^{88}Sr
0.56	^{84}Sr	122.76	31.65	-57.61	1658
9.86	^{86}Sr	~	798	162.25	97.37
7.00	^{87}Sr	~	~	96.2	54.82
82.58	^{88}Sr	~	~	~	-2

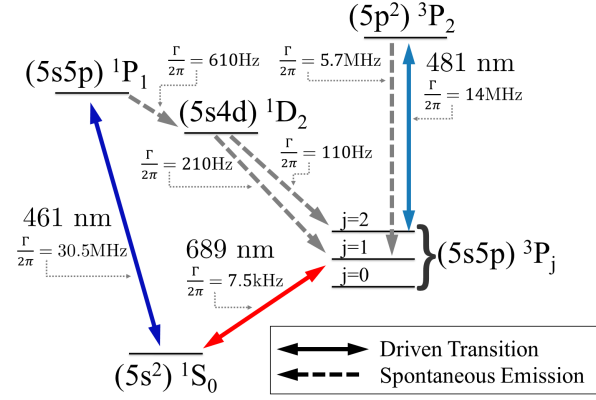


Figure 4.4 : Histogram of PAS beam intensity variation

One of the histograms from onenote. There are separate histograms for each experimental run (I should combine this so I don't have to discuss)

Natural Abundances (%)		Scattering Lengths (a_0)			
		^{84}Sr	^{86}Sr	^{87}Sr	^{88}Sr
0.56	^{84}Sr	122.76	31.65	-57.61	1658
9.86	^{86}Sr	~	798	162.25	97.37
7.00	^{87}Sr	~	~	96.2	54.82
82.58	^{88}Sr	~	~	~	-2

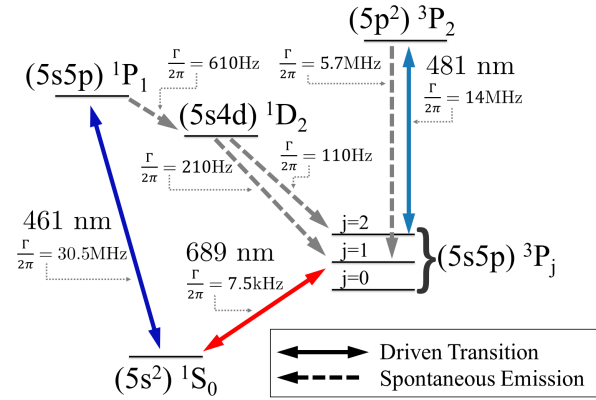


Figure 4.5 : Characteristic view of the PA beatnote

This is the picoscope plot of the beatnote

Using the $^1S_0 + ^3P_1$ interatomic potential, we perform a raman process using the $\nu = -2$ bound state which has a binding energy of $E_b = -44\text{MHz}$ [cite improved binding en.](#) Sample pre

We used strontium 86 in a thermal gas at temperatures between 30 and 1000 nK. Typical peak densities were around $n_0 = 1 \times 10^{12} \text{ cm}^{-3}$.

Raman process using the second bound state of the $^1S_0 + ^3P_1$ interatomic potential

What atom do we use what is the sample conditions what trap do we use what are the dimensions of the trap what are the trap freq how do we determine

Two-photon spectroscopy is performed on ultracold ^{86}Sr atoms in a single-beam optical dipole trap (ODT) generated from a 1064-nm laser propagating perpendicular to gravity with beam waists of $260 \mu\text{m}$ and $26 \mu\text{m}$ [? ?]. The tight waist provides vertical confinement. The trap depth after an evaporative cooling stage determines the sample temperature, which is set between $30 - 1000 \text{ nK}$. Typical atom numbers are several hundred thousand and peak densities are as high as $2 \times 10^{12} \text{ cm}^{-3}$. The number of atoms and sample temperature are measured using time-of-flight absorption imaging operating on the $^1S_0 - ^1P_1$ transition. Trap oscillation frequencies are determined by measuring dipole and breathing collective mode frequencies, which allow determination of trap volume and sample density.

4.2.1 Photoassociation

After the atoms have equilibrated in the final ODT configuration, the PA lasers are applied (Fig. 4.1). A single acousto-optic modulator, driven with two RF frequencies,

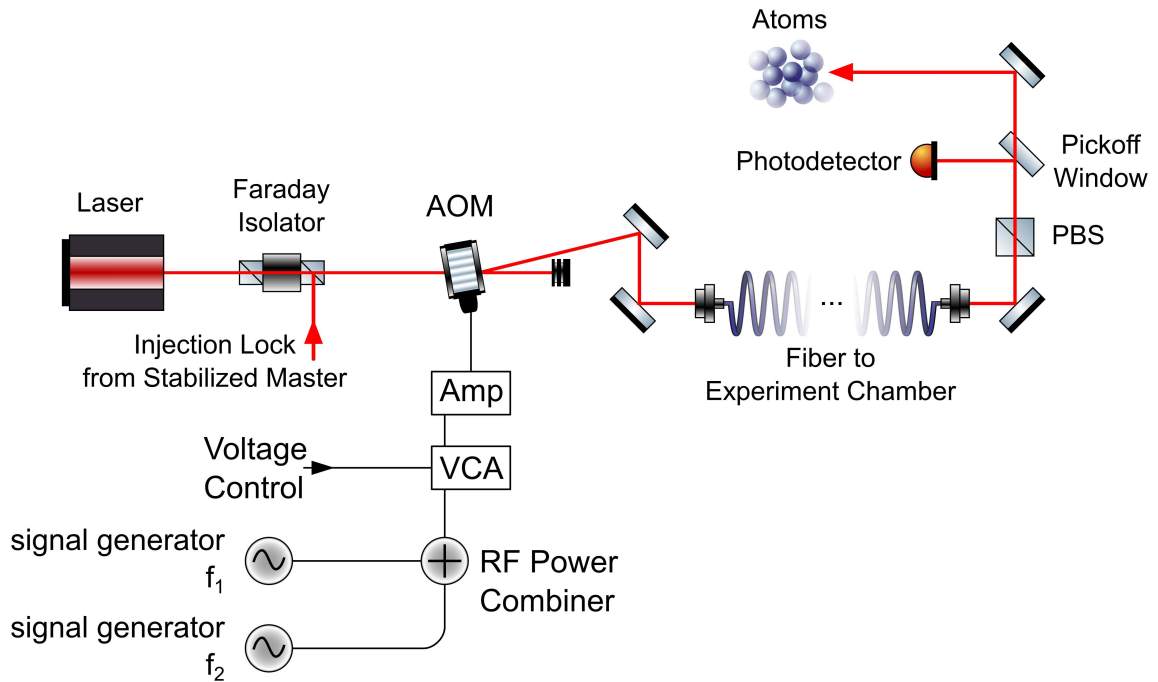


Figure 4.6 : PAS laser setup

Photoassociation laser schematic . A master laser is frequency-stabilized via saturated absorption spectroscopy to the 1S_0 - 3P_1 atomic transition. After amplification with a diode slave laser, light at two controllable frequencies is generated with a single acousto-optic modulator (AOM) and delivered to the atoms with an optical fiber. The beat note between the two frequencies is monitored after the fiber.

is used to generate both PA beams. Light is derived from a frequency-stabilized master laser (Fig. 4.2) and coupled into a single-mode optical fiber with output optics that yield a $320\text{ }\mu\text{m}$ waist at the atoms, much larger than the size of the atom cloud. Both PA beams are linearly polarized along the same direction. The beat signal of the two light fields after the fiber is monitored on a photodiode and the RF powers are adjusted to ensure matched intensities for the two frequency components ($I_1 = I_2 \equiv I$).

The sample temperature is low enough that collisions are entirely *s*-wave. The target state for the two-photon transition has total angular momentum $J = 0$ and binding energy $E_{b2}(< 0)$. ^{86}Sr has no nuclear spin and a 1S_0 electronic ground state, leading to a single ground electronic molecular potential ($X^1\Sigma_g^+$). The dominant intermediate state (b_1) is the $J = 1$ rotational state of the second least-bound ($\nu = -2$) vibrational level on the 0_u^+ molecular potential, which asymptotically connects to the 1S_0 - 3P_1 atomic transition at long range. This state is bound by $44.246(10)$ MHz [?]. We define $\Delta_1 = \omega_1 - E_{b1}/\hbar$ and $\Delta_2 = \omega_1 - \omega_2 - E_{b2}/\hbar$ as the one-photon detuning from state b_1 and two-photon detuning from state b_2 respectively for an initial scattering state with collision energy $\epsilon = 0$. $\Omega_{2,12}$ is the Rabi frequency for coupling between states b_1 and b_2 due to the laser field at ω_2 with single-beam intensity I_2 . Because the binding energy of the halo molecule is very small compared to Δ_1 , both laser frequencies are near resonance with the $\nu = -2$ state. The transitions to the least-bound ($\nu = -1$) $J = 1$ excited molecular state, bound by $1.633(1)$ MHz, and the excited atomic state lie near enough in energy that they can effect our observations.

Photoassociation leads to loss of atoms from the trap through radiative decay from the intermediate, excited electronic state, and from collisions between molecules

and background atoms. The PA spectrum is obtained by holding ω_2 fixed and varying ω_1 , which varies Δ_2 across resonance (Fig. 4.1). Δ_1 thus also varies slightly during a scan, but the spectra are so narrow compared to Δ_1 that we neglect this in our analysis. After an exposure time on the order of one hundred milliseconds, the number of ground-state atoms remaining and the sample temperature are measured with time-of-flight absorption imaging.

4.2.2 Consideration of the trap depth

Show plots of the trap and how we determined what the trap depth was

Our previous discussion of the rate loss constant assumed we could describe the spatial distribution of the atomic density profile analytically. This is a valid supposition given two key assumptions, 1) the sample temperature remains constant during the PA exposure and 2) the trap is of sufficient depth that we can reasonably approximate it as a harmonic trap. [cite Mi's trap paper](#).

Analysis of the trapping conditions after acquisition of the data revealed that this second assumption was not maintained during our experiment. In some figure we can see that we only have an η of 2. This is troublesome as it means we must numerically consider the density distribution over space when solving for the rate loss constant K .

In addition to the modified spatial distribution, we must also consider the effect of the trap depth on the energy profile of the trapped gas. In a typical high- η trap, a typical Boltzmann profile is sufficient to describe the velocity distribution of the atoms and when we consider the distribution of relative energies that is important

for PAS experiments, we recover a simple boltzmann weighting for the distribution of energy probabilities. This is shown in [some app](#).

However, the case of a low-eta trap we must define a local cutoff energy at each point in space within the trap as atoms that have an energy higher than the local eta value are assumed to be lost from the trap. Derivation of this truncated relative energy probability distribution is given in [some app](#) and results in a stronger weighting of the coldest atoms near the bottom of the trap.

4.3 Theoretical description

This section develops the more groddy form of the BJ equation. Include the

In Ch. [somewhere](#) we discussed the usual situation for observing loss due to photoassociation. This experiment was similar to the 88 autler townes experiment.

PA loss is described with a local equation for the evolution of the atomic density

$$\dot{n} = -2Kn^2 - \Gamma n, \quad (4.1)$$

where the laser-frequency dependence of the collision-event rate constant, K , determines the spectrum of the PA loss. The one-body loss rate, Γ , is due to background collisions and off-resonant scattering from the PA lasers. By integrating this equation over the trap volume, we can obtain the evolution of the total number of trapped atoms

$$N(t) = \frac{N_0 e^{-\Gamma t}}{1 + \frac{2N_0 \langle K \rangle V_2}{\Gamma V_1^2} (1 - e^{-\Gamma t})} \quad (4.2)$$

where N_0 is the number of trapped atoms at the beginning of the PAS interaction

time. The effective trap volumes V_q are

$$V_q = \int_V d^3r e^{-\frac{qU(\mathbf{r})}{k_B T}}, \quad (4.3)$$

for trapping potential $U(\mathbf{r})$. $\langle K \rangle$ is the trap-averaged collision event rate constant

$$\begin{aligned} \langle K \rangle &= \frac{1}{V_2} \int_V d^3r e^{-\frac{2U(\mathbf{r})}{k_B T}} \\ &\times \frac{1}{h Q_T} \int_0^{\epsilon_{\max}(\mathbf{r})} d\epsilon |S|^2 e^{-\epsilon/k_B T}, \end{aligned} \quad (4.4)$$

which is itself a thermal average of the scattering probability for loss ($|S(\epsilon, \omega_1, \omega_2, \dots, \mathbf{r})|^2$) over the collision energy ϵ , with an energy cutoff ϵ_{\max} to be discussed momentarily. The trapping potential is given by $U(\mathbf{r}) = mgz + h\chi_{1064,g}I_{1064}(\mathbf{r}) - \tilde{U}_{\min}$, where mgz is the gravitational potential at height z , $I_{1064}(\mathbf{r})$ is the intensity of the trapping light, and $\chi_{1064,g} = 11 \text{ Hz}/(\text{W}/\text{cm}^2)$ [?] is proportional to the polarizability of ground state atoms due to 1064 nm light. \tilde{U}_{\min} is subtracted to set the potential at the trap minimum to zero. The spatial integral is restricted to regions around the trapping local minimum with $U(\mathbf{r})$ less than the trap depth [?]. Downhill regions on the other side of the saddle point defining the trap depth are excluded. The laser intensity profile is measured independently, and the potential is found to be consistent with measured trap oscillation frequencies. The partition function is $Q_T = \left(\frac{2\pi k_B T \mu}{h^2}\right)^{3/2}$ for reduced mass $\mu = m/2$ and sample temperature T , for atoms of mass m .

Equation (4.4) provides the correct thermal average when the collision-energy distribution does not need to be truncated ($\epsilon_{\max} \rightarrow \infty$). For our data, however, the ratio of sample temperature to trap depth is $k_B T / U_{\text{depth}} \approx 3$ for samples with temperature above 100 nK and drops to unity for 30 nK samples, so truncation effects are important. If the single-particle kinetic-energy distribution function is a Boltzmann

truncated at $U_{\text{depth}} - U(\mathbf{r})$, then the collision-energy distribution follows a Boltzmann distribution at low energies [$\epsilon \ll U_{\text{depth}} - U(\mathbf{r})$] and falls off more quickly at larger energies, reaching zero at $2[U_{\text{depth}} - U(\mathbf{r})]$. We find that this treatment predicts a narrower distribution on the red side of the spectral line than we observe in our data, suggesting the presence of atoms in non-ergodic orbits with energies above the saddle point of the trap. This is not surprising given the large collisional loss rate associated with near-resonant scattering in this isotope. Fortunately, the molecular binding energy is strongly determined by the sharp edge of the spectrum on the blue side of the line, which is relatively insensitive to the description of the red tail. Our data is fit well with a truncated Boltzmann distribution of collision energies [Eq. (4.4)]. To estimate the systematic uncertainty introduced by this treatment, we perform fits with ϵ_{max} equal to $2[U_{\text{depth}} - U(\mathbf{r})]$ and $U_{\text{depth}} - U(\mathbf{r})$ and take the mean of the two results as the best value for the binding energy and half the difference as a systematic uncertainty $\sigma_{\epsilon_{\text{max}}} \approx 100$ Hz. This procedure does not correctly represent the overall normalization of $\langle K \rangle$, but we are not concerned with overall signal amplitude in this study. Atom temperatures vary by no more than 20% during the interaction time, so assuming a constant sample temperature is reasonable.

Bohn and Julienne [?] provide an expression for $|S(\epsilon, \omega_1, \omega_2, \dots)|^2$ for a collision on the open channel of two ground state atoms (g) with total energy ϵ leading to loss-producing decay from the excited state b_1 with rate γ_1 (Fig. 4.1),

$$|S|^2 = \frac{(\Delta_2 + \epsilon/\hbar)^2 \gamma_1 \gamma_s}{\left[(\Delta_1 + \epsilon/\hbar)(\Delta_2 + \epsilon/\hbar) - \frac{\Omega_{12}^2}{4} \right]^2 + \left[\frac{\gamma_1 + \gamma_s}{2} \right]^2 (\Delta_2 + \epsilon/\hbar)^2}. \quad (4.5)$$

For simplicity, we have omitted the light shift of b_1 due to coupling to the scattering

continuum [?]. This approach was found to be sufficient for describing two-photon spectroscopy to a more deeply bound molecular level in ^{88}Sr [?]. Equation (4.5) neglects all light shifts due to the trapping laser. Light shifts due to the photoassociation lasers coupling to states outside our model (Fig. 4.1) are also neglected. The thermal energy is much greater than the zero-point energy for trap motion, $T \gg h\nu_{\text{trap}}/k_B$, so confinement effects are negligible [?]. $\gamma_1 = 2\gamma_{\text{atomic}}$, where $\gamma_{\text{atomic}} = 4.7 \times 10^4 \text{ s}^{-1}$ is the decay rate of the atomic 3P_1 level. $\gamma_s(\epsilon)$ is the stimulated width of b_1 due to coupling to the initial scattering state by laser 1, which for low energy can be expressed as [46? , 36]

$$\gamma_s(\epsilon) = 2kl_{\text{opt}}\gamma_1, \quad (4.6)$$

where the optical length ($l_{\text{opt}} \propto I_1$) is related to the overlap between the initial colliding state and b_1 , and $k = (2\mu\epsilon)^{1/2}/\hbar$. We take the intermediate state b_1 as the $\nu = -2$ state, for which $l_{\text{opt}}/I = (1.5 \pm 0.3) \times 10^4 a_0/(\text{W}/\text{cm}^2)$ [?], where $a_0 = 5.29 \times 10^{-11} \text{ m}$ is the Bohr radius.

For the experiments reported here, we maintain significant intermediate-state detuning, Δ_1 , for which $|\Delta_1| \gg |\Omega_{2,12}|$. Thus we are in a Raman configuration, and not in the Autler-Townes regime [?]. In the Raman regime, Eq. 4.5 shows a maximum near two-photon resonance at $\Delta_2 + \epsilon/\hbar = \Omega_{2,12}^2/4\Delta_1$. Following a treatment discussed recently for a similar experiment in calcium [36], if the detuning is restricted to near two-photon resonance then $|S|^2$ can be approximated as a Lorentzian

$$|S|^2 \approx \frac{A(\epsilon)}{\left(\Delta_2 + \epsilon/\hbar - \frac{\Omega_{12}^2}{4(\Delta_1 + \epsilon/\hbar)}\right)^2 + [\Gamma_L(\epsilon)/2]^2}, \quad (4.7)$$

where

$$A(\epsilon) = \frac{\Omega_{2,12}^4 \gamma_1 \gamma_s(\epsilon)}{16(\Delta_1 + \epsilon/\hbar)^4} \quad (4.8)$$

$$\Gamma_L(\epsilon) = \frac{\Omega_{2,12}^2 [\gamma_1 + \gamma_s(\epsilon)]}{4(\Delta_1 + \epsilon/\hbar)^2}. \quad (4.9)$$

In practice, the variation of collision energy is negligible compared to the one-photon detuning Δ_1 .

There are several concerns regarding the rigorous application of the Bohn and Julienne theory [?] to our experiment. The obvious one is that it assumes an isolated intermediate state, which is not always a good approximation because of the proximity of state b_1 to the $^1S_0 + ^3P_1$ asymptote and to the $\nu = -1$ state. Because of the small decay rate γ_1 of the intermediate molecular state associated with metastable 3P_1 atomic state, we also expect that loss from the ground molecular state cannot be neglected.

The more subtle issue is that Eq. (4.7) is derived assuming only a single laser beam is near resonant with each leg of the two-photon transition, which is not a good approximation for two-photon spectroscopy of a halo state and the resulting small laser-frequency difference $\omega_1 - \omega_2 \approx -E_{b2} \ll |\Delta_1|$. We can expect that coupling between pairs of states due to both photoassociation lasers will contribute to the transition strength and light shifts of the levels induced by the photassociation lasers [? ?].

In the absence of a more complete theory treating these effects, we analyze loss spectra using the effective expression given by Eq. (4.10), where the observed molecular binding energy (E'_{b2}) includes any perturbations due to AC Stark or collisional

$$|S|^2 = \frac{\Gamma_L(\epsilon) + \gamma_{\text{eff}}}{\Gamma_L(\epsilon)} \times \frac{\eta A(\epsilon)}{(\omega_1 - \omega_2 + \epsilon/\hbar - E'_{b2}/\hbar)^2 + \left[\frac{\Gamma_L(\epsilon) + \gamma_{\text{eff}}}{2} \right]^2}, \quad (4.10)$$

shifts.

Parameters have been added in Eq. (4.10) to account for deviations of the signal strength (η) and width (γ_{eff}) from the predictions of [?]. If deviations from Eq. (4.7) are small, we expect $\eta \sim 1$, $\gamma_{\text{eff}} \sim 0$, and $E'_{b2} \sim E_{b2} + \Omega_{2,12}^2/4(\Delta_1 + \epsilon/\hbar)$.

Light shifts (AC Stark shifts) due to the trapping lasers and collisions with ground-state atoms (density n) should contribute to shifts of molecular resonance. Similar effects were taken into account in a recent, high-precision study of weakly bound molecular states of ultracold ytterbium atoms [47]. In addition, we expect that both 689-nm excitation lasers will shift the line, not just $I_2 \propto \Omega_{2,12}^2$. We model the relationship between the measured resonance positions and the unperturbed binding energy E_{b2} as

$$E'_{b2} = E_{b2} + h\chi_{689}I_{689} + h\chi_{1064}I_{1064}(\mathbf{r}) + h\chi_n n(\mathbf{r}). \quad (4.11)$$

The susceptibilities, in Hz per unit intensity or density, will be determined from experimental data or theoretical considerations. The variation with position of the trapping laser intensity (I_{1064}) and the density give rise to the spatial dependence of $|S|^2$ and the need for a spatial average in Eq. (4.4). We take I_{689} as twice the single-beam intensity $I_{689} = 2I$. The 689-nm excitation beam is large enough compared to the atom sample to neglect spatial variation. The functional form for the AC Stark shift due to the excitation lasers is discussed in Sec. ??.

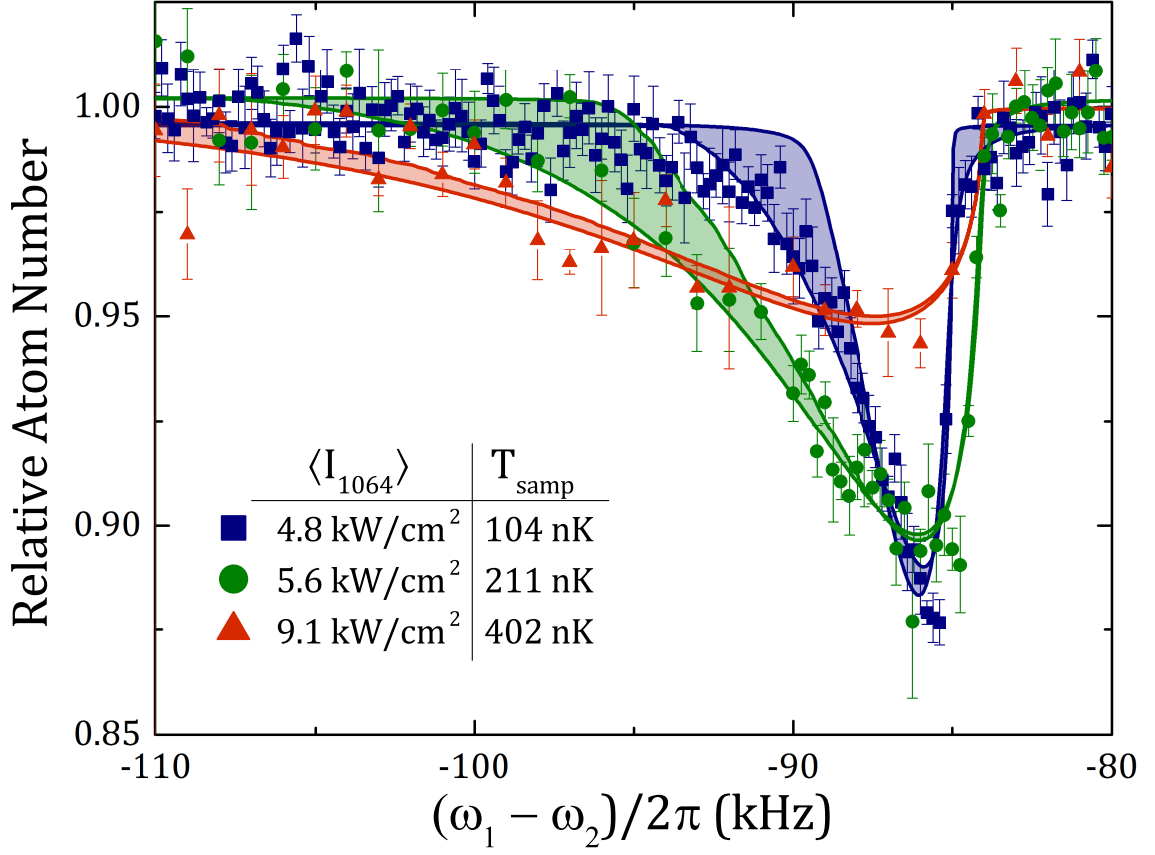


Figure 4.7 : Variation of 1064 nm trap depth

Atom-loss spectra as a function of two-photon difference frequency $(\omega_1 - \omega_2)/2\pi$ for intermediate detuning $\Delta_1/2\pi = -9$ MHz. Sample temperature and average trapping laser intensity are indicated in the legend. The single-beam excitation laser intensity is $I = 25$ mW/cm² for the 104 nK spectrum and $I = 48$ mW/cm² for the 211 nK and 402 nK spectra. Fits are described in the text, with the two boundaries of each band given by the fits with collision-energy truncation ϵ_{max} equal to $2[U_{\text{depth}} - U(\mathbf{r})]$ and $U_{\text{depth}} - U(\mathbf{r})$.

4.4 Spectral fitting and determination of energy shifts

Figure 4.3 shows a series of spectra for different final trap depths and sample temperatures. The characteristic asymmetric lineshape for excitation of a thermal sample is evident, with width decreasing as sample temperature decreases. The molecular binding energy is close to the sharp edge on the blue side of each spectrum.

We fit atom-loss spectra with Eq. (4.2) for the evolution of atom number with time, using the phenomenological expression Eq. (4.10) for the scattering probability and Eq. (4.4) for the average of the collision event rate constant over the trap volume and collision energy. The sample temperature, perturbed resonance frequency E'_{b2} , η , and γ_{eff} are taken as fit parameters. In the final analysis, temperatures are set to values determined from time-of-flight imaging of the atoms, but when they are allowed to vary, the fit values differ by no more than 10%. Approximately 10 spectra are recorded for each set of experimental parameters, and the spread of resulting fit values are used to determine best values and uncertainties.

4.4.1 AC Stark shift due to excitation lasers

The most significant perturbation to the resonance position is the AC Stark shift due to the excitation laser intensity, as shown in Fig. 4.4.1. For this data, the trap parameters, temperature ($T = 30 \text{ nK}$), and initial peak sample density ($n_0 = 2 \times 10^{12} \text{ cm}^{-3}$) are held constant. We vary the single-beam excitation intensity from $I = 0.02 - 0.06 \text{ mW/cm}^{-2}$, and the excitation time is 50 ms. The observed shifts are comparable to the thermal width of the spectrum, allowing a precise determination of $\chi_{689} = -21(1)(2) \text{ kHz/(W/cm}^2\text{)}$ from a linear fit to the resonance positions, $E'_{b2} \propto$

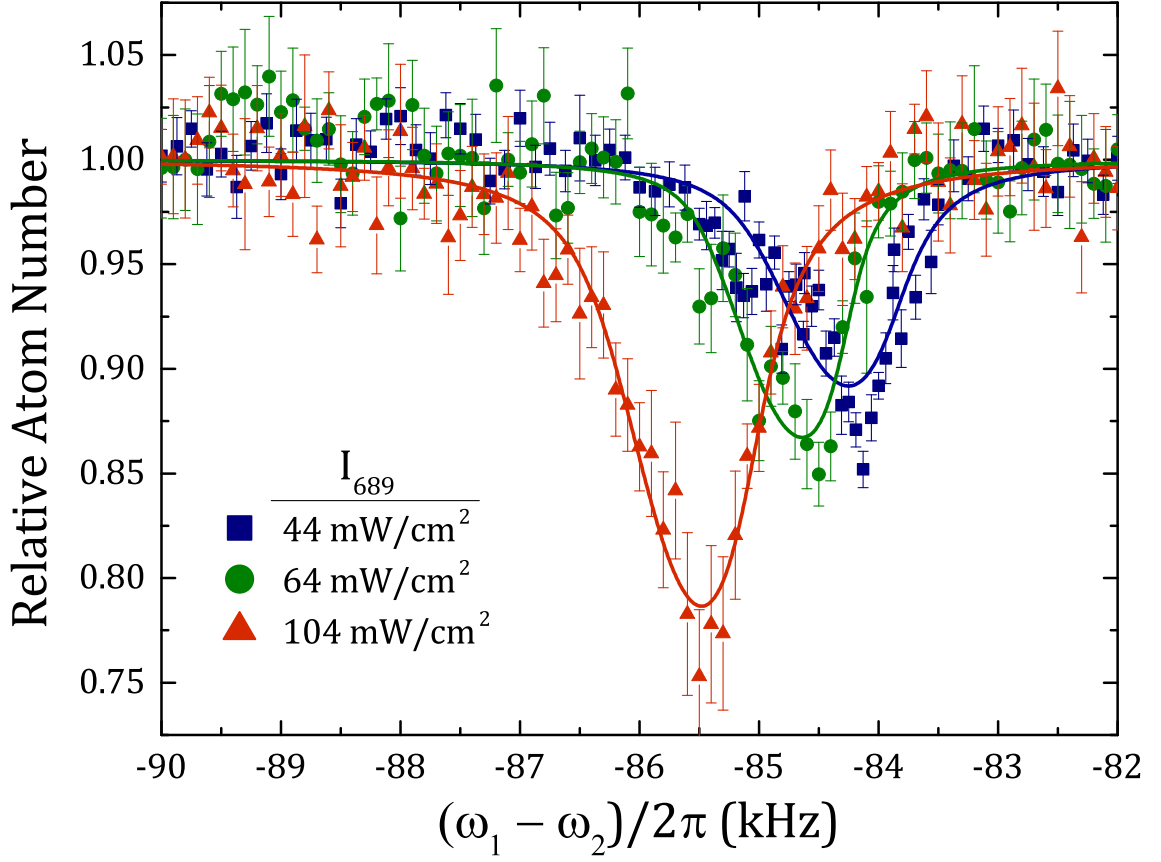


Figure 4.8 : Variation of 689 nm excitation

Atom-loss spectra as a function of two-photon difference frequency $(\omega_1 - \omega_2)/2\pi$ for intermediate detuning $\Delta_1/2\pi = -9$ MHz and various 689-nm excitation laser intensities. Twice the single-beam intensity $I_{689} = 2I$ is indicated in the legend.

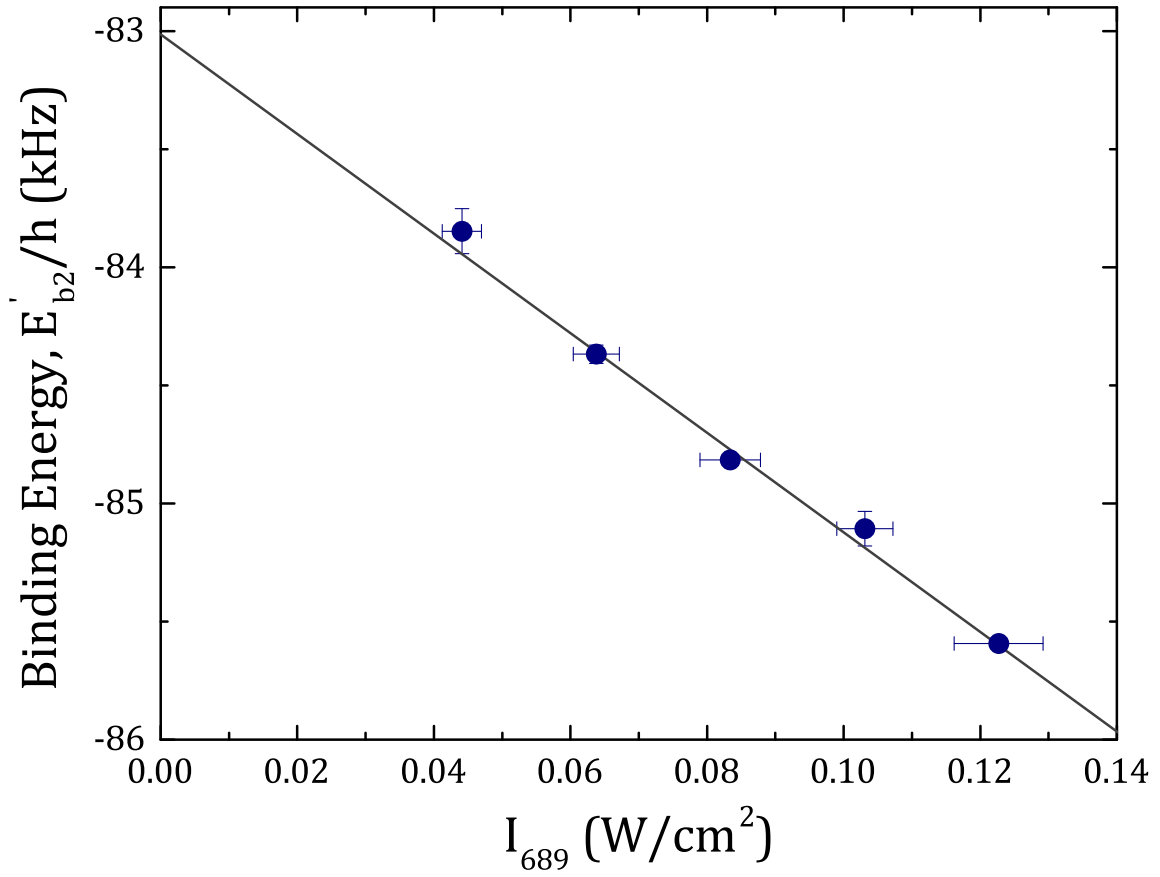


Figure 4.9 : Fit of 689 nm AC Stark shift

Measured resonance position E'_{b2} plotted versus twice the single-beam intensity $I_{689} = 2I$. The linear fit provides the AC Stark shift parameter χ_{689} .

$h\chi_{689}I_{689}$ (Fig. 4.9). The first quoted uncertainty is statistical and it arises from variations in parameters and fluctuations in the measured intensity during the scans. The second value is systematic, reflecting uncertainty in laser-beam size and intensity profile at the atoms. All parameters beside the 689-nm laser intensity are held fixed for this data set, and the AC Stark shift is not correlated with any other variable, such as density or trap intensity. We thus obtain an accurate measure of χ_{689} without attempting to account for other systematic shifts of E'_{b2} in this data. A study of the dependence of χ_{689} on detuning from the excited molecular state will be discussed in Sec. ??.

Broadening to the red of the spectrum reflects the distribution of atom-atom collision energies, while broadening to the blue is most sensitive to decay of the intermediate state (Γ_L) and the phenomenological broadening term γ_{eff} [Eqs. (4.9) and (4.10)]. The long lifetime of the excited state and the significant detuning Δ_1 result in a width $\Gamma_L(\epsilon)$ less than 5 Hz for all conditions. This is extremely small compared to observed width, which yields values of γ_{eff} on the order of 300 Hz. We hypothesize that this width reflects decay of molecules in the electronic ground-state due to collisions with background atoms.

4.4.2 Density-dependent frequency shift

A shift of the two-photon resonance position is possible due to differing mean-field shifts of initial atomic and final molecular states arising from interaction with the background of ground-state atoms. Such a shift would be proportional to the atom density and depend upon the s -wave scattering lengths for atom-atom and atom-

dimer collisions, a_{86} and a_{ad} respectively. This was observed in a Rb Bose-Einstein condensate (BEC) in [48]. For a non-degenerate gas, this effect yields $\chi_n = \hbar(\frac{a_{ad}}{\mu_{ad}} - 4\frac{a_{86}}{\mu_{aa}}) = \frac{\hbar}{m}(\frac{3}{2}a_{ad} - 8a_{86})$, where μ_{ad} and μ_{aa} are the reduced masses for molecule-atom and atom-atom collisions respectively. Note that the shift would vanish for $a_{ad} = (16/3)a_{86}$.

The largest density used in our experiment ($\sim 1 \times 10^{12} \text{ cm}^{-3}$) is relatively low compared to typical BEC densities, and at this time we are unable to accurately measure a variation of resonance position with density. However, the atom-atom scattering is close to resonance and thus Efimov physics can provide information on a_{ad} [32, 33] and an estimate of the systematic error introduced by any residual density-dependent frequency shifts. For a zero-range interaction, the atom-dimer scattering length is related to the atom-atom scattering length through the three-body Efimov parameter κ_* according to [32]

$$a_{ad} = a_{86} \{1.46 + 2.15 \cot[s_0 \ln(14.1 \kappa_* a_{86})]\} \quad (4.12)$$

where $s_0 = 1.006$ *.

In principle, the atom-dimer scattering length can take any value. However, for a deep atom-atom potential, such as for the ground-state strontium dimer [45], there is a universality of the three-body physics that sets $\kappa_* = 0.226(2)/l_{\text{vdW}}$ [49]. Here, $l_{\text{vdW}} = (2\mu C_6/\hbar^2)^{1/4}/2 = 74.6 a_0$ is the van der Waals length associated with the C_6 coefficient of the long-range Sr_2 ground-state potential. We use $C_6 = 3.03(1) \times 10^{-76}$

The Efimov parameter is related to E_{3b}^0 through $\kappa_ = (m|E_{3b}^0|/\hbar^2)^{1/2}$, where E_{3b}^0 is the binding energy the lowest Efimov trimer would have in the case of resonant atom-atom interactions.

J m^6 found from a fit of potential parameters to spectroscopic data [45], which is consistent with a recent *ab initio* calculation [50]. This yields $\kappa_* = 5.72 \times 10^7 \text{ m}^{-1} = (330 a_0)^{-1}$. Equation (4.12) then predicts $a_{\text{ad}} = 6.4 a_{86}$, which leads to a small density-dependent frequency shift parameter of $\chi_n = 50 \text{ Hz}/(10^{12} \text{ cm}^{-3})$. A numerical calculation including a finite-range correction for the atom-atom interaction [51] results in $a_{\text{ad}} = 3.5 a_{86}$ and $\chi_n = -90 \text{ Hz}/(10^{12} \text{ cm}^{-3})$. Thus, a very small shift is expected for the densities used here. We incorporate $\chi_n = 0 \pm 90 \text{ Hz}/(10^{12} \text{ cm}^{-3})$ as a set parameter in our model of the spectrum, where we set the systematic uncertainty to reflect the spread of theory predictions. This uncertainty will be significant for our determination of the unperturbed halo binding energy.

4.4.3 AC Stark Shift due to Trapping Lasers

With an accurate determination of χ_{689} and a value for χ_n , we use the data shown in Fig. 4.3 to determine the susceptibility for the AC Stark shift from the trapping laser, χ_{1064} , and the unperturbed halo binding energy E_{b2} . Figure 4.4.3 shows a plot of $E'_{b2} - \chi_{689} I_{689} - \chi_n \langle n \rangle$ versus $\langle I_{1064} \rangle$, where E'_{b2} is the resonance position from each fit and $\langle \dots \rangle$ indicates a weighted average of the quantity over the trapped sample, with a weighting given by the square of atom density. This weighting reflects the contribution to photoassociative loss, a two-body process. The plotted uncertainties in $E'_{b2} - \chi_{689} I_{689} - \chi_n \langle n \rangle$ are from statistical variation in the fit parameters. The typical average density is $\langle n \rangle \approx 1 \times 10^{12} \text{ cm}^{-3}$. The linear fit function is to $E_{b2} + \chi_{1064} \langle I_{1064} \rangle$. In addition to statistical uncertainty, we have systematic uncertainty from χ_n and treatment of the truncation of the collision-energy integral [Eq. (4.4)]. The dashed lines shown in Fig. 4.4.3 are resulting fits when the values of $E'_{b2} - \chi_{689} I_{689} - \chi_n \langle n \rangle$

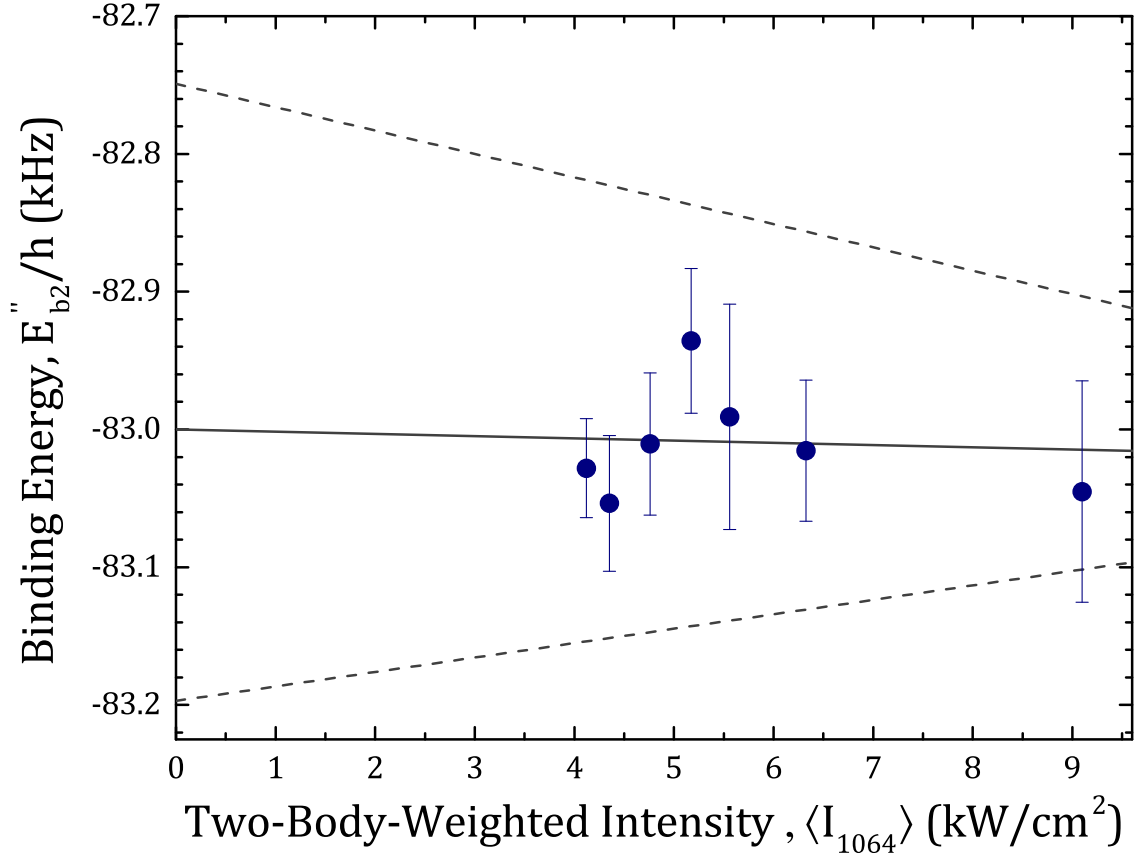


Figure 4.10 : Measurement of halo state susceptibility, χ_{1064}

Measured resonance positions corrected for excitation-laser AC Stark shift and collisional frequency shift, $E'_{b2} - \chi_{689}I_{689} - \chi_n\langle n \rangle$, as a function of average trap laser intensity $\langle I_{1064} \rangle$ for the data such as in Fig. 4.3 . The trend line and confidence intervals are described in the text.

are shifted by the sum of these systematic uncertainties. The resulting value for the unperturbed binding energy is $E_{b2}/h = -83.00(7)(20)$ kHz, where the first uncertainty is statistical, and the second is systematic. We observe a susceptibility to I_{1064} of $\chi_{1064} = 0 \pm 10$ Hz/(kW/cm²).

For two-photon spectroscopy to a weakly bound dimer, it is typical to neglect any potential AC Stark shift due to far-off-resonant trapping lasers because the atoms contribute to the overall polarizability approximately as free atoms. But the high precision of our measurement allows us to detect a small shift. This corresponds to a relative differential polarizability of $\chi_{1064}/2\chi_{1064,g}g = (\chi_{1064,b2} - 2\chi_{1064,g}g/2\chi_{1064,g}g \approx xx$.

4.5 Unperturbed halo binding energy

In the limit of extremely small binding energy, and thus resonant atom-atom interactions, the binding energy of a halo molecule is approximately given by [30]

$$E_b = -\hbar^2/2\mu a^2. \quad (4.13)$$

For interactions described at long-range by the van-der-Waals form, $V(r) = -C_6/r^6$, as with ultracold atoms, a convenient figure of merit for quantifying how accurate this simple expression should be is given by the ratio of the s -wave scattering length to the mean scattering length or interaction range, closely related to the van der Waals length through [42, 37]

$$\bar{a} = l_{\text{vdW}} \frac{\Gamma\left(\frac{3}{4}\right)}{\sqrt{2}\Gamma\left(\frac{5}{4}\right)}. \quad (4.14)$$

Slightly away from resonance, corrections to the binding energy for the van

der Waals potential were worked out in [43, 44], yielding

$$E_{b2} = -\frac{\hbar^2}{2\mu(a-\bar{a})^2} \left[1 + \frac{g_1\bar{a}}{a-\bar{a}} + \frac{g_2\bar{a}^2}{(a-\bar{a})^2} + \dots \right], \quad (4.15)$$

where $g_1 = \Gamma(1/4)^4/6\pi^2 - 2 = 0.918\dots$ and $g_2 = (5/4)g_1^2 - 2 = -0.947\dots$. The range of validity of this expression is $a \gtrsim 2\bar{a}$. The accuracy of the first term in this expansion has been experimentally confirmed for various systems such as ^{85}Rb [39, 52], ^{40}K [53, 54] and ^6Li [55]. This derivation of Eq. (4.15) assumes that the influence of short-range physics, which can be expressed through a quantum defect, varies negligibly from threshold to the molecular binding energy. We expect this to be an excellent approximation, since, as shown in Ref. [43] the corrections are typically less than about 1% even for GHz binding energies.

For ground-state ^{86}Sr atoms, $\bar{a} = 71.3 a_0$. The most accurate value available for the s-wave scattering length is $a = 798(12) a_0$ [45], satisfying the requirement of $a \gg \bar{a}$ for the least-bound state on the ground molecular potential to be a halo molecule. Nonetheless, $\bar{a}/(a-\bar{a}) = .10$, and the corrections given by Eq. (4.15) are significant. Figure 4.5 shows the importance of the correction terms.

Equation (4.15) and the previous best value of the scattering length [45] predict a binding energy of $E_{b2} = -86(3) \text{ kHz}$. This agrees with our measurement, but by inverting Eq. (4.15), we can use our increased accuracy in E_{b2} to extract an improved value of the scattering length of $a = 810.6(3)(9) a_0$, where uncertainties reflect statistical and systematic uncertainties in E_{b2} respectively. The next higher-order term in $x_0 = \bar{a}/(a-\bar{a})$ is likely to introduce a correction on the order of 100 Hz in Eq. (4.15), creating a systematic uncertainty in a that is about one third of the uncertainty from our measurement.

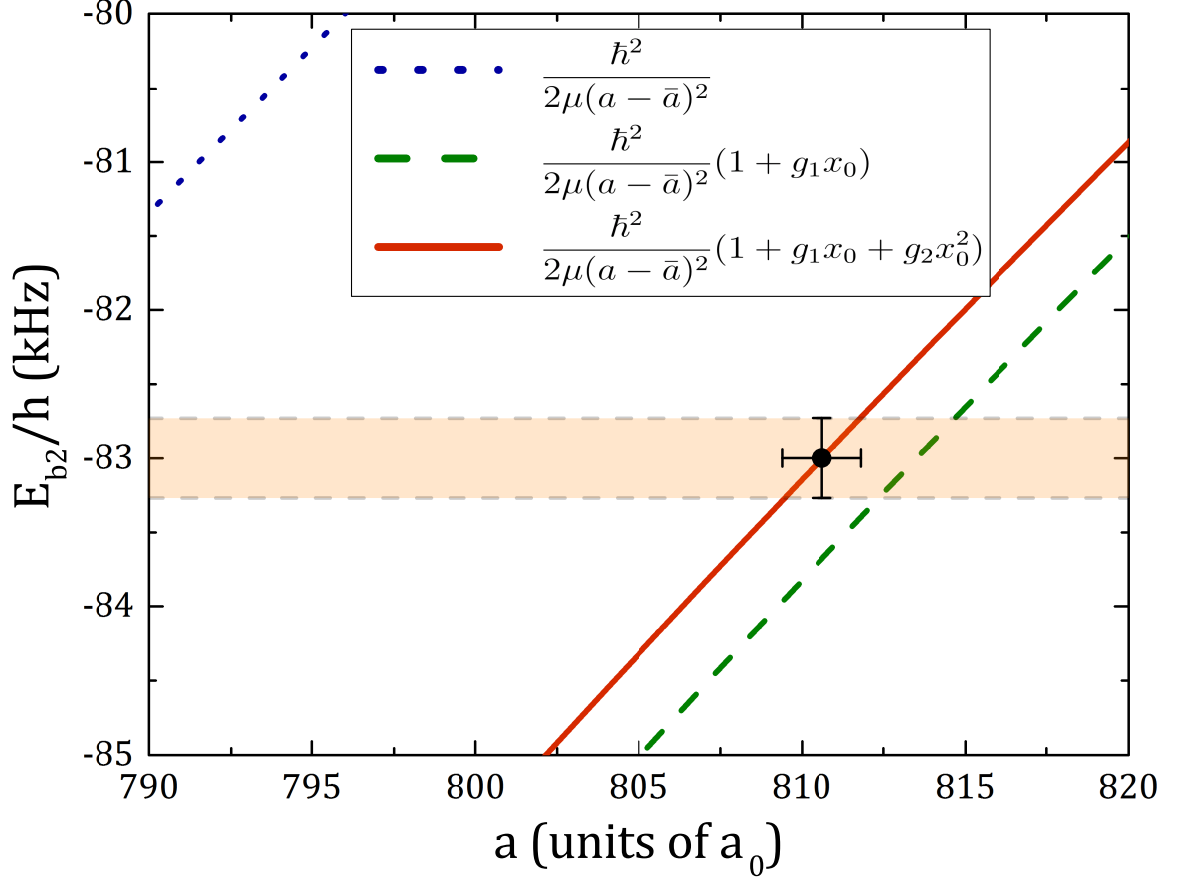


Figure 4.11 : Determination of ^{86}Sr scattering length

Halo binding energy versus s -wave atom-atom scattering length for ^{86}Sr . The shaded region indicates our experimental measurement. The lines are predictions of Eq. 4.15 retaining up to the first, second, and third terms as indicated in the legend [$x_0 = \bar{a}/(a - \bar{a})$]. The data point is the prediction of Eq. (4.15) for the recommended value of the measured binding energy.

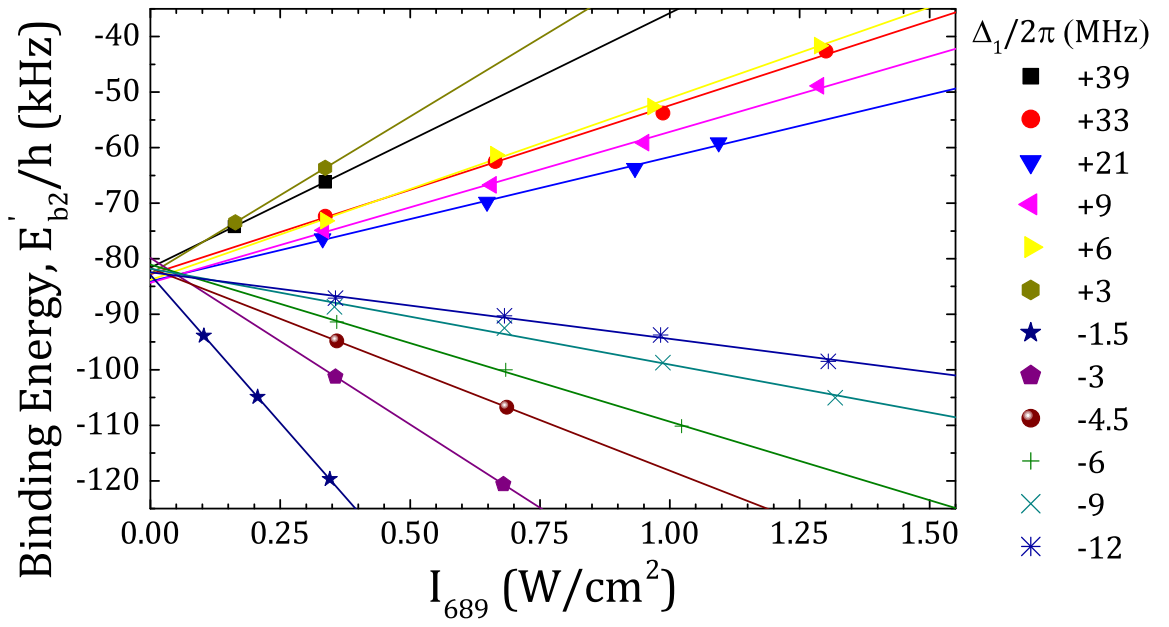


Figure 4.12 : Variation of halo susceptibility as a function of Δ_1

Two-photon PA resonance positions as a function of twice the single-beam excitation intensity, $2I = I_{689}$ for various intermediate state detunings, Δ_1 .

4.6 Calculating the bound-bound Frank-Condon factor

The proximity of ^{86}Sr to a scattering resonance and the susceptibility of the halo binding energy to the intensity of the excitation light suggests using light to tune the binding energy and scattering length as was done with optically assisted magnetic Feshbach resonances [56, 38], which is closely related to the use of optical Feshbach resonances [25, 57, 23, 22]. Understanding the frequency-dependence of χ_{689} is important for investigating this possibility, so we extracted this parameter from spectra at a wide range of 689-nm laser intensities and detuning from the intermediate resonance (Δ_1).

Figure 4.5 shows the resulting resonance positions, E'_{b2} , versus twice the single-beam intensity, $2I = I_{689}$. The shift in molecular binding energy is linear with intensity over the explored range, but varies greatly in magnitude and sign. From linear fits, we extract the AC Stark shift parameter $\chi_{689}(\Delta_1)$ through $E'_{b2} \equiv E_{b2} + h\chi_{689}(\Delta_1)I_{689}$ (Fig. 4.6).

In the experiment, the total 689-nm intensity oscillates with 100% contrast according to $I_{\text{total}} = I_1 + I_2 + 2\sqrt{I_1 I_2} \cos[(\omega_1 - \omega_2)t] = 2I \{1 + \cos[(\omega_1 - \omega_2)t]\}$. The functional form we use to fit the AC Stark shift reflects the time average of the intensity and neglects the interference term. To confirm that this is the correct description, we numerically solved the time-evolution for a three-level system with similar optical couplings and oscillating optical intensity as present during two-photon

PA of a halo state. The Hamiltonian is

$$H = \begin{pmatrix} 0 & \Omega_{01} [\cos(\omega_1 t) + \cos(\omega_2 t)] & 0 \\ \Omega_{01} [\cos(\omega_1 t) + \cos(\omega_2 t)] & E_{b1} & \Omega_{12} [\cos(\omega_1 t) + \cos(\omega_2 t)] \\ 0 & \Omega_{12} [\cos(\omega_1 t) + \cos(\omega_2 t)] & E_{b2} \end{pmatrix}$$

For $\Omega_{01} \ll \Omega_{12} \ll |\Delta_1| \equiv |\omega_1 - E_{b1}/\hbar|$, which is analogous to the experimental conditions used here, we find that the two-photon resonance is shifted by

$$\frac{\hbar\Omega_{12}^2}{4\Delta_1} + \frac{\hbar\Omega_{12}^2}{4(\Delta_1 - E_{b2}/\hbar)} \approx \frac{\hbar\Omega_{12}^2}{2\Delta_1}. \quad (4.16)$$

This agrees with our observation of a shift that is linear with intensity, and implies that the susceptibility is related to the Rabi frequency for a single-beam intensity I through $\chi_{689} \approx (\Omega_{12}/\sqrt{I})^2/(8\pi\Delta_1)$.

This single-resonance model [Eq. (4.16)] describes the observed shifts well for detuning close to the $\nu = -2$ state of the 0_u^+ molecular potential (small Δ_1). For large positive Δ_1 , however, at which ω_1 and ω_2 approach atomic resonance, deviations indicate coupling to one or more other states (Fig. 4.6). The most likely suspects are the $\nu = -1$, $J = 1$ excited molecular state, bound by 1.633(1) MHz, and the $^1S_0 + ^3P_1$ continuum. The sign of the deviation indicates that AC Stark shift of colliding 1S_0 atoms due to coupling to the 3P_1 state is dominant in this regime. We have neglected shifts due to collisions and the trapping laser, which are small at the large excitation-laser intensities used here.

A fit of the single-resonance model as shown in Fig. 4.6 yields $\Omega_{2,12}/2\pi \equiv \Omega_{12}/2\pi = 800 \text{ kHz}$ for $I = 1 \text{ W/cm}^2$. Note that $\Omega_{2,12}$ as defined here would be the splitting of the Autler-Townes doublet [36], which differs from the Bohn-Julienne

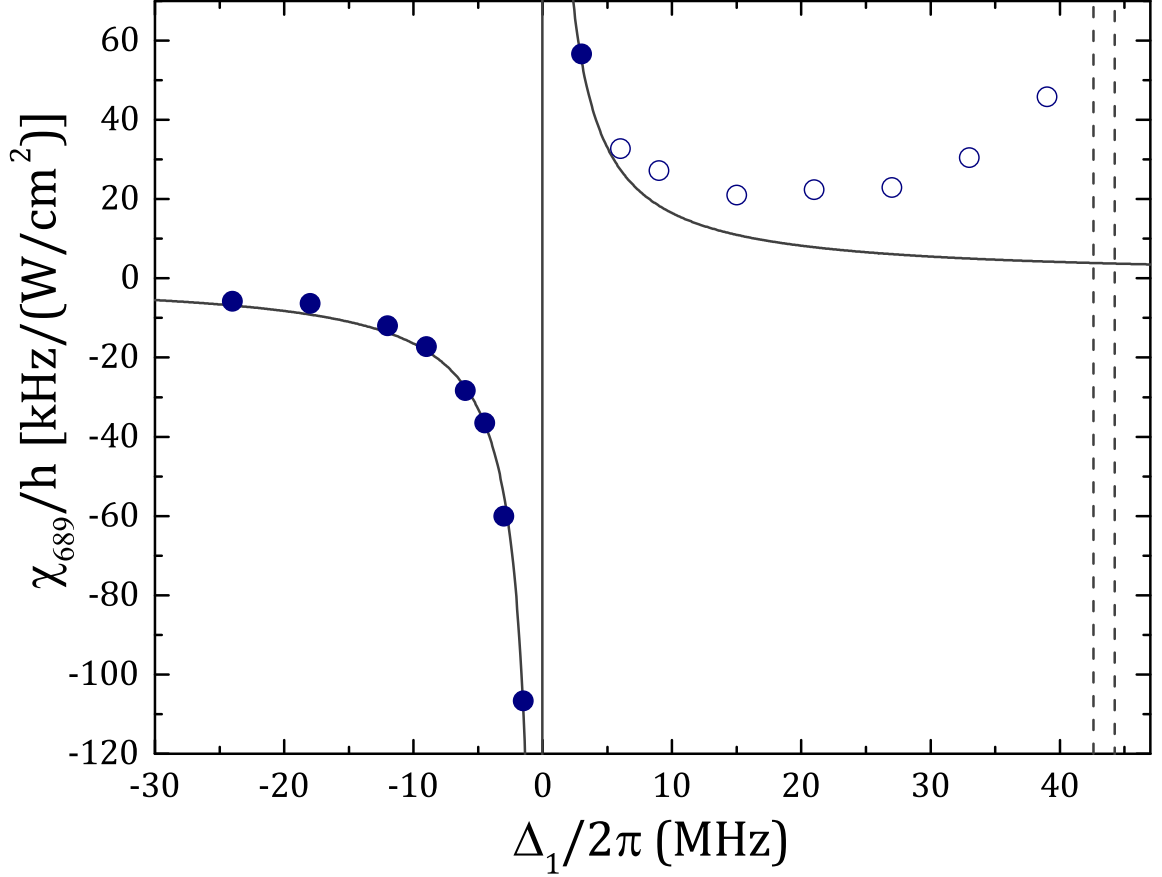


Figure 4.13 : Estimate of bound-bound coupling via isolated resonance model
AC Stark shift susceptibility, χ_{689} . Dashed lines indicate the positions of the $\nu = -1$, $J = 1$ excited molecular state, bound by 1.633(1) MHz, and the $^1S_0 + ^3P_1$ continuum. Solid and open symbols show experimental measurements of the susceptibility. Using only the solid symbols, we fit a single resonance model of the form $\chi_{689} \approx (\Omega_{12}/\sqrt{I})^2/(8\pi\Delta_1)$ and show this fit result as a solid line.

definition of the molecular Rabi coupling [?]. From the measured $\Omega_{2,12}$, one can extract the Franck-Condon factor, f_{FCF} , reflecting the overlap of the ground and intermediate molecular states through

$$\Omega_{2,12} = \sqrt{f_{\text{ROT}}} \sqrt{f_{\text{FCF}}} \gamma_{\text{atomic}} \sqrt{\frac{I}{2I_{\text{sat,atom}}}} \quad (4.17)$$

where $I_{\text{sat,atom}} = 2\pi^2 \hbar c \gamma_{\text{atomic}} / (3\lambda^3) = 3 \mu\text{W}/\text{cm}^2$ is the atomic saturation intensity for the 1S_0 - 3P_1 transition and $I = I_{689}/2$ is the single-beam intensity. The rotational factor f_{ROT} accounts for the change in dipole moment from atom to molecule due to symmetry of the wave function and projection on a rotating molecular axis. Following the formalism described in [36], $f_{\text{ROT}} = 2$ for the $J = 1 \rightarrow 0$ bound-bound molecular transition studied here. This yields $f_{\text{FCF}} = 0.03$.

From the formula for the line shape we can see that it depends on the spatial distribution of the atoms. The standard approximation made when measuring these types of systems is to ensure loss does not cause heating of the atoms during photoassociation. Heating results in re-equilibration of the atomic density distribution, which in turn effects the rate of loss creation. Without independent controls to keep the system in thermal (and therefore spatial density) equilibrium.

What are the things the rate equation deals with?

We need the density distribution.

In a harmonic trap, there is a simple analytic form to the density distribution of a thermal gas. From Mi's work (and others) we know that this is only an approximation that is valid when η is approx greater than 4. When greater than 4 we can apply the high- η approx and the trap frequencies along a particular direction

reduce to $j_{eq}i$.

However, the trap we did this experiment in were at η 's of 1 or less so we don't have an analytic solution to the spatial distribution. Since this could be a problem we need to know what the trap looks like.

We measure trap oscillation freq. at several different powers and model the trap using the utility outlined somewhere else.

From the numeric model, we can define a spatially dependent η which is determined by the local trap depth which is simply the difference between the local potential energy and the global depth. This is illustrated in fig something.

The spatial information is not only important for the density determination, but also for the range of available thermal energies. Consider two atoms near the local bottom of the trap. By definition, in equilibrium, a single atom may only have up to the trap depths worth of energy since any additional energy would result in its expulsion from the trap. In this case, in a relative momentum frame, the allowed collision energies range from zero to two times the trap depth. Similarly, as we move towards the edge of the trap the range of accessible collision energies shrinks. This additional weighting factor may be viewed as having a local truncated Boltzmann distribution at every point in space.

Normally the BZ dist goes to infinity but here we have a cutoff at 2 trap depth. The most naive approx would be to simply consider the BZ and harshly truncate at 2 trap depth. We tried this

We know this is unphysical since we should expect that the probability of ob-

serving a certain momenta at a certain point in space, should smoothly tend zero towards as we approach the edge of the trap. To see what this looks like we (and determine how important the effect is) we rederive the relative momentum distribution.

Some stuff about center of mass and relative

What were all the cases and conclusions of having done this? Remember to consider what the different cases are. If the total relative energy can be X then how does that get split up? Use the plots to show this limiting behavior. Like if particle 1 has all the energy then there is only one possible value for particle 2 (and vice versa).

DERIVATION for truncated trap below

Need to lookup references for this molecular chaos assumption. What about ergodicity? How to discuss that we may not be completely ergodic?

What does my potential look like? Can I make it a piecewise function? How should I introduce this part?

Where does the f equation come from? I believe this is just the normalized boltzmann factor for probability to occupy a particular state.

We can truncate this single particle distribution by

$$f_{\mathbf{r}}(\mathbf{p}) = A \left(\frac{1}{2\pi k_B T} \right)^{3/2} e^{\left(\frac{-p^2}{2mk_B T} \right)} \Theta \left(\epsilon_{max} - U(\mathbf{r}) - \frac{p^2}{2m} \right) \quad (4.18)$$

where A is a normalization constant which ensures $\int_0^\infty f_{\mathbf{r}}(\mathbf{p}) d\mathbf{p} = 1$ and $\Theta(x)$ is the Heaviside function defined by

$$\Theta(x) = \begin{cases} 1 & \text{if } x \geq 0, \\ 0 & \text{if } x < 0 \end{cases} \quad (4.19)$$

We got a certain answer with the way shown in the paper.

We can also use a completely different method that ignores all the considerations of the last few sections. As was done in the calcium paper, we could simply fit the blue edge of the feature using a model function which can capture the high level features of the lineshape. Get the same answer. SHOW PLOTS TO THIS AFFECT AND COMPARE

Maybe go a little into the isolated resonance model (or at least recall), then tie into how we can measure the susceptibility across several different detunings which can give us the coupling to intermediate level. The first order analysis of this data suggest a bound-bound rabi frequency of **BLAH**.

Point out the curling up at the end and say how the simple isolated resonance model cannot predict. A full coupled channel calculation probably could but in the spirit of the Bohn and Julienne semi-classical approach, we set out to derive an approximate analytic expression to determine the binding energies. This is presented in the next chapter.

Lastly, we note that in the context of photoassociation, the center-of-mass component of Eq.A.3 is not typically considered as typical PAS experiments are performed utilizing broad dipole allowed transitions which have linewidths much greater than the doppler width thus only the relative momentum between particles is important

for determining the loss rate coefficient K discussed in (somewhere).

The case of PA using narrow intercombination line transitions found in alkaline-earth-metal atoms

In general K is considered as a boltzmann average over a single loss rate constant This can be seen in [27] Eq. 1 where the loss rate constant is given by

$$\begin{aligned} K(\Delta, T) &= \langle \mathcal{K}(\Delta, \mathbf{P}_c, \mathbf{p}_r) \rangle \\ &= \int d^3\mathbf{P}_c f_M(\mathbf{P}_c) \int d^3\mathbf{p}_r f_\mu(\mathbf{p}_r) \mathcal{K}(\Delta, \mathbf{P}_c, \mathbf{p}_r) \end{aligned} \quad (4.20)$$

To this end we can integrate out the center of mass component to obtain the distribution most typically relevant to photoassociation.

By the time I've gotten to this I have already introduced K and that is not what I wanted to do.

conclusion here is the modified version of K we need for a trap that has a truncated energy distribution

to get there normal version of K is given in ch3 this K can be given in terms of f ? this version of f is given in the appendix why do I integrate out the com component?

typical PAS experiments utilize dipole allowed transitions which have linewidths many times larger than the

We now perform a change of variables using Eq. and Eq.A.2 can be rewritten as

Need to make a connection between dipole matrix element, wigner threshold, and infinite square step potential. This infinite square step can be viewed as a dilute ideal gas.

To prove this assumption I want to show that using the square step I can get the same equations like in Eq. 1 of the 99 paper. Then once we know the infinite energy behavior (valid for only a particular portion of energy due to s-wave constraint) then we can ask what happens if $f(p)$ is truncated.

In the s-wave limit I need to write K as a function of $f(p)$ (should do this in the appendix proof and reference in body). Given the form of the loss rate constant K , our problem reduces to determining the form of $f(p)$ when η is finite.

Ok, so need to reference [27] to motivate usage of center of mass. Then use [21] Eq. 43 to reference the particular form

what is the throughline I want to make? Develop $K_{in} \rightarrow$ recast in terms of P distribution \rightarrow show how we can replace the normal dist with a truncated dist \rightarrow explore the effects of that truncation

Chapter 5

Strongly coupled PAS of a weakly bound molecule

5.1 Introduction

”Lorem ipsum dolor sit amet, consectetur adipiscing elit, sed do eiusmod tempor incididunt ut labore et dolore magna aliqua. Ut enim ad minim veniam, quis nostrud exercitation ullamco laboris nisi ut aliquip ex ea commodo consequat. Duis aute irure dolor in reprehenderit in voluptate velit esse cillum dolore eu fugiat nulla pariatur. Excepteur sint occaecat cupidatat non proident, sunt in culpa qui officia deserunt mollit anim id est laborum.”

5.2 Experimental methods

”Lorem ipsum dolor sit amet, consectetur adipiscing elit, sed do eiusmod tempor incididunt ut labore et dolore magna aliqua. Ut enim ad minim veniam, quis nostrud exercitation ullamco laboris nisi ut aliquip ex ea commodo consequat. Duis aute irure dolor in reprehenderit in voluptate velit esse cillum dolore eu fugiat nulla pariatur. Excepteur sint occaecat cupidatat non proident, sunt in culpa qui officia deserunt mollit anim id est laborum.”

5.3 Three level model

”Lorem ipsum dolor sit amet, consectetur adipiscing elit, sed do eiusmod tempor incididunt ut labore et dolore magna aliqua. Ut enim ad minim veniam, quis nostrud exercitation ullamco laboris nisi ut aliquip ex ea commodo consequat. Duis aute irure dolor in reprehenderit in voluptate velit esse cillum dolore eu fugiat nulla pariatur. Excepteur sint occaecat cupidatat non proident, sunt in culpa qui officia deserunt mollit anim id est laborum.”

5.4 Resonance positions

”Lorem ipsum dolor sit amet, consectetur adipiscing elit, sed do eiusmod tempor incididunt ut labore et dolore magna aliqua. Ut enim ad minim veniam, quis nostrud exercitation ullamco laboris nisi ut aliquip ex ea commodo consequat. Duis aute irure dolor in reprehenderit in voluptate velit esse cillum dolore eu fugiat nulla pariatur. Excepteur sint occaecat cupidatat non proident, sunt in culpa qui officia deserunt mollit anim id est laborum.”

5.5 Lineshape

”Lorem ipsum dolor sit amet, consectetur adipiscing elit, sed do eiusmod tempor incididunt ut labore et dolore magna aliqua. Ut enim ad minim veniam, quis nostrud exercitation ullamco laboris nisi ut aliquip ex ea commodo consequat. Duis aute irure dolor in reprehenderit in voluptate velit esse cillum dolore eu fugiat nulla pariatur. Excepteur sint occaecat cupidatat non proident, sunt in culpa qui officia deserunt mollit anim id est laborum.”

5.6 Emergence of multi-photon Raman coupling

”Lorem ipsum dolor sit amet, consectetur adipiscing elit, sed do eiusmod tempor incididunt ut labore et dolore magna aliqua. Ut enim ad minim veniam, quis nostrud exercitation ullamco laboris nisi ut aliquip ex ea commodo consequat. Duis aute irure dolor in reprehenderit in voluptate velit esse cillum dolore eu fugiat nulla pariatur. Excepteur sint occaecat cupidatat non proident, sunt in culpa qui officia deserunt mollit anim id est laborum.”

Chapter 6

Progress towards studies of quantum magnetism

A straightforward extension of the work presented in this thesis would be to control interparticle spacing via an optical lattice. For these and additional experiments using quantum degenerate fermionic strontium we purchased and installed an optical lattice system. Our lattice is implemented using a Coherent Verdi V-18 which is shapped and propagated to our science chamber in free space. Fig shows the optical path for each arm of our cubic lattice.

Unfortunately, complications due to heating when loading the lattice has limited our success in this optical trap. I want to go over what we have been able to do so far with the lattice.

How did we characterize? Kaptiza-dirac extension

What convinced us we were having problems?

What are some ideas we could do in the lattice? Zeno faster cooling via stimulated raman potentially? (can I model this somehow?) repulzively bound molecules? use interaction control in lattice with the zeno thing

6.1 532 nm optical lattice: installation and characterization

Optical lattices are formed by a standing wave of light which creates a defect free periodic potential. These traps are extremely versatile and have enabled the observation of the superfluid - Mott insulator transition [58], artificial gauge fields for neutral atoms [59], quantum microscopy with single-site resolution [?], and investigations of quantum magnetism [? ?]. They are among the most well-established techniques for controlling a quantum state and have proven to be great tools for exploring the connection between few- and many-body systems [?].

6.1.1 Background

This section should cover band structure and refer to the types of wavefunctions that are possible. Perhaps through some stuff in here from the quantum magnetism proposal from the NSF

Until recently, experiments on the Neutral apparatus were confined to work with bulk gases in an optical dipole trap. While optical dipole traps are useful for efficient evaporation and thermalization of an ultracold gas, experiments with Feshbach molecules in ODTs suffer from a high rate of inelastic collisions. [5]. The association of these molecules in an optical lattice has been shown to slow these processes since atoms must tunnel from site to site and can be pinned in sufficiently deep potentials [60?]. In order to gain a quantitative understanding of these processes we will briefly outline the relevant lattice physics for ultracold bosons in an optical lattice.

An optical lattice is created by counterpropagating two laser beams to form a standing wave pattern, which for two plane waves in one dimension results in a

periodic potential given by

$$V(x) = V_{lat} \sin^2(k_L x) \quad (6.1)$$

where V_{lat} is the lattice depth determined by the polarizability of the atom for a given trapping wavelength λ and laser intensity I , and k_L is the lattice wavevector. This potential can be readily extended to three dimensions using two additional pairs of counterpropagating laser beams along the y and z directions which results in a 3D cubic lattice. Depth of the trapping potential, V_{lat} , is controlled by varying the intensity of the lattice beams. Clever arrangements of laser beam propagation, in addition to phase and polarization control of the trapping fields, can extend these standing wave potentials to a number of non-trivial geometries such as triangular, checkerboard, and dimerized lattices [61].

Periodic potentials are powerful because they break the translational invariance of space which results in the formation of band structure and the opening of bandgaps or disallowed particle energies [62]. Because of the broken invariance, p is no longer a good quantum number and instead must be replaced by two new quantum numbers: the band index, n , and the quasimomentum, q . In one dimension, quasimomentum is specified by $q = p - nG$, where $G = 2\pi/a$ is a reciprocal lattice vector, and a is the real space lattice constant. Fig. 6.1.1 shows how the band structure varies as the lattice depth is increased. Optical lattices have a lattice spacing $a = \lambda/2$ which determines the reciprocal lattice vector $G = 4\pi/\lambda = 2\hbar k_L$ and the natural energy scale $E_r = \frac{\hbar^2 k_L^2}{2m}$ where m is the atomic mass and k_L is the lattice wavevector, $k_L = 2\pi/\lambda$. From the band structure, we see that the bandwidth of each band, given by $\Delta E = E_{q=\hbar k_L} - E_{q=0}$, decreases as the lattice depth is increased. In the limit

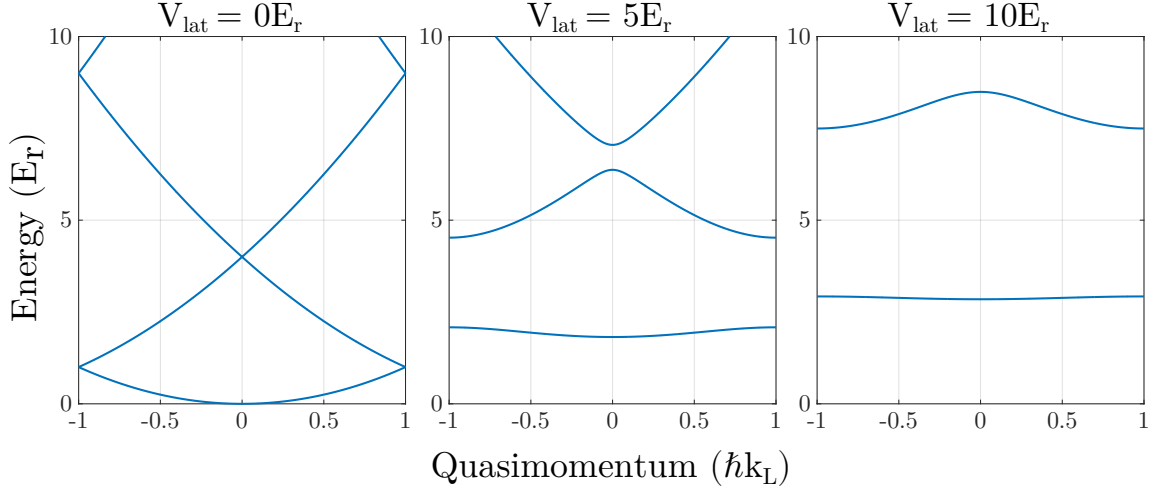


Figure 6.1 : 1D band structure as a function of lattice depth

One dimensional band structure for an optical lattice as the lattice depth is increased. The band energies are found by solving the Schrödinger equation using the Bloch functions of Eq. 6.2.

that $V_{lat} \rightarrow \infty$ the band structure reduces to a ladder of harmonic oscillator levels spaced by $\hbar\omega_{ho} = \sqrt{4V_{lat}E_r}$. Although, for moderately deep lattices, $V_{lat} \gtrsim 5E_r$, this approximation is valid near the center of the Brillouin zone, $q = 0$, and provides a simple form to estimate the energy gaps between bands [? 63].

Solutions to the Schrödinger equation in a periodic potential are given by the Bloch functions [62]

$$\phi_q^{(n)}(x) = e^{iqx/\hbar} u_q^{(n)}(x) \quad (6.2)$$

These eigenstate wavefunctions are specified for a given quasimomentum q , and band index n . Their corresponding energy eigenvalues define the band structure of the lattice shown in Fig. 6.1.1. From Eq. 6.2 we see that the Bloch functions are the

product of plane waves modulated by a function $u_q^{(n)}(x)$, which shares the periodicity of the underlying lattice potential [62]. For an optical lattice this modulating function can be expanded in a basis of plane waves through a Fourier decomposition of the lattice potential in Eq. 6.1, which gives [61],

$$u_q^{(n)}(x) = \sum_l c_l^{(n,q)} e^{i2lk_L x} \quad (6.3)$$

Here $c_l^{(n,q)}$ are the coefficients for each plane wave in the basis expansion that are found by diagonalizing the lattice Hamiltonian [61].

Often, we are interested in the dynamics of particles on a particular lattice site, but since Bloch functions are delocalized over the entire lattice, it is useful to instead use the Wannier functions. These functions provide an orthogonal and normalized set of wavefunctions that are maximally localized to a specific lattice site. The Wannier function for a localized particle in the n^{th} band of a lattice site located at position x_i is given by [63]

$$w_n(x - x_i) = \mathcal{N}^{-1/2} \sum_q e^{iqx_i/\hbar} \phi_q^{(n)}(x) \quad (6.4)$$

where \mathcal{N} is a normalization constant and $\phi_q^{(n)}(x)$ are the Bloch functions of Eq. 6.2. This localized description of particles allows us to calculate important physical quantities which govern dynamical properties of the lattice such as the tunneling rate, J/\hbar , and on-site interaction energy, U . As $V_{lat} \rightarrow \infty$, the Wannier functions approach the eigenfunctions of the harmonic oscillator, which allows us to estimate the spatial extent of an atomic wavefunction by $a_{ho} = \sqrt{\frac{\hbar}{m\omega_{ho}}}$ [63].

When bosons are confined to the lowest energy band of a lattice, a particularly simple model known as the Bose-Hubbard Hamiltonian is used to describe the lattice

system [?].

$$H_{BH} = -J \sum_{\langle i,j \rangle} (\hat{b}_i^\dagger \hat{b}_j + \hat{b}_j^\dagger \hat{b}_i) + \frac{U}{2} \sum_i \hat{n}_i(\hat{n}_i - 1) \quad (6.5)$$

Where $\langle i, j \rangle$ denotes a sum over nearest-neighbors. This model is the simplest example of a non-trivial interacting many-body system for dynamics in a lattice. The first term describes hopping of bosons from site to site at a rate J/\hbar . The second term describes an interaction energy which is related to the s-wave contact interaction term, $g = 4\pi\hbar^2 a_s/m$, where a_s , is the s-wave scattering length of the particles. J and U can be calculated directly using the Wannier functions of Eq. 6.4 and are given by [63]

$$\begin{aligned} J_{ij} &= - \int d^3x w_0(x - x_i) \left(\frac{p^2}{2m} + V(x) \right) w_0(x - x_j) \\ U &= \frac{4\pi\hbar^2 a_s}{m} \int d^3x |w_0(x - x_i)|^4 \end{aligned} \quad (6.6)$$

Using Eq. 6.6 we have calculated the expected tunneling rates and interaction energies for atomic strontium and plot the results in Fig. 6.1.1 for homonuclear samples of strontium as a function of lattice depth. This single band calculation is valid under the assumption that the interaction energy of a site is smaller than the bandgap between the $n = 0$ and 1 bands, namely $UN \lesssim \hbar\omega_{ho}$ where N is the mean number of particles per site and $\hbar\omega_{ho}$ is the approximate energy spacing between bands [64].

Alternatively, Eq. 6.6 can be simplified through considering appropriate limits to the Bose-Hubbard model. In the limit that $U \rightarrow 0$, the Bose-Hubbard model becomes exactly solvable and the energy of the $n = 0$ band is given by $E_q^{(0)} = -2J \cos(qa)$ [63]. Thus, the tunneling rate, J , can be related to the bandwidth of the lowest band as expressed in Eq. 6.7. Under a separate limit, $V_{lat} \rightarrow \infty$, then the tunneling rate goes to zero and the localized wavefunctions can be approximated by

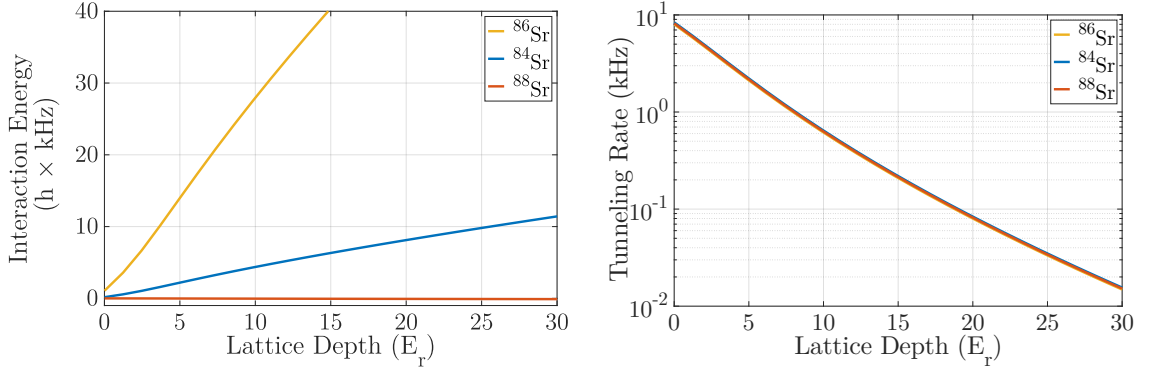


Figure 6.2 : Calculated interaction energies and tunneling rates for each isotope of strontium

The interaction energy shows a large variation because of its dependence on the s-wave scattering length. However, the tunneling rate is approximately the same for all isotopes since the change in mass is negligible between isotopes.

a Gaussian wavefunction which yields the form for the on-site interaction U given in Eq. 6.7 [64].

$$J = \frac{E_{q=\hbar k_L} - E_{q=0}}{4} \quad (6.7)$$

$$U = \frac{\hbar a_s}{\sqrt{2\pi}} \frac{\bar{\omega}_{ho}}{\bar{a}_{ho}}$$

Here \bar{a}_{ho} and $\bar{\omega}_{ho}$ are the geometric means of the one-dimensional harmonic oscillator length and frequency given previously.

Competition between J and U results in a phase transition known as the superfluid - Mott insulator transition [65, 58]. When $J/U \gg 1$ atoms are free to delocalize over the lattice and the many-body ground state is a superfluid. In the opposite limit that $J/U \ll 1$, particle fluctuations between sites are no longer energetically accessible and the system transitions into an interaction induced insulating state known as a Mott insulator. This state is characterized by fixed particle number per site and in

a 3D cubic lattice near unit filling, this phase transition occurs at $J/U \approx 35$ which, for ^{84}Sr , corresponds to a lattice depth of $V_{lat} \approx 13E_r$ [65].

The tunability of an optical lattice potential is useful for studying feshbach molecules. By controlling the lattice depth and/or atomic density, we can efficiently create molecules when there are two or more atoms per site. Using the volume of a unit cell we can estimate the densities needed to reach average on-site occupancy of 2, which is ideal for forming isolated molecules. For a lattice wavelength of 532 nm in a simple cubic configuration, the volume for each lattice site is $1.9 \times 10^{-14} \text{ cm}^3$, so we must achieve densities on the order of $4 \times 10^{14} \text{ cm}^{-3}$ to expect significant conversion. A more detailed approach to estimate our conversion efficiency would entail: 1) calculating the variation in chemical potential across the trap due to the inhomogeneous confinement of the trapping potential, 2) finding the average particle number per site as a function of J/U to estimate the distribution of μ/U on the superfluid - Mott insulating phase diagram [65], and 3) integrating the density distribution from the center of the trap to a limiting value of μ/U , where the local density is too dilute for efficient molecule conversion. Though such a calculation is beyond the scope of this proposal, it is worth noting that the shell structure found near the Mott insulating regime inhibits complete molecular conversion of the atomic gas. Therefore, molecules are accompanied by a large number of unconverted remnant atoms. Previous investigators have shown that it is beneficial to clear non-molecule atoms out of the lattice through a sequence of light and/or microwave pulses. Such a cleaning sequence will need to be investigated in our system since tunneling from single atoms can lead to a reduction of the molecular lifetime [5, 60].

6.1.2 Setup

This section should cover all the specifics regarding the lattice

Our optical lattice operates at $\lambda = 532 \text{ nm}$ and is derived from a Coherent Verdi V-18 single mode laser which is sent through separate AOMs for intensity control of each arm before propagating in free space to the atoms. The horizontal arms of the lattice (x and y) have $1/e^2$ waists of $200 \mu\text{m} \times 200 \mu\text{m}$ and their polarization is linear and aligned along the z direction, parallel to gravity. The vertically propagating beam has a $1/e^2$ waist size of $300 \mu\text{m} \times 300 \mu\text{m}$ and polarization aligned orthogonal to the polarization of the horizontal beams. With this configuration we have measured a maximum depth of $9E_r$ in an isotropic lattice. As this is our first implementation of an optical lattice, we have spent a significant amount of time characterizing our system as detailed below.

6.1.3 Measurement and results

What are all the types of experiments we did in the lattice?

Cover sideband cooling and Bloch oscillations Results, look into why its not necessarily so easy from end of red MOT, thoughts on how it could become useful

Kapitza-Dirac Scattering

Brief intro to theory and some plots showing fits.

Fig. 6.1.3 shows a typical Kapitza-Dirac oscillation pattern which we use to maximize beam overlap near the atoms and calibrate our achievable lattice depths. Kapitza-Dirac is useful as an alignment tool since measurement of the population

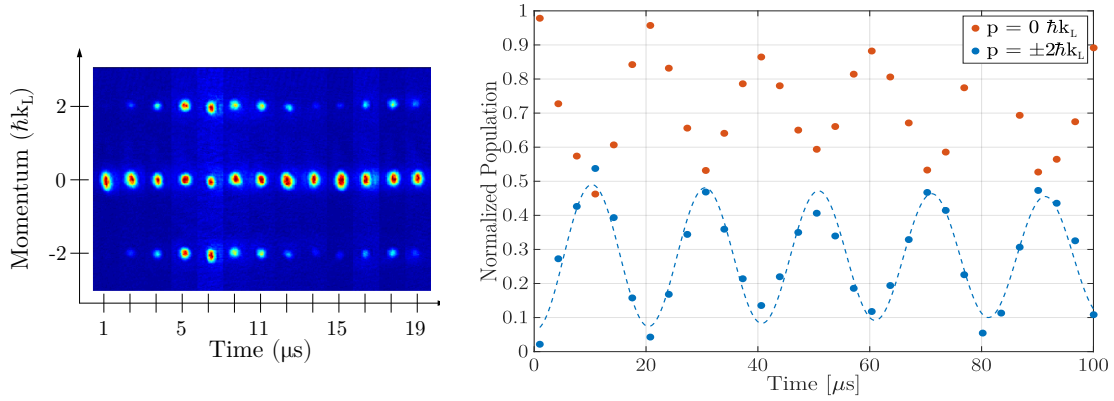


Figure 6.3 : Evolution of plane wave population using Kapitza-Dirac

Left: Time of flight slices for several realizations of Kapitza-Dirac with varying hold time in the lattice. Right: Normalized population from fits of time-of-flight images. Oscillations are fit with a decaying sinusoidal and the best-fit frequency is used to determine the lattice depth.

oscillation frequency can be highly accurate and directly relates to the bandgap energy in the lattice, shown in Fig. 6.1.1.

Kapitza-Dirac diffraction can be viewed as a diabatic projection from an initial eigenstate to a new set of eigenstates which results in an oscillation of the wavefunctions probability amplitudes over the new eigenstates of the system [66]. As was discussed in Sec. 6.1, the free space eigenstates are not the eigenstates of the lattice Hamiltonian. Thus a pure $p = 0$ plane wave, $|\phi_{p=0}\rangle$, suddenly loaded into an optical lattice can be written as a superposition of the Bloch states given by Eq. 6.2, here denoted by $|n, q\rangle$.

$$|\Psi(t = 0)\rangle = \sum_{n=0}^{\infty} |n, q\rangle \langle n, q | \phi_{p=0} \rangle \quad (6.8)$$

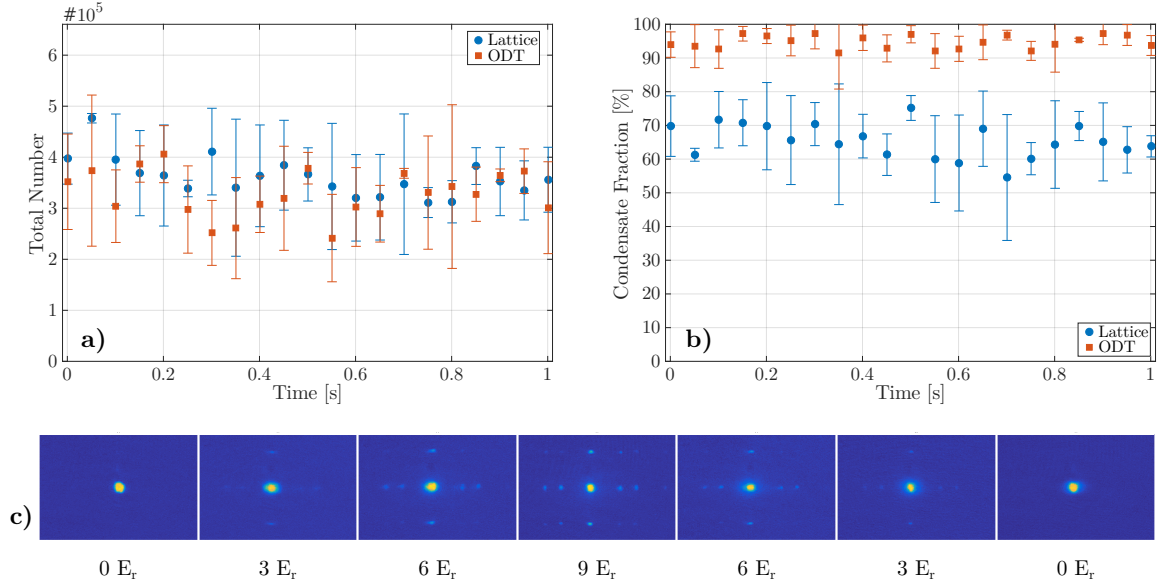


Figure 6.4 : Evolution of condensate fraction over time after adiabatically ramping on the lattice to $9 E_r$. a,b) Comparison of total number and condensate fraction for a sample held in the optical dipole trap (red squares) or in a deep lattice (blue circles). c) Time of flight images after ramping on the lattice and diabatically projecting back to plane wave states.

The time evolution of this state is then given by

$$|\Psi(t)\rangle = \sum_{n=0}^{\infty} |n, q\rangle \langle n, q | \phi_{p=0} \rangle \exp\left(\frac{-i E_n(q) t}{\hbar}\right) \quad (6.9)$$

where $E_n(q)$ is the energy of the Bloch state at a specified q and n shown in Fig. 6.1.1. The exponential factor of Eq. 6.9 introduces oscillations among Bloch states and after a second diabatic projection back to the plane wave basis, we can relate evolution of plane wave population to the bandgap energy. From this analysis we find that for relatively weak lattices, $V_{lat} \lesssim 10 E_r$, the plane wave population will vary as $\omega_{osc} = (E_2 - E_0)/\hbar$. Where E_i is the band energy of the i^{th} band with $q = 0$ as is the case when performing Kapitza-Dirac with a Bose-Einstein condensate.

Heating of a quantum degenerate gas

Creation of a Mott insulator and the results showing unacceptable heating rates

While Kapitza-Dirac diffraction is useful as a characterization tool, we typically wish to maintain equilibrium when loading condensates into the lattice. Thus slowly ramping up the lattice laser intensity will adiabatically transform a plane wave ground state into the ground Bloch state of the lattice [67]. Strictly speaking, in order to adiabatically connect the free space eigenstates and the lattice eigensates, the lattice must be turned on infinitely slowly due to the infinitesimal bandgaps which open near the band edges. Although near the band center, $q = 0$, the adiabaticity requirement relaxes to $dV_{lat}/dt \ll 16E_r^2/\hbar$, [66] which for strontium in a 532 nm lattice is $\approx 5 \mu s/E_r$. However, in practice we find that our condensate fraction is reduced during fast ramps into the lattice. Instead, we exponentially ramp on the lattice over 100 ms which reduces heating caused by the ramp. As shown in Fig. 6.1.3, we observe a large condensate fraction after similarly ramping the lattice back down. Additionally, by holding in a deep lattice after an adiabatic ramp, we can measure the effects of off-resonant scatter of lattice photons as a reduction of atom population over time. For our red detuned optical lattice we expect the off-resonant scattering rate to be well approximated by a simple two level approach. In this model, the effective scattering rate is given by [63]

$$\Gamma_{eff} \approx \frac{\Gamma V_{lat}}{\hbar \delta_{lat}} \quad (6.10)$$

where Γ is linewidth of the dipole transition between the two states, V_{lat} is the lattice depth, and δ_{lat} is the detuning of the optical lattice from the two level transition frequency. In strontium, the $^1S_0 \rightarrow ^1P_1$ transition strongly dominates the polarizability

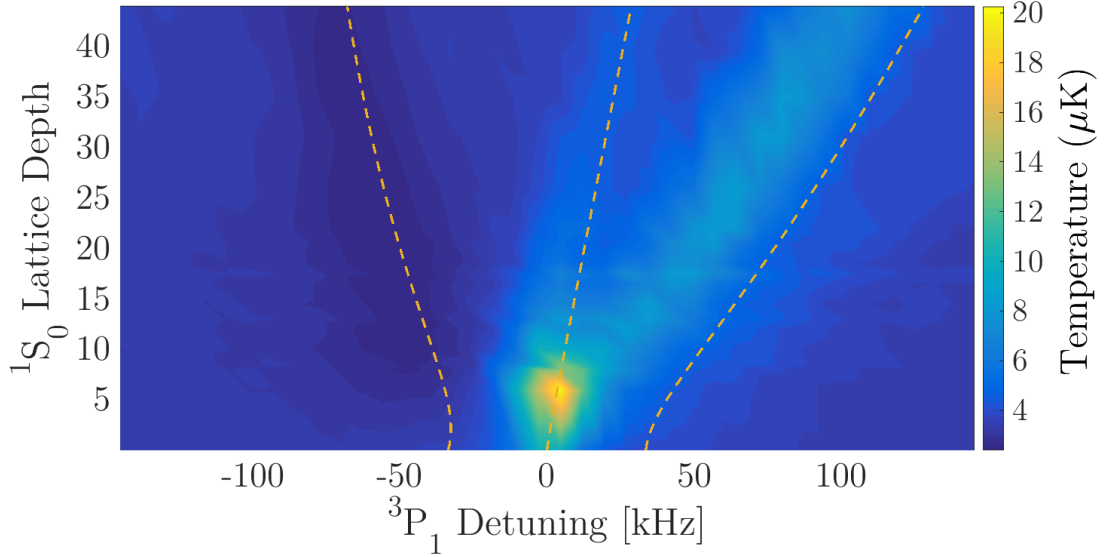


Figure 6.5 : Observation of driven sideband transitions

Driven sidebands in a 1D lattice as a function of lattice depth using an ultracold gas with an initial temperature of ≈ 200 nK. Dashed lines are the expected band positions using a 1D model of the lattice as shown in Fig. 6.1.1.

of the ground state and therefore can be used to estimate the effective off-resonant scattering rate. For this transition $\Gamma = 2\pi \times 30.5$ MHz and a 532 nm lattice is detuned by $\delta_{lat} \approx 2\pi \times 87$ THz. With a lattice depth of $V_{lat} = 10 E_r$ we expect a scattering rate of $\Gamma_{eff} \approx 2 \times 10^{-1} \text{ s}^{-1}$, which is negligible for the timescales of our proposed experiments. From Fig. 6.1.3, we see that there is not an appreciable loss of atoms over a one second timescale, supporting our estimate that off-resonant scattering is unimportant on these timescales.

6.2 Spin manipulation of ^{87}Sr

Here is where I need to introduce and characterize the LCR

Averaging images together (how to use this code specifcally)

6.3 Search for narrowline PA molecules using various spin mixtures

”Lorem ipsum dolor sit amet, consectetur adipiscing elit, sed do eiusmod tempor incididunt ut labore et dolore magna aliqua. Ut enim ad minim veniam, quis nostrud exercitation ullamco laboris nisi ut aliquip ex ea commodo consequat. Duis aute irure dolor in reprehenderit in voluptate velit esse cillum dolore eu fugiat nulla pariatur. Excepteur sint occaecat cupidatat non proident, sunt in culpa qui officia deserunt mollit anim id est laborum.”

Chapter 7

Conclusion

We have measured the binding energy of the least-bound vibrational level of the ground electronic state of the $^{86}\text{Sr}_2$ molecule with two-photon photoassociative spectroscopy. Using the universal prediction for the binding energy of a halo state including corrections derived for a van der Waals potential [Eq. (4.15)] [42, 43, 44], we extract an improved value of the s -wave scattering length.

We also characterized the AC Stark shift of the halo-state binding energy due to light near resonant with the single-photon photoassociation transition. A model only accounting for a single excited-state channel [?] cannot explain the observed frequency dependence of the AC Stark shift, which can be attributed to the proximity of other excited states.

Large AC Stark shifts of the halo state point to the possibility of optically tuning the ^{86}Sr scattering length, similar to recent demonstrations of optical tuning of magnetic Feshbach resonances [56, 38]. This is attractive because ground-state strontium lacks magnetic Feshbach resonances. With improved measurement of the photoassociation resonance frequency and its dependence on background atom density, perhaps combined with optical manipulation of the scattering length, it may also be possible to study the landscape of Efimov trimers associated with this naturally occurring scattering resonance. This work also points to the need for improved the-

ory, such as an improved calculation of the Sr ground-state molecular potential and C_6 coefficient, which could be compared with this high-accuracy measurement of the halo binding energy.

The work presented in this proposal is a natural extension of previous work done in our lab using an optical Feshbach resonance and one color photoassociation to manipulate the quantum state of a Bose-Einstein condensate. The creation and characterization of a novel type of Feshbach molecule is of fundamental interest to complete the analogy between optical and magnetic Feshbach resonances as well as to test the mechanism of Feshbach molecule stability in the presence of closed channel decay. This experiment provides a practical first demonstration of an optical lattice on our apparatus, which can be readily extended to a number of experiments such as out of equilibrium unitarity quenches [68], strongly interacting Bose gases stabilized by the quantum zeno effect [? 69, 70, 71], and the observation of exotic spin phases [8? , 9]. Moreover, additional insight might also be drawn from revisiting OFR and photoassociation in an optical lattice and employing new measurement techniques in the lattice [72]. These and future experiments will take advantage of the variety of interactions and narrow intercombination transitions available in strontium as well as the control and selectivity afforded through an optical lattice.

Bibliography

- [1] C. C. Bradley, C. A. Sackett, J. J. Tollett, and R. G. Hulet, “Evidence of Bose-Einstein condensation in an atomic gas with attractive interactions,” *Physical Review Letters*, vol. 75, pp. 1687–1690, aug 1995.
- [2] C. Méndez-Visag, “Responsible management of dental amalgam mercury: A review of its impact on health,” *Revista Peruana de Medicina Experimental y Salud Publica*, vol. 31, pp. 725–732, sep 2014.
- [3] F. Lang, K. Winkler, C. Strauss, R. Grimm, and J. H. Denschlag, “Ultracold triplet molecules in the rovibrational ground state,” *Physical Review Letters*, vol. 101, p. 133005, sep 2008.
- [4] C. Chin, R. Grimm, P. Julienne, and E. Tiesinga, “Feshbach resonances in ultracold gases,” *Reviews of Modern Physics*, vol. 82, pp. 1225–1286, apr 2010.
- [5] T. Köhler, K. Góral, and P. S. Julienne, “Production of cold molecules via magnetically tunable Feshbach resonances,” *Reviews of Modern Physics*, vol. 78, pp. 1311–1361, dec 2006.
- [6] J. A. Aman, J. C. Hill, R. Ding, K. R. A. Hazzard, T. C. Killian, and W. Y. Kon, “Photoassociative spectroscopy of a halo molecule in ^{86}Sr ,” *Physical Review A*, vol. 98, p. 053441, nov 2018.
- [7] K. M. Jones, E. Tiesinga, P. D. Lett, and P. S. Julienne, “Ultracold photoasso-

- ciation spectroscopy: Long-range molecules and atomic scattering,” *Reviews of Modern Physics*, vol. 78, pp. 483–535, may 2006.
- [8] M. E. Beverland, G. Alagic, M. J. Martin, A. P. Koller, A. M. Rey, and A. V. Gorshkov, “Realizing exactly solvable $SU(N)$ magnets with thermal atoms,” *Physical Review A*, vol. 93, p. 051601, may 2016.
- [9] G. Chen, K. R. Hazzard, A. M. Rey, and M. Hermele, “Synthetic-gauge-field stabilization of the chiral-spin-liquid phase,” *Physical Review A*, vol. 93, jan 2016.
- [10] S. Stenholm, *Laser cooling and trapping*, vol. 9 of *Graduate Texts in Contemporary Physics*. New York, NY: Springer New York, 1988.
- [11] T. Ido, Y. Isoya, and H. Katori, “Optical-dipole trapping of Sr atoms at a high phase-space density,” *Physical Review A - Atomic, Molecular, and Optical Physics*, vol. 61, p. 4, may 2000.
- [12] S. B. Nagel, C. E. Simien, S. Laha, P. Gupta, V. S. Ashoka, and T. C. Killian, “Magnetic trapping of metastable atomic strontium,” *Physical Review A - Atomic, Molecular, and Optical Physics*, vol. 67, p. 4, jan 2003.
- [13] T. Mukaiyama, H. Katori, T. Ido, Y. Li, and M. Kuwata-Gonokami, “Recoil-Limited Laser Cooling of Sr Atoms near the Fermi Temperature,” *Physical Review Letters*, vol. 90, p. 4, mar 2003.
- [14] T. H. Loftus, T. Ido, M. M. Boyd, A. D. Ludlow, and J. Ye, “Narrow line cooling and momentum-space crystals,” *Physical Review A - Atomic, Molecular, and Optical Physics*, vol. 70, p. 063413, dec 2004.

- [15] V. Begun and M. Gorenstein, “Bose-Einstein condensation of pions,” *Proceedings of Science*, vol. 82, p. 041602, oct 2007.
- [16] P. G. Mickelson, Y. N. Martinez De Escobar, M. Yan, B. J. Desalvo, and T. C. Killian, “Bose-Einstein condensation of Sr88 through sympathetic cooling with Sr87,” *Physical Review A - Atomic, Molecular, and Optical Physics*, vol. 81, pp. 5–8, may 2010.
- [17] M. K. Tey, S. Stellmer, R. Grimm, and F. Schreck, “Double-degenerate Bose-Fermi mixture of strontium,” *Physical Review A - Atomic, Molecular, and Optical Physics*, vol. 82, p. 011608, jul 2010.
- [18] M. Borkowski, R. Ciuryło, P. S. Julienne, S. Tojo, K. Enomoto, and Y. Taka-hashi, “Line shapes of optical Feshbach resonances near the intercombination transition of bosonic ytterbium,” *Physical Review A - Atomic, Molecular, and Optical Physics*, vol. 80, no. 1, pp. 1–14, 2009.
- [19] R. Ciurylo, E. Tiesinga, P. S. Julienne, R. Ciuryło, E. Tiesinga, P. S. Julienne, R. Ciurylo, E. Tiesinga, and P. S. Julienne, “Optical tuning of the scattering length of cold alkaline-earth-metal atoms,” *Physical Review A - Atomic, Molecular, and Optical Physics*, vol. 71, p. 030701, mar 2005.
- [20] J. L. Bohn and P. S. Julienne, “Prospects for influencing scattering lengths with far-off-resonant light,” *Physical Review A - Atomic, Molecular, and Optical Physics*, vol. 56, pp. 1486–1491, aug 1997.
- [21] T. L. Nicholson, S. Blatt, B. J. Bloom, J. R. Williams, J. W. Thomsen, J. Ye, and P. S. Julienne, “Optical Feshbach resonances: Field-dressed theory and com-

- parison with experiments,” *Physical Review A - Atomic, Molecular, and Optical Physics*, vol. 92, p. 022709, aug 2015.
- [22] M. Yan, B. J. DeSalvo, B. Ramachandhran, H. Pu, and T. C. Killian, “Controlling condensate collapse and expansion with an optical feshbach resonance,” *Physical Review Letters*, vol. 110, p. 123201, mar 2013.
- [23] S. Blatt, T. L. Nicholson, B. J. Bloom, J. R. Williams, J. W. Thomsen, P. S. Julienne, and J. Ye, “Measurement of Optical Feshbach Resonances in an Ideal Gas,” *Physical Review Letters*, vol. 107, p. 073202, aug 2011.
- [24] G. Thalhammer, M. Theis, K. Winkler, R. Grimm, and J. H. Denschlag, “Inducing an optical Feshbach resonance via stimulated Raman coupling,” *Physical Review A - Atomic, Molecular, and Optical Physics*, vol. 71, p. 033403, mar 2005.
- [25] M. Theis, G. Thalhammer, K. Winkler, M. Hellwig, G. Ruff, R. Grimm, and J. H. Denschlag, “Tuning the Scattering Length with an Optically Induced Feshbach Resonance,” *Physical Review Letters*, vol. 93, p. 123001, sep 2004.
- [26] F. K. Fatemi, K. M. Jones, and P. D. Lett, “Observation of optically induced Feshbach resonances in collisions of cold atoms,” *Physical Review Letters*, vol. 85, pp. 4462–4465, nov 2000.
- [27] R. Ciuryło, E. Tiesinga, S. Kotochigova, and P. S. Julienne, “Photoassociation spectroscopy of cold alkaline-earth-metal atoms near the intercombination line,” *Physical Review A - Atomic, Molecular, and Optical Physics*, vol. 70, p. 062710, dec 2004.
- [28] L. B. Ratcliff, J. L. Fish, and D. D. Konowalow, “Electronic transition dipole

- moment functions for transitions among the twenty-six lowest-lying states of $\{L\}i_2$,” *J. Mol. Spectrosc.*, vol. 122, p. 293, 1987.
- [29] A. S. Jensen, K. Riisager, D. V. Fedorov, and E. Garrido, “Structure and reactions of quantum halos,” *Reviews of Modern Physics*, vol. 76, no. 1, p. 215, 2004.
- [30] T. Köhler, K. Góral, and P. S. Julienne, “Production of cold molecules via magnetically tunable $\{F\}$ eshbach resonances,” *Reviews of Modern Physics*, vol. 78, no. 4, p. 1311, 2006.
- [31] E. Braaten and H. W. Hammer, “Universality in few-body systems with large scattering length,” *Physics Reports*, vol. 428, p. 259, 2006.
- [32] E. Braaten and H.-W. Hammer, “Efimov physics in cold atoms,” *Annals of Physics*, vol. 322, p. 120, jan 2007.
- [33] P. Naidon and S. Endo, “Efimov physics: A review,” *Reports on Progress in Physics*, vol. 80, p. 56001, 2017.
- [34] F. Luo, G. C. Mcbane, G. Kim, C. F. Giese, and W. R. Gentry, “The weakest bond: Experimental observation of helium dimer Effects of adiabatic, relativistic, and quantum electrodynamics interactions on the pair potential and thermophysical properties of helium The weakest bond: Experimental observation of helium dime,” *The Journal of Chemical Physics The Journal of Chemical Physics The Journal of Chemical Physics*, vol. 981, no. 10, 1993.
- [35] W. Scholikopf and J. P. Toennies, “Nondestructive Mass Selection of Small van der Waals Clusters,” *Science*, vol. 266, no. 5189, p. 1345, 1994.

- [36] E. Pachomow, V. P. Dahlke, E. Tiemann, F. Riehle, and U. Sterr, “Ground-state properties of Ca₂ from narrow-line two-color photoassociation,” *Physical Review A*, vol. 95, p. 043422, apr 2017.
- [37] C. Chin and P. S. Julienne, “Radio-frequency transitions on weakly bound ultracold molecules,” *Physical Review A - Atomic, Molecular, and Optical Physics*, vol. 71, no. 1, p. 12713, 2005.
- [38] L. W. Clark, L. C. Ha, C. Y. Xu, and C. Chin, “Quantum Dynamics with Spatiotemporal Control of Interactions in a Stable Bose-Einstein Condensate,” *Physical Review Letters*, vol. 115, p. 155301, 2015.
- [39] N. R. Claussen, S. J. J. M. F. Kokkelmans, S. T. Thompson, E. A. Donley, E. Hodby, and C. E. Wieman, “Very-high-precision bound-state spectroscopy near a 85 Rb Feshbach resonance,” *Physical Review A*, vol. 67, p. 60701, jun 2003.
- [40] M. Greiner, C. A. Regal, and D. S. Jin, “Emergence of a molecular {B}ose-{E}instein condensate from a {F}ermi gas,” *Nature*, vol. 426, p. 537, 2003.
- [41] S. Jochim, M. Bartenstein, A. Altmeyer, G. Hendl, S. Riedl, C. Chin, J. Hecker-Denschlag, and R. Grimm, “Bose-{E}instein condensation of molecules,” *Science*, vol. 302, p. 2101, 2003.
- [42] G. F. Gribakin and V. V. Flambaum, “Calculation of the scattering length in atomic collisions using the semiclassical approximation.pdf,” *Physical Review A*, vol. 48, p. 546, jul 1993.
- [43] B. Gao, “Angular-momentum-insensitive quantum-defect theory for diatomic

- systems,” *Physical Review A - Atomic, Molecular, and Optical Physics*, vol. 64, p. 10701, 2001.
- [44] B. Gao, “Binding energy and scattering length for diatomic systems,” *Journal of Physics B: Atomic, Molecular and Optical Physics*, vol. 37, p. 4273, nov 2004.
- [45] A. Stein, H. Knöckel, and E. Tiemann, “The $^1S+^1S$ asymptote of $\{S\}r^2$ studied by Fourier-transform spectroscopy,” *Eur. Phys. J. D*, vol. 57, p. 171, 2010.
- [46] R. Ciurylo, E. Tiesinga, and P. S. Julienne, “Stationary phase approximation for the strength of optical $\{F\}$ eshbach resonances,” *Physical Review A*, vol. 74, p. 22710, 2006.
- [47] M. Borkowski, A. A. Buchachenko, R. Ciuryło, P. S. Julienne, H. Yamada, Y. Kikuchi, K. Takahashi, Y. Takasu, and Y. Takahashi, “Beyond-Born-Oppenheimer effects in sub-kHz-precision photoassociation spectroscopy of ytterbium atoms,” *Physical Review A*, vol. 96, p. 63405, 2017.
- [48] R. Wynar, R. S. Freeland, D. J. Han, C. Ryu, and D. J. Heinzen, “Molecules in a $\{B\}$ ose- $\{E\}$ instein Condensate,” *Science*, vol. 287, p. 1016, 2000.
- [49] J. Wang, J. P. D’Incao, B. D. Esry, and C. H. Greene, “Origin of the Three-Body Parameter Universality in Efimov Physics,” *Phys. Rev. Lett.*, vol. 108, p. 263001, 2012.
- [50] X. Zhang, M. Bishof, S. L. Bromley, C. V. Kraus, M. S. Safronova, P. Zoller, A. M. Rey, and J. Ye, “Spectroscopic observation of $SU(N)$ - symmetric interactions in Sr orbital magnetism,” *Science*, vol. 345, p. 1467, aug 2014.

- [51] P. M. A. Mestrom, J. Wang, C. H. Greene, and J. P. D’Incao, “Efimov-van der Waals universality for ultracold atoms with positive scattering lengths,” *Physical Review A*, vol. 95, p. 32707, 2017.
- [52] T. Köhler, T. Gasenzer, and K. Burnett, “Microscopic theory of atom-molecule oscillations in a Bose-Einstein condensate,” *Physical Review A*, vol. 67, p. 13601, jan 2003.
- [53] C. A. Regal, C. Ticknor, J. L. Bohn, and D. S. Jin, “Creation of ultracold molecules from a Fermi gas of atoms,” *Nature*, vol. 424, p. 47, 2003.
- [54] H. Moritz, T. Stoferle, K. Gunter, M. Kohl, and T. Esslinger, “Confinement Induced Molecules in a 1D Fermi Gas,” *Physical Review Letters*, vol. 94, p. 210401, 2005.
- [55] M. Bartenstein, A. Altmeyer, S. Riedl, R. Geursen, S. Jochim, C. Chin, J. H. Denschlag, R. Grimm, A. Simoni, E. Tiesinga, C. J. Williams, and P. S. Julienne, “Precise determination of ^6Li cold collision parameters by radio-frequency spectroscopy on weakly bound molecules,” *Physical Review Letters*, vol. 94, no. 10, p. 103201, 2005.
- [56] D. M. Bauer, M. Lettner, C. Vo, G. Rempe, and S. Durr, “Control of a magnetic {F}eshbach resonance with laser light,” *Nature Physics*, vol. 5, p. 339, 2009.
- [57] R. Yamazaki, S. Taie, S. Sugawa, and Y. Takahashi, “Submicron spatial modulation of an interatomic interaction in a bose-einstein condensate,” *Physical Review Letters*, vol. 105, p. 050405, jul 2010.
- [58] M. Greiner, O. Mandel, T. Rom, A. Altmeyer, A. Widera, T. W. Hänsch, and

- I. Bloch, “Quantum phase transition from a superfluid to a Mott insulator in an ultracold gas of atoms,” *Physica B: Condensed Matter*, vol. 329-333, pp. 11–12, jan 2003.
- [59] Y. J. Lin, K. Jiménez-García, and I. B. Spielman, “Spin-orbit-coupled Bose-Einstein condensates,” *Nature*, vol. 471, pp. 83–86, mar 2011.
- [60] G. Thalhammer, K. Winkler, F. Lang, S. Schmid, R. Grimm, and J. H. Denschlag, “Long-lived feshbach molecules in a three-dimensional optical lattice,” *Physical Review Letters*, vol. 96, p. 050402, feb 2006.
- [61] T. Anker, *Ultracold quantum gases in one-dimensional optical lattice potentials*. PhD thesis, Ludwig-Maximilians-Universität München, 2005.
- [62] D. J. Bergman and D. Stroud, *Solid state Physics*. Saunders College, 1992.
- [63] D. Jaksch and P. Zoller, “The cold atom Hubbard toolbox,” *Annals of Physics*, vol. 315, pp. 52–79, jan 2005.
- [64] A. M. Rey, *Ultracold Bosonic Atoms in Optical Lattices*. PhD thesis, University of Maryland, 2004.
- [65] M. P. Fisher, P. B. Weichman, G. Grinstein, and D. S. Fisher, “Boson localization and the superfluid-insulator transition,” *Physical Review B*, vol. 40, pp. 546–570, jul 1989.
- [66] J. H. Denschlag, J. Hecker Denschlag, J. E. Simsarian, H. Häffner, C. McKenzie, A. Browaeys, D. Cho, K. Helmerson, S. L. Rolston, and W. D. Phillips, “A

- Bose-Einstein condensate in an optical lattice,” *Journal of Physics B: Atomic, Molecular and Optical Physics*, vol. 35, pp. 3095–3110, jul 2002.
- [67] J. J. Sakurai, *Modern Quantum Mechanics, Supplement I*. Pearson, 1994.
- [68] P. Makotyn, C. E. Klauss, D. L. Goldberger, E. A. Cornell, and D. S. Jin, “Universal dynamics of a degenerate unitary Bose gas,” *Nature Physics*, vol. 10, pp. 116–119, jan 2014.
- [69] B. Zhu, B. Gadway, M. Foss-Feig, J. Schachenmayer, M. L. Wall, K. R. Hazzard, B. Yan, S. A. Moses, J. P. Covey, D. S. Jin, J. Ye, M. Holland, and A. M. Rey, “Suppressing the loss of ultracold molecules via the continuous quantum Zeno effect,” *Physical Review Letters*, vol. 112, p. 070404, feb 2014.
- [70] L. S. Wong, B. W. N. Voon, S. C. Teo, and A. Balakrishnan, “Spectrometry analysis on Cyanobacteria for heavy metals detection in aquatic environment,” *Ecology, Environment and Conservation*, vol. 22, pp. 1107–1111, jan 2016.
- [71] N. Syassen, D. M. Bauer, M. Lettner, T. Volz, D. Dietze, J. J. García-Ripoll, J. I. Cirac, G. Rempe, and S. Dürr, “Strong dissipation inhibits losses and induces correlations in cold molecular gases,” *Science*, vol. 320, pp. 1329–1331, jun 2008.
- [72] S. Taie, S. Watanabe, T. Ichinose, and Y. Takahashi, “Feshbach-Resonance-Enhanced Coherent Atom-Molecule Conversion with Ultranarrow Photoassociation Resonance,” *Physical Review Letters*, vol. 116, p. 043202, jan 2016.

Appendices

Appendix A

Two-particle momentum probability distribution

A.1 Standard form

Typical derivation of relative momentum probability distribution function

We begin by considering the single particle momentum probability distribution function (gotten how)? Single particle momentum probability distribution

$$f^1(\mathbf{p}) = \left(\frac{1}{2\pi k_B T} \right)^{3/2} e^{\left(\frac{-p^2}{2mk_B T} \right)} \quad (\text{A.1})$$

Extension of this simple Boltzmann equation into the two-particle regime is complicated due to dependence of each particle on the others. If however, we make the assumption that particle collisions are rapid (on some timescale) we can approximate the two particle momentum distribution as the product of two single particle functions. This is known as the molecular chaos assumption and is important for what???

The two particle distribution for a homogeneous system is then

$$\begin{aligned} f^2(\mathbf{p}_1, \mathbf{p}_2) &= f^1(\mathbf{p}_1) f^1(\mathbf{p}_2) \\ &= \left(\frac{1}{2\pi m k_B T} \right)^3 \exp \left(\frac{-(p_1^2 + p_2^2)}{2m k_B T} \right) \end{aligned} \quad (\text{A.2})$$

Next, we'd like to consider a center-of-mass frame for the distribution. So we'll define

we define the relative and center-of-mass momenta of the two particles by defining

$$\begin{aligned}\mathbf{P}_c &= \mathbf{p}_1 + \mathbf{p}_2 & M &= m_1 + m_2 = 2m \\ \mathbf{p}_r &= \frac{\mathbf{p}_1 - \mathbf{p}_2}{2} & \mu &= \frac{m_1 m_2}{m_1 + m_2} = \frac{m}{2}\end{aligned}$$

from these equations we can use conservation of energy to determine the quadrature sum of the two momenta

$$\begin{aligned}\frac{p_1^2}{2m} + \frac{p_2^2}{2m} &= \frac{P_c^2}{2M} + \frac{p_r^2}{2\mu} \\ p_1^2 + p_2^2 &= \frac{P_c^2}{2} + 2p_r^2\end{aligned}$$

thus the momentum probability distribution take the form

$$f^2(\mathbf{P}_c, \mathbf{p}_r) = \left(\frac{1}{2\pi M k_B T} \right)^{3/2} \left(\frac{1}{2\pi \mu k_B T} \right)^{3/2} \exp \left(\frac{-P_c^2}{2M k_B T} \right) \exp \left(\frac{-p_r^2}{2\mu k_B T} \right) \quad (\text{A.3})$$

A.2 Truncated form

Here I will derive, motivate, and test limiting cases. Plots showing the effects of truncation will be in the main text

Two particle distribution (for correcting notation, use C and R when denoting

CoM and Rel)

$$f_{\mathbf{r},trunc}^2(\mathbf{p}_1, \mathbf{p}_2) = A^2 \left(\frac{1}{2\pi m k_B T} \right)^3 \exp \left(\frac{-(p_1^2 + p_2^2)}{2m k_B T} \right) \times \Theta \left(\epsilon_{max} - U(\mathbf{r}) - \frac{p_1^2}{2m} \right) \Theta \left(\epsilon_{max} - U(\mathbf{r}) - \frac{p_2^2}{2m} \right) \quad (\text{A.4})$$

We have introduced a normalization constant A here to ensure the that integration over the truncated probability distribution remains equal to one.

The meaning of r is such that f should be evaluated at each point in space. Furthermore since the atoms are held in a trapping potential. each point in space has a local trap depth relative to the lip at the top of the trap **need some figure to try and denote this**

Want distribution of relative momenta so integrate out center of mass. Going to drop the two and trunc for now

$$\begin{aligned} \tilde{f}_{\mathbf{r}}(\mathbf{p}_{rel}) &= \int d^3\mathbf{P}_c f_{\mathbf{r}}(\mathbf{p}_1, \mathbf{p}_2) \\ &= \left(\frac{1}{2\pi M k_B T} \right)^{3/2} \left(\frac{1}{2\pi \mu k_B T} \right)^{3/2} A^2 \int d^3\mathbf{P}_c e^{\left(\frac{-P_c^2}{2M k_B T} \right)} e^{\left(\frac{-p_r^2}{2\mu k_B T} \right)} \\ &\quad \times \Theta \left(\epsilon_{max} - U(\mathbf{r}) - \frac{P_c^2}{8m} - \frac{p^2}{2m} - \frac{\mathbf{P}_c \cdot \mathbf{p}}{2m} \right) \Theta \left(\epsilon_{max} - U(\mathbf{r}) - \frac{P_c^2}{8m} - \frac{p^2}{2m} + \frac{\mathbf{P}_c \cdot \mathbf{p}}{2m} \right) \end{aligned} \quad (\text{A.5})$$

Spherically symetrix collisions so can integrate by transforming into spherical coordinates with the radius aligned along the interatomic axis

$$\begin{aligned} \tilde{f}_{\mathbf{r}}(\mathbf{p}) &= \left(\frac{1}{2\pi M k_B T} \right)^{3/2} \left(\frac{1}{2\pi \mu k_B T} \right)^{3/2} e^{\left(\frac{-p_r^2}{2\mu k_B T} \right)} A^2 \int_0^\pi \sin \theta d\theta \int_0^{2\pi} d\phi \int_0^\infty dP_c P_c^2 e^{\left(\frac{-P_c^2}{2M k_B T} \right)} \\ &\quad \times \Theta \left(\epsilon_{max} - U(\mathbf{r}) - \frac{P_c^2}{8m} - \frac{p^2}{2m} - \frac{P_c p \cos \theta}{2m} \right) \Theta \left(\epsilon_{max} - U(\mathbf{r}) - \frac{P_c^2}{8m} - \frac{p^2}{2m} + \frac{P_c p \cos \theta}{2m} \right) \end{aligned} \quad (\text{A.6})$$

$$X = \cos \theta$$

$$dX = -\sin \theta d\theta$$

Substitute and integrate over ϕ

$$\begin{aligned} \tilde{f}_{\mathbf{r}}(\mathbf{p}) &= \left(\frac{1}{2\pi M k_B T} \right)^{3/2} \left(\frac{1}{2\pi \mu k_B T} \right)^{3/2} e^{\left(\frac{-p_r^2}{2\mu k_B T} \right)} 2\pi A^2 \int_{-1}^1 dX \int_0^\infty dP_c P_c^2 e^{\left(\frac{-P_c^2}{2M k_B T} \right)} \\ &\times \Theta \left(\epsilon_{max} - U(\mathbf{r}) - \frac{P_c^2}{8m} - \frac{p^2}{2m} - \frac{P_c p X}{2m} \right) \Theta \left(\epsilon_{max} - U(\mathbf{r}) - \frac{P_c^2}{8m} - \frac{p^2}{2m} + \frac{P_c p X}{2m} \right) \end{aligned} \quad (\text{A.7})$$

Recognize that the Heaviside functions cancel each other out on either side of zero, so can eliminate one of the Heavisides and multiply by 2

$$\begin{aligned} \tilde{f}_{\mathbf{r}}(\mathbf{p}) &= \left(\frac{1}{2\pi M k_B T} \right)^{3/2} \left(\frac{1}{2\pi \mu k_B T} \right)^{3/2} e^{\left(\frac{-p_r^2}{2\mu k_B T} \right)} 4\pi A^2 \int_0^1 dX \int_0^\infty dP_c P_c^2 e^{\left(\frac{-P_c^2}{2M k_B T} \right)} \\ &\times \Theta \left(\epsilon_{max} - U(\mathbf{r}) - \frac{P_c^2}{8m} - \frac{p^2}{2m} - \frac{P_c p X}{2m} \right) \end{aligned} \quad (\text{A.8})$$

From here we can rewrite using the infinite relative momentum probability distribution $f_{\mathbf{r},\infty}(\mathbf{p})$ from [some equation](#)

$$\begin{aligned} \tilde{f}_{\mathbf{r}}(\mathbf{p}) &= \left(\frac{1}{2\pi \mu k_B T} \right)^{3/2} e^{\left(\frac{-p_r^2}{2\mu k_B T} \right)} \mathcal{G}(T, \epsilon_{max}, p_{rel}) \\ &= f_{\mathbf{r},\infty}(\mathbf{p}) \mathcal{G}(T, \epsilon_{max}, p_{rel}) \end{aligned} \quad (\text{A.9})$$

where $\mathcal{G}(T, \epsilon_{max}, p_{rel})$ is given by

$$\begin{aligned} \mathcal{G}(T, \epsilon_{max}, p_{rel}) = A^2 \left(\frac{4\pi}{2\pi M k_B T} \right)^{3/2} \int_0^1 dX \int_0^\infty dP_c P_c^2 e^{\left(\frac{-P_c^2}{2M k_B T} \right)} \\ \times \Theta \left(\epsilon_{max} - U(\mathbf{r}) - \frac{P_c^2}{8m} - \frac{p^2}{2m} - \frac{P_c p X}{2m} \right) \end{aligned} \quad (\text{A.10})$$

Now define two dimensionless variables $\tilde{\epsilon}$ and \tilde{E} which will be used to change variables once more

$$\begin{aligned} \tilde{\epsilon} &= \frac{p_{rel}^2}{2\mu k_B T} & \tilde{E} &= \frac{P_c^2}{2M k_B T} \\ p &= \sqrt{2\mu k_B T \tilde{\epsilon}} & P_c &= \sqrt{2M k_B T \tilde{E}} \\ dpp^2 &= \frac{\sqrt{\tilde{\epsilon}}}{2} (2\mu k_B T)^{3/2} d\tilde{\epsilon} & dP_c P_c^2 &= \frac{\sqrt{\tilde{E}}}{2} (2M k_B T)^{3/2} d\tilde{E} \end{aligned}$$

Plugging these expressions into Eq.A.10 and rearranging

$$\begin{aligned} \tilde{f}_{\mathbf{r}}(\mathbf{p}) = A^2 \frac{e^{-\tilde{\epsilon}}}{(2\pi\mu k_B T)^{3/2}} \int_0^1 dX \frac{2}{\sqrt{\pi}} \int_0^\infty d\tilde{E} e^{-\tilde{E}} \sqrt{\tilde{E}} \\ \times \Theta \left(\eta(\mathbf{r}) - \frac{\tilde{E}}{2} - \frac{\tilde{\epsilon}}{2} - X \sqrt{\tilde{E} \tilde{\epsilon}} \right) \end{aligned} \quad (\text{A.11})$$

would like to turn this distribution into a relative energy distribution. Collisions are isotropic so we can use the relation

$$\begin{aligned} \int dpp^2 \int d\Omega_p \tilde{f}_{\mathbf{r}}(\mathbf{p}) &= \int d\tilde{\epsilon} \hat{f}_{\mathbf{r}}(\tilde{\epsilon}) = 1 \\ \Rightarrow 4\pi p^2 \tilde{f}_{\mathbf{r}}(\mathbf{p}) dp &= \hat{f}_{\mathbf{r}}(\tilde{\epsilon}) d\tilde{\epsilon} \end{aligned} \quad (\text{A.12})$$

using dpp^2 given above we then write

$$\hat{f}_{\mathbf{r}}(\tilde{\epsilon}) = A^2 \sqrt{\tilde{\epsilon}} e^{-\tilde{\epsilon}} \frac{2}{\sqrt{\pi}} \int_0^1 dX \frac{2}{\sqrt{\pi}} \int_0^\infty d\tilde{E} e^{-\tilde{E}} \sqrt{\tilde{E}} \Theta \left(\eta(\mathbf{r}) - \frac{\tilde{E}}{2} - \frac{\tilde{\epsilon}}{2} - X \sqrt{\tilde{E}\tilde{\epsilon}} \right) \quad (\text{A.13})$$

We can now choose the normalization constant A^2 using

$$\int_0^{2\eta(\mathbf{r})} d\tilde{\epsilon} \hat{f}_{\mathbf{r}}(\tilde{\epsilon}) = 1$$

where we have used an energy cutoff of $2\eta(\mathbf{r})$ since either particle may have an energy in the range $[0 \rightarrow \eta(\mathbf{r})]$. With the normalization, the complete expression for $\hat{f}_{\mathbf{r}}(\tilde{\epsilon})$ is then

$$\hat{f}_{\mathbf{r}}(\tilde{\epsilon}) = \frac{2}{\sqrt{\pi}} \sqrt{\tilde{\epsilon}} e^{-\tilde{\epsilon}} \hat{\mathcal{G}}(\eta_{\mathbf{r}}, \tilde{\epsilon}) \quad (\text{A.14})$$

where all the effects of the truncation have been moved to $\hat{\mathcal{G}}$, given by

$$\hat{\mathcal{G}}(\eta_{\mathbf{r}}, \tilde{\epsilon}) = \frac{\int_0^1 dX \frac{2}{\sqrt{\pi}} \int_0^\infty d\tilde{E} e^{-\tilde{E}} \sqrt{\tilde{E}} \Theta \left(\eta(\mathbf{r}) - \frac{\tilde{E}}{2} - \frac{\tilde{\epsilon}}{2} - X \sqrt{\tilde{E}\tilde{\epsilon}} \right)}{\int_0^{2\eta(\mathbf{r})} d\tilde{\epsilon} \frac{2}{\sqrt{\pi}} \sqrt{\tilde{\epsilon}} e^{-\tilde{\epsilon}} \int_0^1 dX \frac{2}{\sqrt{\pi}} \int_0^\infty d\tilde{E} e^{-\tilde{E}} \sqrt{\tilde{E}} \Theta \left(\eta(\mathbf{r}) - \frac{\tilde{E}}{2} - \frac{\tilde{\epsilon}}{2} - X \sqrt{\tilde{E}\tilde{\epsilon}} \right)}$$

we can check the limiting behavior of this equation since we expect when

$$\lim_{\eta \rightarrow \infty} \hat{\mathcal{G}}(\eta_{\mathbf{r}}, \tilde{\epsilon}) = 1$$

. Indeed, remembering that

$$\int_0^\infty dx \sqrt{x} e^{-x} = \frac{\sqrt{\pi}}{2}$$

then this requirement is fulfilled.

Appendix B

Imagefit analysis routine

”Lorem ipsum dolor sit amet, consectetur adipiscing elit, sed do eiusmod tempor incididunt ut labore et dolore magna aliqua. Ut enim ad minim veniam, quis nostrud exercitation ullamco laboris nisi ut aliquip ex ea commodo consequat. Duis aute irure dolor in reprehenderit in voluptate velit esse cillum dolore eu fugiat nulla pariatur. Excepteur sint occaecat cupidatat non proident, sunt in culpa qui officia deserunt mollit anim id est laborum.”

General procedure, should probably suggest moving to Github and warn about software migration breaking older versions of code.

Currently everything is working in 2015b? Can it work in a newer version?

B.1 Background removal

Covers *imagefit_Background_PCA*

Would like to remove noisy fringes to fit more easily

B.1.1 Principal component analysis

be sure to discuss tradeoffs such as matrix size, basis size, and number of images

The Anderson and Cornell groups have adapted two statistical techniques used

in astronomical data processing to the analysis of images of ultracold atom gases. Image analysis is necessary for obtaining quantitative information about the behavior of an ultracold gas under different experimental conditions. Until now, the preferred method has been to find a shape (such as a Gaussian) that looks like the results and write an image-fitting routine to probe a series of photographs. The drawback is that information extracted this way will be biased by the model chosen.

The two groups recently employed model-free analysis techniques to extract results from interferometry experiments on Bose-Einstein condensates (BECs). The statistical processing techniques were able to rapidly pinpoint correlations in large image sets, helping the researchers uncover unbiased experimental results. Using the techniques, graduate student Steve Segal, former graduate student Quentin Diot, Fellows Eric Cornell and Dana Anderson, and a colleague from Worcester Polytechnic Institute calibrated their interferometer, identified and mitigated some noise sources, and unearthed signal information partially buried in the noise generated during the BEC experiment. By looking for correlations and relationships between pixels in a series of images (a), the researchers were able to clearly "see" changes in the overall number of atoms (d), changes in the vertical positions of three peaks in a momentum distribution (c), and changes in the fraction of atoms in the central peak (b), which was the primary experimental signal.

The results were obtained with principal component analysis (PCA) and independent component analysis (ICA). PCA identified simple pixel correlations and looked for areas of maximum variance. Such areas provided an idea about where to look for changes in size, structure, or position of the ultracold atom cloud. The

PCA analysis was sufficient for calibrating the interferometer and debugging the experiment. It also provided an idea of size changes in one or more features of the experiment. However, the PCA analysis alone wasn't perfect. ICA was required to extract the most important information about the experiment, i.e., the fraction of the total number of atoms in one of three clouds. Using preprocessed data from a PCA analysis, ICA was able to test whether the values of neighboring pixels were statistically independent from one another. With this information, ICA could then determine relative differences in the experimental signal and separate its individual features.

Segal thinks physicists in the ultracold atomic physics field will be intrigued by the potential of using the PCA and ICA techniques to probe their experimental images. There are only two caveats: The techniques require 10–100 images, and their application to ultracold atom-cloud experiments is still in its infancy. - Julie Phillips

B.1.2 Comparison of PCA implementations

B.2 Fitting the spatial distribution

Covers *imagefit_NumDistFit*

B.3 Evaluating fit parameters

Covers *imagefit_ParamEval*

B.3.1 Writing new plug-ins

B.3.2 Suggested improvement

Move all data structures (or at least the experimental plugin ones) to be table based so that everything is held at the same level. This would make it much easier to be flexible with different analyses (since you're not imposing a structure that might be restrictive later)

One of the key lessons I've learned is to be flexible when starting new projects. You don't know where the data is going to take you or what may come up as an interesting/useful perspective for developing and questioning hypotheses. Tables are a scheme that I've have realized are very common in data management and analysis. The popular python package Pandas, uses datatables exclusively and was the impetus for my interest in the data structure. Tables also make it easy to export and share your data via spreadsheet applications (assuming you use simple datatypes within each cell) Lastly, this is a warning that no matter what you end up doing with the data, you will inevitably have to spend time organizing and reorganizing it at times. With less structure imposed on the data you'll be able to manipulate things more easily and (most importantly to Tom) more quickly.

Appendix C

neuKLEIN - Killian lab experimental interface

During my time working on the neutral apparatus, Joe Whalen began a rewrite of the Labview based experimental control software which had grown organically through the first decade of the neutral apparatus' existence. Following this refactor, the user interface was also revamped to help reduce human errors and improve overall data collection efficiency. This chapter will outline the major components of the neuKLEIN software package and how this system integrates with the hardware control system and the software analysis algorithm.

C.1 Labview code

Need to have description of state machine.

Need to

Use of references for updating front panel

Need to get references for LV documentation for this stuff

Discuss triggered waveform oddity (retriggerable setup)

C.2 FPGA code

The versatility of FPGA led us to want to simple system for setting static voltages and switching them at will. We built such a system using an National Instrument FPGA device (Xilinx something). The hardware details and circuitry are available in [appendix blah](#). This section will focus on the software side of programming and using the FPGA system.

This was originally a project started by a summer student named Weixuan Li in summer 2018. He did a good job.

Talk about special programs (the custom operation builder specifically)

C.3 Possible future improvements

Specifically thinking about the ability to do network shared variables. Then we could dedicate a mahcine to an instrument and share the data using a networking layer instead of a hard connection.

Movement to full state machine

Standardization of the triggered waveform VI

implementation of coupled scanning mechanism (how is this currently handled)

Appendix D

Experimental control computer hardware

”Lorem ipsum dolor sit amet, consectetur adipiscing elit, sed do eiusmod tempor incididunt ut labore et dolore magna aliqua. Ut enim ad minim veniam, quis nostrud exercitation ullamco laboris nisi ut aliquip ex ea commodo consequat. Duis aute irure dolor in reprehenderit in voluptate velit esse cillum dolore eu fugiat nulla pariatur. Excepteur sint occaecat cupidatat non proident, sunt in culpa qui officia deserunt mollit anim id est laborum.”

D.1 Overview of status

D.2 Migration to a new machine

D.3 PixelFly camera system

What is the datasheet? Where are the drivers? What OS is it compatible with?

Double shot system, the difference in camera exposure times, how we mitigate that difference and what errors might result because of this timing.

Get the double shot timing diagram.

Appendix E

Concise derivation of effective volumes

The following derivation is meant to serve as a quick reference for finding the analytic form of the effective volumes for ultracold gases held in a optical dipole trap. This section follows the arguments presented by Mi's paper which considers and numerically evaluates the general case of power-law potentials and the corresponding density distribution at arbitrary temperatures less than the trap depth.

If instead one restricts to the experimentally reasonable conditions of high- η (recall η is the ratio of trap depth to sample temperature, $\eta = \epsilon_t/k_B T$) and harmonic trapping potentials, then a useful analytic expression can be found for the effective volumes of the gas.

Following eff volume derivation from first year

Appendix F

Repair of 922 Lynx master

”Lorem ipsum dolor sit amet, consectetur adipiscing elit, sed do eiusmod tempor incididunt ut labore et dolore magna aliqua. Ut enim ad minim veniam, quis nostrud exercitation ullamco laboris nisi ut aliquip ex ea commodo consequat. Duis aute irure dolor in reprehenderit in voluptate velit esse cillum dolore eu fugiat nulla pariatur. Excepteur sint occaecat cupidatat non proident, sunt in culpa qui officia deserunt mollit anim id est laborum.”

Appendix G

Custom circuitry

”Lorem ipsum dolor sit amet, consectetur adipiscing elit, sed do eiusmod tempor incididunt ut labore et dolore magna aliqua. Ut enim ad minim veniam, quis nostrud exercitation ullamco laboris nisi ut aliquip ex ea commodo consequat. Duis aute irure dolor in reprehenderit in voluptate velit esse cillum dolore eu fugiat nulla pariatur. Excepteur sint occaecat cupidatat non proident, sunt in culpa qui officia deserunt mollit anim id est laborum.”

G.1 AC line zero crossing trigger

G.2 Hard drive shutters

G.3 Power locks

G.4 Photodiodes

G.5 Infinite sample and hold

G.5.1 Reduced intensity fluctuations for sub-hertz exposures

Don’t forget to talk about whatever noise I observed. I think there is a picture on my phone of this.

Appendix H

Miscellaneous tips and tricks

”Lorem ipsum dolor sit amet, consectetur adipiscing elit, sed do eiusmod tempor incididunt ut labore et dolore magna aliqua. Ut enim ad minim veniam, quis nostrud exercitation ullamco laboris nisi ut aliquip ex ea commodo consequat. Duis aute irure dolor in reprehenderit in voluptate velit esse cillum dolore eu fugiat nulla pariatur. Excepteur sint occaecat cupidatat non proident, sunt in culpa qui officia deserunt mollit anim id est laborum.”

H.1 Alignment of GHz AOM

H.2 Using the Picoscope in Labview(TM)

H.3 Liquid crystal retarder

H.4 Newport(TM) optomotion control

H.5 Fast analog lock for 689 nm

H.6 Porta CoM technique

H.7 Measuring Rabi frequencies